Transverse flow in 2-8 AGeV Au+Au at the BNL AGS

By
William Patrick Caskey
B.S. (University of California, Davis) 1994
M.S. (University of California, Davis) 1996

DISSERTATION
Submitted in partial satisfaction of the requirements for the degree of
DOCTOR OF PHILOSOPHY
in
Physics
in the
OFFICE OF GRADUATE STUDIES
of the
UNIVERSITY OF CALIFORNIA
DAVIS

Approved:

Committee in Charge
1999

William Patrick Caskey
June 1999
Physics

Transverse flow in 2-8 AGeV/c Au+Au at the BNL AGS

Abstract

Transverse flow of particles in nucleus-nucleus collisions has been studied in the region of incident beam energies of nominally $2 - 8\ A - GeV$. We see that in ^{197}Au on ^{197}Au collisions, that there is large proton transverse flow ($.240\ c$). The two pion species have been observed to exhibit smaller anti-flow for the same energy range.

Dedicated to my loving wife Karen
for her love and support through these
many joyous and difficult years.

Acknowledgements

First and foremost I would like to thank my advisor, Daniel Cebra, for taking a risk on me and helping through these many years. I would also like to thank my parents (both Caskey and Balvert) for their love and support. Also my son Will who provided endless hours of entertainment playing in the drafts of this dissertation.

I would like to also acknowledge and thank, Jim Draper, Paul Brady, Juan Romero, Lynn Wood and each of the members of the E895 collaboration for helping me in this great undertaking. Special thanks to Jenn Klay for working so hard on the particle identification.

This research made possible by a grant from the National Science Foundation.

Contents

List of Figures

List of Tables

Chapter 1

Introduction

1.1 Introduction

The purpose of this dissertation is to examine the role played by pions in relativistic heavy ion collisions. I will be studying the pion flow signals in the light of nucleon flow for comparison. Nucleon flow has been used as an experimental means of determining the equation of state (EOS) of nuclear matter. This has been an important physics goal which spreads across the fields of nuclear physics and astrophysics. A better understanding of the EOS is needed to explain supernovae, neutron stars, and also high energy heavy ion collisions. The compressibility of nuclear matter provides some insight into the equation of state. Heavy ion beams make it possible to study nuclear compression in the laboratory.

In the mid 1970's, studies of heavy ion reactions by theorists Scheid, Müller and Greiner [Sche74] using ideal hydrodynamics led to the observation that the transverse expansion of the fluid was important. This sideward flow was then tested by several experiments, originally the Streamer Chamber [Stro83] and Plastic Ball [Bade15]. These experimental studies led to publications [Gust84] and [Renf84] in which the first experimental observations of flow were reported.

To probe the hottest, earliest, most dense stage of a reaction, one would like to study an observable which becomes established during this early phase and remains constant as the system evolves. Several models [Sche74,Stoc80,Bert84, Krus85,Aich86] suggest that nucleon "flow" has this property. Flow of nucleons has been interpreted as a recoil effect from the compression generated in the early stage of a heavy ion collision. Sideward flow is defined as the preferential emission of particles in the reaction plane such that particles with velocities higher (lower) than the center of mass velocity are preferentially emitted on the same side of the beam axis as the projectile (target)[Sche74,Gust84]. The reaction plane is defined by the beam vector and the impact parameter of the event.

Figure 1.1 shows some of the measured nucleon flow which has been systematically studied across a broad range of energies from $\sim 25A-MeV$ up to $160A-GeV$ [Part97, Herm96,Barr96,Barr97,Mage99]. The flow can be observed to be rising monotonically with bombarding energy up to $1\,A-GeV$ where the observed flow reaches a value of 220 MeV/c. The magnitude increases with the increased compression which is generated by the higher beam energies. A saturation in the observed flow was first seen by the EOS group [Chan97] in the Ni+Cu system. By applying a scaling developed by Chance and Brady, it has been suggested that this maximum should be the same for all systems. The observed maximum in Ni+Ni has since been confirmed by the FOPI group [Herm96]. More recently, the E877 experiment has provided a data point at $10.8\,A-GeV$ for which the extracted flow is observed to be only $150\,MeV/c$ [Barr96,Barr97]. This is lower than the maximum flow which had been observed previously at roughly $1\,A-GeV$ in the EOS data. This reduction in nucleon flow indicates a 'softening' of the equation of state, which corresponds to a change in the degrees of freedom allowed to the system. This change in degrees of freedom is explained by the opening of the pion production channel at energies above the

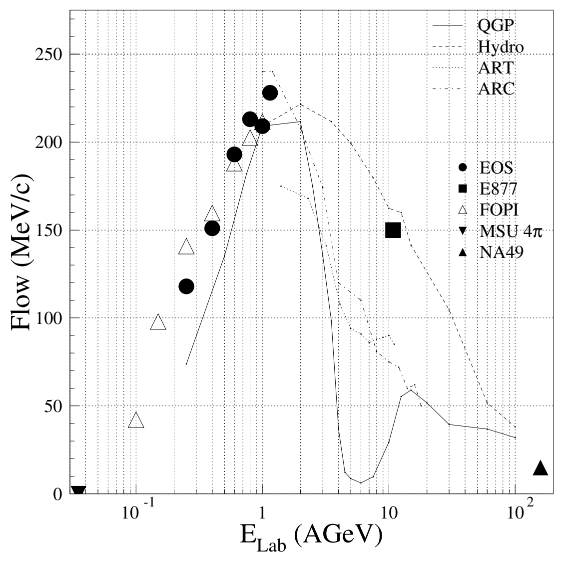

Figure 1.1: Extracted flow (as defined by the slope of $\langle p_x \rangle$ as a function of normalized rapidity) as a function of beam energy for Au+Au experiments. The theory predictions are plotted as curves while the experimental results are indicated by the plotting symbols. References are provided in the text.

delta resonance. Figures 1.2, 1.3, 1.4 and 1.5 demonstrate this. The reduction in the observed nucleon flow is predicted by several models, specifically, ART [LiKo96], ARC [Kaha96], Hydro and a variant of Hydro that includes a quark gluon plasma transition [Risc96]. However, more data are needed to differentiate between these models and their interpretations. Analyses of the data from 2 to 8 $A - GeV$ will fill in this crucial energy range.

1.2 Pions

Pions are unique to the discussion because they are not present before the reaction. They are created in the reaction and therefore may carry different information about the reaction dynamics. They are used to explain the softening of the EOS at the $1-2A-GeV$ area as seen by the nucleon flow and therefore must in themselves be studied to support these assumptions and the conclusions made from them. Measurements of the pion flow exist for 1.0 [Cebr98,Pink96] and $1.15A-GeV$ by [Kint97] bounding the lower energy range of this experiment. Pions have also been measured at $10.8A-GeV$ by E877 which bounds our upper energy range. Therefore the E895 experiment with energy samplings at 2,4,6 and 8 $A-GeV$ will fill in the energy excitation function where the pion channel is softening the EOS. For large impact parameters the pions are seen to be anti-flowing. This means that the $\langle p_x \rangle$ is directed away from the flowing protons in the reaction. The pion signal was originally believed to be due exclusively to their parent Δ resonances and these by their proton production. This would have led to a positive flow signal. The apparent anti-flow signal is now thought to be due to the competition between the Δ process and rescattering or absorption effects. As can be seen in Fig. 1.6 from [Barn98], there is a very large cross section for the pions to interact with the nuclear matter. This then depletes the number of pions being emitted in the flow plane (where the nucleons are preferentially emitted), leading to an anti-flow signal for the pions. Theoretical attempts at explaining the competition by BUU [Bass93] and QMD [Bass96] by turning on and off the scattering process

($\pi + N \rightarrow \Delta \rightarrow \pi + N$) versus the absorption process ($N + \Delta \rightarrow N + N$) have been performed. These attempts found that the signal was mostly due to the rescattering or shadowing effect. In light of these large interaction cross sections, it is necessary for the models to address the pions properly if conclusions about the nucleons are to be made.

1.3 Pion Interactions

It should be noted that all of the inferences made about the flow signals are model dependent. The models all depend on the input parameters and the basic interactions of the pions. Pion production cross sections have been accumulated and summerized by VerWest and Arndt [VerW82]. Figures 1.2, 1.3, 1.4 and 1.5. show the relevant plots. The cross sections for the neutron interactions can be obtained through Clebsch-Gordan coefficients assuming charge independence of the nuclear forces. Noting that the pion carries an isospin of $I = 1$ with $I_3 = 1,\ 0,\ -1$ for the π^+, π° and the π^- respectively, while the nucleons are $I = 1/2$ with $I_3 = 1/2,\ -1/2$ for the proton and neutron respectively. With these we can consult the tables and find that the reaction cross sections for the neutrons can be related in strength to that of the protons.

$$\sigma(nn \rightarrow np\pi^-) \quad = \quad \sigma(pp \rightarrow pn\pi^+) \qquad (1.1)$$

$$\sigma(np \rightarrow pp\pi^-) \quad = \quad \sigma(np \rightarrow nn\pi^+) \tag{1.2}$$

Pion interaction cross sections can be found in [Barn98] and are shown in Fig. 1.6. These show only proton and deuteron interactions. Neutron interactions are inferred from Clebsch-Gordon coefficients. Note that in general the pion + nucleon isospin state can couple to two isospin values (3/2 and 1/2). As is described by Griffiths in [Grif87] the 1/2 state can generally be ignored due to the very large $\Delta(1232)$ resonance which is in the 3/2 state. This large resonance can easily be seen in Fig. 1.6 at the energy of $\sim 1232\ MeV$. The fallowing equations show the Clebsch-Gordon deconvolution of the pion+nucleon elastic interactions,

$$\sigma(\pi^+p \rightarrow \pi^+p) \quad = \quad M|3/2, 3/2> \tag{1.3}$$

$$\sigma(\pi^-p \rightarrow \pi^-p) \quad = \quad 1/3\, M|3/2, -1/2> +2/3\, M|1/2, -1/2> \tag{1.4}$$

$$\sigma(\pi^+n \rightarrow \pi^+n) \quad = \quad 1/3\, M|3/2, 1/2> +2/3\, M|1/2, 1/2> \tag{1.5}$$

$$\sigma(\pi^-n \rightarrow \pi^-n) \quad = \quad M|3/2, 3/2> \tag{1.6}$$

and for the four charge exchange reactions that we are interested in.

$$\sigma(\pi^+n \rightarrow \pi^\circ p) \quad = \quad \sqrt{2}/3\, M|3/2, 3/2> -\sqrt{2}/3\, M|1/2, 1/2> \tag{1.7}$$

$$\sigma(\pi^-p \rightarrow \pi^\circ n) \quad = \quad \sqrt{2}/3\, M|3/2, 3/2> -\sqrt{2}/3\, M|1/2, -1/2> \tag{1.8}$$

$$\sigma(\pi^\circ n \rightarrow \pi^-p) \quad = \quad \sqrt{2}/3\, M|3/2, 3/2> -\sqrt{2}/3\, M|1/2, -1/2> \tag{1.9}$$

$$\sigma(\pi^\circ p \rightarrow \pi^+n) \quad = \quad \sqrt{2}/3\, M|3/2, 3/2> -\sqrt{2}/3\, M|1/2, 1/2> \tag{1.10}$$

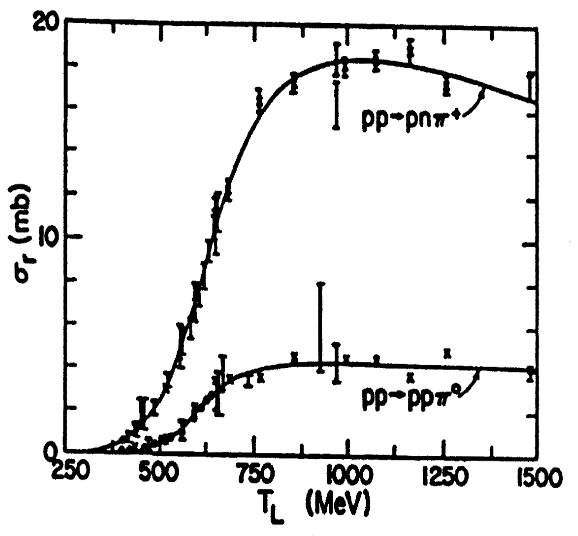

Figure 1.2: Reaction cross sections for $(pp \rightarrow pp\pi^o)$ and $(pp \rightarrow pn\pi^+)$. T_L is the kinetic energy of the beam in the laboratory.

Where M is the scattering matrix element. If we ignore the $M|1/2,*>$, as was stated above, then the total cross sections (summing the charge exchange with the elastic scattering) for the charged pions are in the following ratios.

$$\sigma(\pi^+n)_{tot} : \sigma(\pi^+p)_{tot} : \sigma(\pi^-n)_{tot} : \sigma(\pi^-p)_{tot}$$

$$3 : 9 : 9 : 3$$

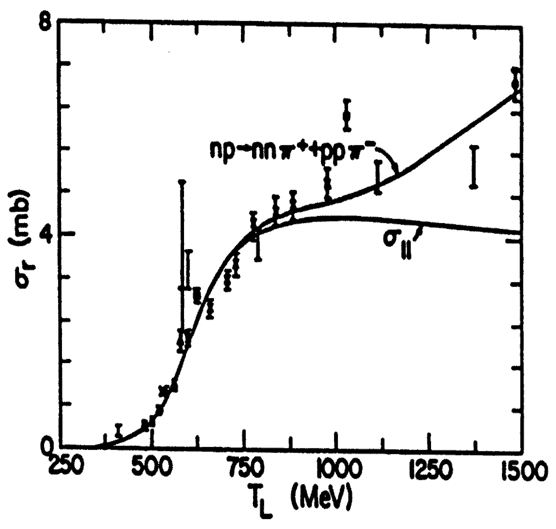

Figure 1.3: Reaction cross sections for $(pn \to pn\pi^+ + pp\pi^-)$. T_L is the kinetic energy of the beam in the laboratory.

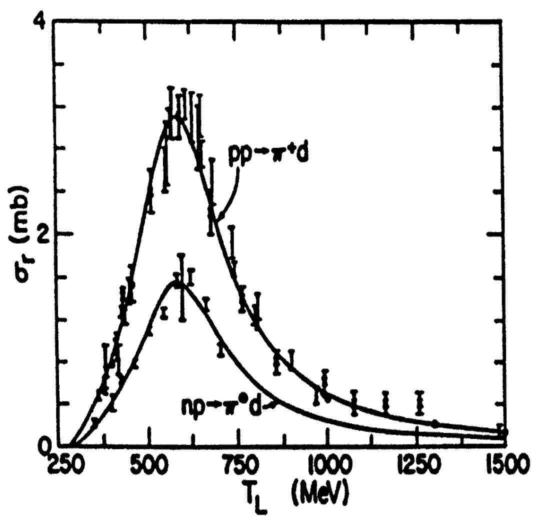

Figure 1.4: Reaction cross sections for $(pp \to \pi^+ d)$ and $(pn \to \pi^o d)$. T_L is the kinetic energy of the beam in the laboratory.

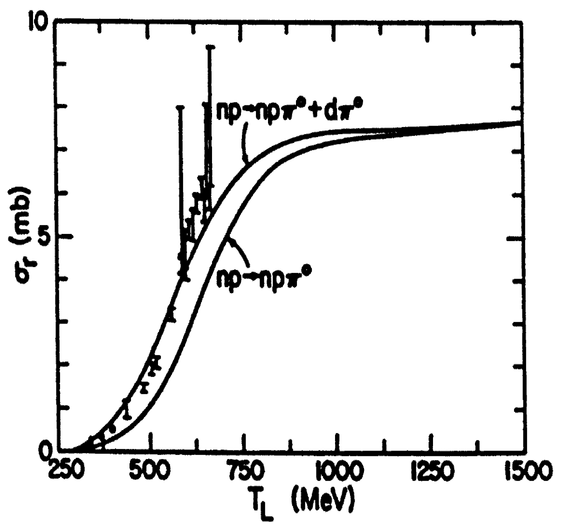

Figure 1.5: Reaction cross sections for $(pn \rightarrow pn\pi^o + d\pi^o)$ and $(pn \rightarrow np\pi^o)$. T_L is the kinetic energy of the beam in the laboratory.

It should be noted that these cross sections are those of free or nearly free nucleons and therefore are only the beginning. In order to study the in-medium effects new measurements and assumptions are necessary. This set of data will allow for the testing of these theories specifically with respect to their addressing the pion contributions to the reactions.

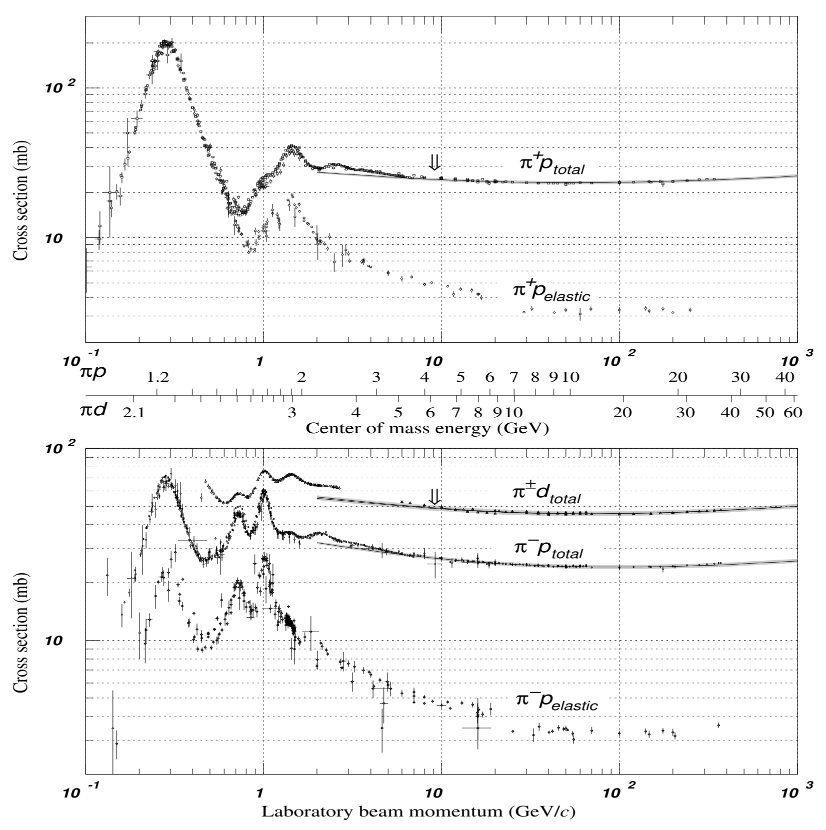

Figure 1.6: Reaction cross sections for π^+p_{total} and $\pi^+p_{elastic}$ in the upper panel, and π^-p_{total}, $\pi^-p_{elastic}$ and $\pi^{\pm}d_{total}$ in the lower panel.

Chapter 2

Instrumentation

2.1 Overview

The E895 experiment was a continuation of the EOS experiment which was performed at the BEVALAC of the Lawrence Berkley National Laboratory (LBNL). The EOS experiment was designed to be a nearly 4π detector system (in the center of mass frame) for the study of event-by-event physics. The main detector was the EOS TPC (Time Projection Chamber), which was also the primary detector for the E895 experiment. The TPC was used to detect the energy loss, charge, and momentum of the outgoing particles from the interactions: Au+Au, Au+Ag, Au+Cu and Au+Be. Table 2.1 displays the data samples taken. The experiment was performed at the Brookhaven National Laboratory in Upton, New York. It was conducted in the Multi-Particle Spectrometer (MPS) magnet area of the Alternating Gradient Synchrotron (AGS) on the A1 beam line. Built in 1960, the Alternating Gradient Synchrotron or AGS is a 250 m diameter synchrotron capable of accelerating protons to 33 GeV,Oxygen to 15 $A-GeV$ and Au up to 10.8 $A-GeV$. Data contained in this document consists of the ^{197}Au on ^{197}Au experiment, at energy samplings of nominally 2, 4, 6 and 8 $A-GeV$ kinetic energy with several centrality selections.

2.2 EOS TPC

The main detector in the E895 experiment was the EOS TPC which was relocated from Lawrence Berkley National Laboratory (Fig. 2.1). The TPC was designed to reconstruct the three dimensional trajectory and multiply sampled energy loss of each charged particle as it left the interaction region. The momentum and particle identification can be obtained, thus allowing the reconstruction of the event at freeze out.

Momentum reconstruction was obtained from the relation below based on the principle of charged particle curvature in a magnetic field.

$$\begin{aligned} mv &= qrB \qquad (2.1) \\ m &= mass \\ v &= velocity \\ q &= charge \\ B &= magnetic\,field \\ r &= radius\,of\,curvature \end{aligned}$$

The direction of curvature can be used to determine the sign of the particle's charge state, however it should be noted that an assumption must be made concerning the direction of the propagation for a given track. We assume first that the particle is traveling forward along the beam axis and find its direction of curvature and thereby determine its charge sign. This assumption is then checked by testing to see if the particle's helix can be projected back to the target. If this is not the case then we assume the particle looped around and traveled backward through the TPC and, therefore, has the opposite sign. This procedure can determine the sign of all target related tracks, non-target or secondary decay tracks must rely on the forward traveling direction assumption. The magnitude of the charge is still as yet unknown. This leads to an ambiguity in the momentum of the particle as the momentum determination

System	Energy	Target	Magnet Setting	Trigger	Events
Au+Au	2	2%	0.75 Tesla	Central	300k
		2%	0.75	Min Bias	60
Au+Au	4	3%	0.75	Semi	300
		3%	1.0	Semi	190
		3%	1.0	Central	300
		1%	1.0	Min Bias	40
Au+Au	6	3%	1.0	Central	700
		3%	1.0	Min Bias	100
Au+Au	8	3%	1.0	Central	364
		3%	1.0	Min Bias	59

Table 2.1: Total statistics of events from the E895 Experiment.

depends on the rigidity and charge of the particle as in Eq. (2.2). The energy loss of the particle as it passes through the gas combined with the information of rigidity

$$R = \frac{mv}{q} = rB \tag{2.2}$$

can be used to identify the particles and thereby, remove this ambiguity (see Section 3.4 for details on the particle identification).

The TPC consists of a large drift volume, a multi-wire proportional chamber (MWPC), and a pad plane with readout. The drift volume of the TPC measures $150\,cm \times 96\,cm \times 75\,cm$ and is filled with P10 counting gas ($10\%CH_4$ $90\%Ar$). This volume is then surrounded by a field cage which provides $120\,Volts/cm$ of drift field toward the MWPC plane. Below this region is the pad plane which reads out the signals. It consists of $128\,rows \times 120\,pads/row = 15360\,pads$ each of $1.2\,cm \times .8\,cm$ pitch (center to center pad spacing), where the $1.2\,cm$ pad length is in the nominal

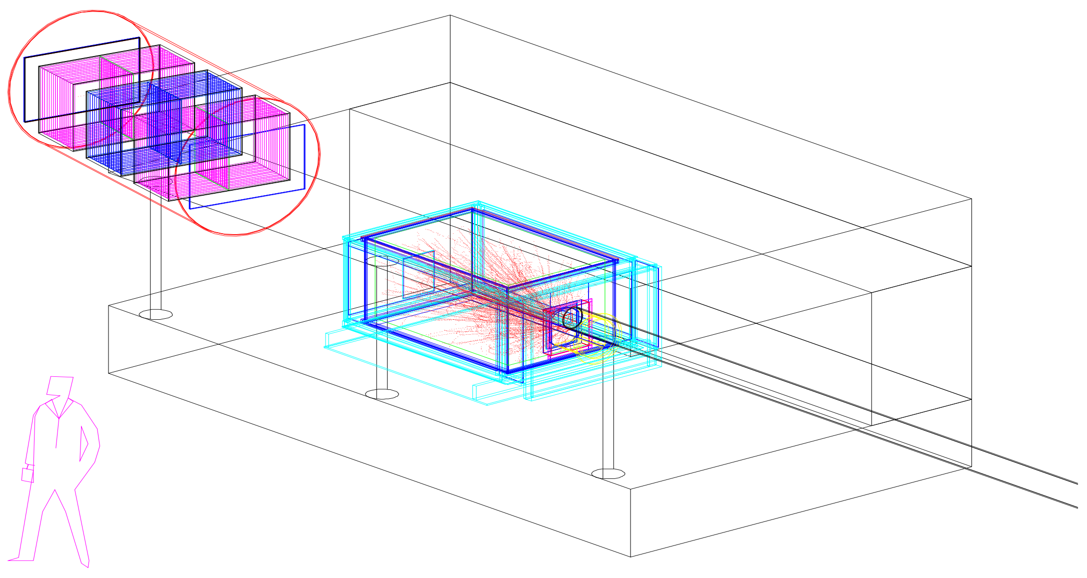

Figure 2.1: The E895 experimental setup. On the left is the cylinder representing the MUSIC chamber (not located to scale), then inside the MPS pole tip region is the EOS TPC shown with a typical 4 $A-GeV$ event. The beam enters from the right. Not shown are the beam profiling scintillators which sit $\sim 3m$ upstream of the magnet pole tip.

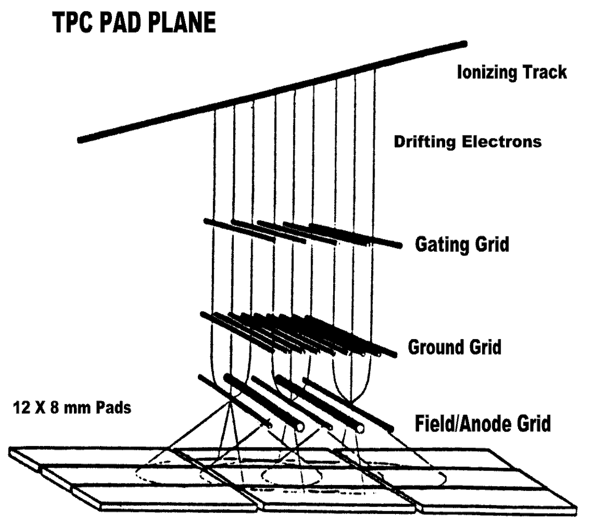

Figure 2.2: TPC READOUT REGION

beam direction or z-axis. The arrangement of the readout region is shown in Fig. 2.2.

When a charged particle passes through the P10 gas in the active drift volume it ionizes the gas through the standard dE/dx energy loss of Bethe Block [Fern92]. In P10 one typically gets 100 primary ion pairs per cm of trajectory at atmospheric pressure [Fern92]. These ion pairs then experience the $120\,V/cm$ drift field and begin to migrate or drift. The electric field is designed so that the electrons will drift down into the MWPC region at a terminal velocity of $\sim 5\,cm/\mu s$ [Fern92]. Parallel to the electric field is the MPS's $10\,kG$ magnetic field. The purpose of this field is two fold, first it causes the trajectories of the charged particles being tracked to curve allowing their momentum reconstruction by the relation in Eq. (2.1), and it causes

EOS TPC Characteristics	
Pad Plane Area	$1.536\,m \times .96\,m$
Number of Pads	15320 (120 × 128)
Pad Size	$12\,mm \times 8\,mm$
Drift Distance	$75\,cm$
Time Sampling Freq.	$10\,MHz$
Signal Shaping Time	$250\,ns$
Electronic Noise	$700\,e$
Gas Gain	3000
Gas Composition	$90\% Ar\ 10\% CH_4$
Pressure	$1\ Atm.$
B Field	$10\,kG$
E Field	$120\,V/cm$
Drift Velocity	$\sim 5\,cm/\mu s$

Table 2.2: Design Specifications for the EOS TPC.

Pad Signal for Centered Minimum Ionizing Particle	
dE/dx	$1250\,eV/cm$
Pad Length	$1.2\,cm$
Energy loss(eV)/Ion Pair	26
Gas Gain	3000
Efficiency of Charge collection due to the integration time	0.4
Wire-Pad Coupling	0.16
Pad Signal	$11000\,e$

Table 2.3: Signal Profile for the EOS TPC. Note that the 'Pad Signal' is the result of the MWPC configuration. The signal is from the gas ionization ($1250 eV/cm \cdot 1.2 cm/26 eV = 58\,ions$) which is then multiplied by the MWPC's gain ($58\,ions \cdot 3000 \cdot .4 = 70000\,ions$) at the anode wire. The pads are actually inductively coupled to the anode wire with a coupling of .16 yielding the final signal of 11000 electrons.

Electronics Specifications							
Device	Gain	Device Noise	Cumulative Noise		Min Ion Signal	Device Maximum (Saturation)	
			e	mV	mV	mV	$Min\ Ion's$
Preamp	$.32\ \mu V/e$	$600\ e$	600	.192	3.5	2000	570
Shaper	6.5	.5		1.3	23	2000	90

Table 2.4: Electronics Profile for the EOS TPC.

the electrons to spiral as they drift. This spiraling limits their transverse diffusion and therefore, increases the resolution in the pad plane dimensions ([Fern92] and [Lohs]) as depicted by the longitudinal D_L and transverse D_T diffusion parameters below. Where D_o is the natural thermal diffusion of the gas with no magnetic field effects in the equations below.

$$\begin{aligned} D_L(B) = D_o &= \frac{kTv_D}{eE} && (2.3) \\ D &= \frac{\sigma^2}{2t} \\ v_d &= \frac{l_d}{t} \\ \sigma^2_{D_o} &= \frac{2kT}{eE} l_d \\ measured & \\ \sigma_{D_L} &= 320\mu m/\sqrt{cm} && (2.4) \end{aligned}$$

Where l_d is the drift distance, E is the electric field,e the electric charge,t the drift time and v_d is the drift velocity in the equations above.

$$\begin{aligned} D_T(B) &= \frac{D_o}{1+\omega^2\tau^2} && (2.5) \\ \sigma^2_T &= \frac{2D_T}{v_d} l_d \\ \sigma^2_T &= \frac{D_o}{1+\omega^2\tau^2}\frac{l_d}{v_d} \end{aligned}$$

$$\begin{aligned} &\mathit{measured} \\ &(\mathit{with\ B\ field}) \\ \sigma_T &= 185\mu m/\sqrt{cm}\ \mathit{at}\ .5\ \mathit{Tesla} \end{aligned} \tag{2.6}$$

Where ω is the cyclotron frequency and τ is the mean time between collisions.

It should be noted that these diffusion relations are for a track crossing at zero angle above the pad row. The diffusion is modified by the equations below for non-zero track crossing angle. For a discussion of how it is corrected see Section 3.3. The Lorentz angle mentioned in the equation below is to account for the fact that the magnetic and electric field lines are far from parallel as the electrons drift into the anode wires [Lohs].

$$\begin{aligned} \sigma_w &= \frac{d}{\sqrt{12}} \cdot |\tan\alpha - \tan\Psi| \\ \alpha &= \mathit{angle\ to\ wire\ normal\ of\ the\ track} \\ \Psi &= \arctan\omega\tau = \mathit{Lorentz\ angle} \end{aligned} \tag{2.7}$$

Once the electrons enter the MWPC region, they are accelerated by the $1/r$ E-field of the anode wires ($20\,\mu m$ diameter at $1200\,Volts$) and undergo multiplication through avalanche ionization. The electrons are then carried away by the anodes. The large number of positive ions that are left behind induce an image charge on the pad plane below.

The Townsend relations [Fern92] allow us to calculate the gain for the MWPC's configuration

$$\begin{aligned} \alpha &= PAe^{-BP/\varepsilon} \\ P &= Pressure \end{aligned} \tag{2.8}$$

$$\begin{aligned}\varepsilon &= Electric\,field\\ A &= 12-14\frac{1}{cm\,torr}\\ B &= 180\frac{V}{cm\,torr}\\ M(x) &= e^{\int_x^0 \alpha(y)dy} \qquad (2.9)\end{aligned}$$

The constants A and B are determined for the gas used. The factor α^{-1} is the mean free path of ionization for the electron. The gain (M) is then the integration of α over the multiplication distance (‘y’ in the integration) which is essentially from the beginning of the MWPC region (the ‘x’ integration limit) to the anode wire (the zero in integration limit). The above values are for the P10 gas of the TPC. The resulting avalanche provides a gain of 3×10^3 in the number of ions which is sufficient for detection by the pad plane electronics and yields the typical signals listed in the various tables above. The TPC pad size was set such that most particles will create a ‘three pad hit’ for this gain and diffusion allowing what would be a 3-point gaussian if it were fit in only one dimension. Therefore the TPC would be capable of a typical spatial resolution of $.7\,mm$. If, however we have only one pad hits the resolution is reduced to

$$\sigma_{1pad} = \frac{8\,mm}{\sqrt{12}} = 2.3\,mm \qquad (2.10)$$

and the hit position is taken to be the center of the pad.

The image charge is then collected by a charge sensitive pre-amplifier (16:1 signal to noise ratio, dynamic range 4200:1) [Rai90] located in the electronics bay directly below the pad plane. The pre-amp integrates the total charge that is collected onto each pad. This is then channeled into a shaping amplifier that differentiates and then integrates the pre-amp signal. The dynamic ranges of the devices allow for 90 times minimum ionization signals [Rai90]. The amplitude of the signal has been kept carefully linear throughout the process, thus the final signal is proportional to number of primary ions in the gas. This information will be used to establish energy loss later in the analysis phase. The shaper amplifier signals are sampled at 100 ns intervals and stored as 'time buckets' in a Switch Capacitor Array [Rai90]. This sampling rate value was designed to match with the longitudinal diffusion of Eq. (2.3). The resolution here is due to the diffusion and shaper response but can be represented by the time resolution. A gaussian fit in the time dimension of the TPC yields a typical timing resolution of 20 ns which then ($\sim 5\ cm/\mu s$ at 20 ns) results in about 1 mm. The SCA accomplishes this storage via an array of independent capacitors that are sequentially filled by the amplifier output by a series of solid state switches. This provides digitization in the time direction for each pad of the analog signal. Coupling this with the 2-dimensional position of the pad, a 3-dimensional picture of the tracks can be reconstructed as in Fig. 2.3.

The positive ions from the avalanche having done their job inducing a signal on the pad plane now become a liability. They drift approximately 2000 times slower than the drifting electrons. They therefore provide a large sink for the primary electrons that may be drifting down from the next event by creating a large positive

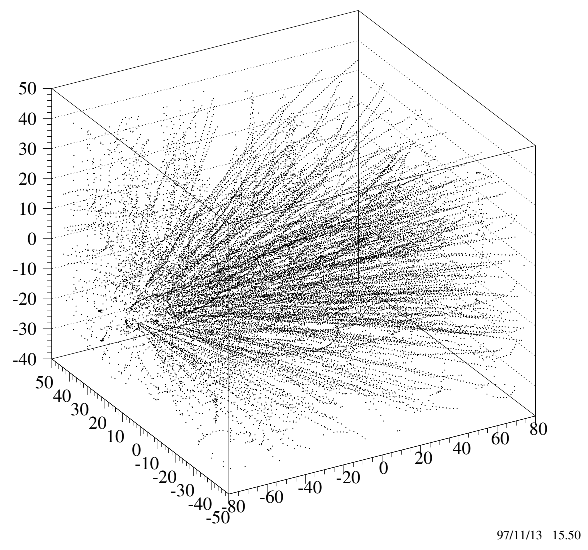

Figure 2.3: Each cross shows the position of a hit found in the TPC.

space charge drifting slowly back to the top of the TPC. The gating grid is used to eliminate this space charge by closing it after the primary electrons pass through. Fig. 2.4 shows the two states of the gating grid. The grid remains closed until the chamber is ready for the next event. The gating grid prevents the amplification of non-triggered events of beam tracks, which reduces the build up of positive space charge within the active volume of the TPC. It also provides a termination point for the positive ions which are collected and neutralized.

Momentum and Energy Loss resolution govern many of the device specifications of the TPC. First the momentum resolution can be estimated by the following equations. Equations were taken from the STAR Conceptual Design Report [STAR92] and the typical resolution for the EOS TPC is about 1%.

$$\begin{aligned}\frac{\delta P}{P} &= \frac{P\sigma\sqrt{720}}{eBs^2\sqrt{n+6}} \qquad (2.11)\\ P &= momentum\,(GeV/c)\\ \sigma &= Resolution\,(spatial)\,(m)\\ e &= .2998GeV\,Tesla\,m/c\\ B &= Magnetic\,Field\,(Tesla)\\ n &= number\,of\,samples\\ s &= Track\,length\,(m)\end{aligned}$$

Next the Energy Loss resolution of the detector is taken into account. Linearity of the TPC electronics was necessary for the Particle Identification scheme discussed in Section 3.4. The overall resolution can be predicted from Allison and Cobb's [Alli80] empirical formula which suggests in a resolution of 7-10% for the EOS TPC's configuration.

$$\begin{aligned}\frac{\delta I}{I} &= \frac{.96}{2.35}n^{-.46}(Ph)^{-.32}(\frac{dE}{dx})_{trunc} \qquad (2.12)\\ t &= Sampling\,Thickness\,(cm)\\ P &= Pressure\,(atm)\\ h &= Sample\,length\,(cm)\\ n &= Number\,of\,Samples\end{aligned}$$

2.3 The Trigger

The TPC's drifting electrons take up to 20 μs to reach the readout region. By the standards of nuclear electronics, this is a slow detector. Fast triggering detectors were needed to determine when an event of interest occurred, and then to initiate the

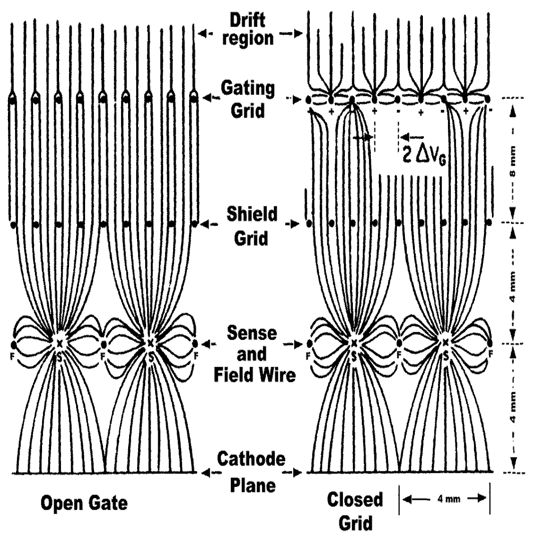

Figure 2.4: The two configurations of the Gating Grid. On the left is the open configuration which allows the drifting electrons to terminate on the anode multiplication wires. On the right is the closed position that terminate all drifting charges on the non-multiplying Gating Grid plane and thereby neutralizing the charges.

sequence of actions necessary to record that event. Primarily this consisted of opening the gating grid to allow the primary ionization to drift into the MWPC region of the TPC. The trigger detectors were also used to provide a precise measure of the start time of the TPC's drift sampling, or the T0 signal.

The trigger was designed to insure that first the TPC had a good beam candidate, i.e. a gold beam particle had arrived on target. The beam particle was identified by scintillators S1,V1 and V2 which were upstream of the target as seen in Fig. 2.7. Scintillators V1 and V2 had 1 cm holes cut such that they performed a veto function separating out off axis beam particles or upstream interactions. A logic signal of

$S1 \cdot \overline{V1} \cdot \overline{V2}$ identified a beam particle.

The next criterion for the trigger was that something ‘interesting’ had happened to the projectile or beam candidate. A target scintillator (ST) was placed just down stream of the the target ($\sim 1\ cm$). The principle is that a particle will deposit light as a function of Z^2 as described by Ahlen [Ahle77]. Figures 2.5 and 2.6 show the theory (Eq. (2.13)) and E895 data for comparison (noting that the scintillator will have a linear response to the energy deposited). The parameters of the the model are discussed in [Ahle80]. It should be noted that the Ahlen model and Fig. 2.5 are for the ideal case of only a single charged particle in the scintillator. In the actual events this is not the case, however one can see that Fig 2.6 agrees reasonably well with the model. One can see in these plots that the break-up of the projectile (which is indicated by the sum of the Z^2's as seen in the MUSIC chamber) corresponds to a reduced amplitude on the ST scintillator. One can see in the figure that by adjusting the discriminator thresholds on the ST scintillator we can directly affect the spectator matter seen in MUSIC.

$$\begin{aligned}
\frac{dL}{dx} &= A\{(1-F_s)e^{-B_s(1-F_s)\frac{dE}{dx}} + F_s\}\frac{dE}{dx} \qquad (2.13)\\
A &= scintillator\ constant\ (mV/MeV)\ (empirical)\\
B_s &= 4.5 \times 10^{-3} gm/cm^2/MeV\ (empirical)\\
F_s &= \frac{1}{2}\frac{\ln(\frac{\varepsilon_{max}}{T_o}) - \beta^2}{\ln(\frac{\varepsilon_{max}}{I_{adj}}) - \beta^2}\\
F_s &= number\ of\ \delta's\ escaping\ core\ ionization\\
\varepsilon_{max} &= 2m_ec^2\beta^2\gamma^2\\
I_{adj} &= 63eV\ \ adjusted\ ionization\ potential\\
&\quad\ for\ scintillator
\end{aligned}$$

$$T_0 \;=\; \sim 1.5keV\;(empirical) \tag{2.14}$$

We set an upper threshold on the ST signal such that, at a minimum, uninteracted beam particles were excluded. A lower limit was set to remove noise signals, but below the Z=1 particle limit. These two settings then formed a window for good 'interactions'. The upper limit could also be lowered to generate more central collision data sets. The logic signal of $\overline{ST}$ was defined to be an ADC level within the window. The basic interaction trigger was then $\overline{ST} \cdot S1 \cdot \overline{V1} \cdot \overline{V2}$. The basic trigger would then open the gating grid, begin buffering the read out data from the pad plane of the TPC and establish the T0 start time of the event.

The trigger was further complicated by three additional hardware constraints. The first two were due to the fact that the TPC needs $\sim 20\,\mu s$ of drift time after an event has occurred to allow for the drift of all of the electrons. Therefore, a post-pileup signal was developed which required no beam candidates after a trigger for $20\,\mu s$. A pre-pileup veto was also established to require that there had been no beam candidates less than $\sim 20\,\mu s$ prior to the event. The third constraint was the data-to-tape bottleneck imposed by the tape drive queues. Each event represents approximately 2 MegaBytes of data therefore, the DAQ could be easily saturated resulting in computer dead time. Pre-pileup and DAQ BUSY (computer dead time) then acted to negate potential triggers. Post pileup then acted to negate an established trigger, thereby reclosing the gating grid and dumping the buffered data. In addition to determining the trigger status, the raw signals from each of the scintillators were also digitized

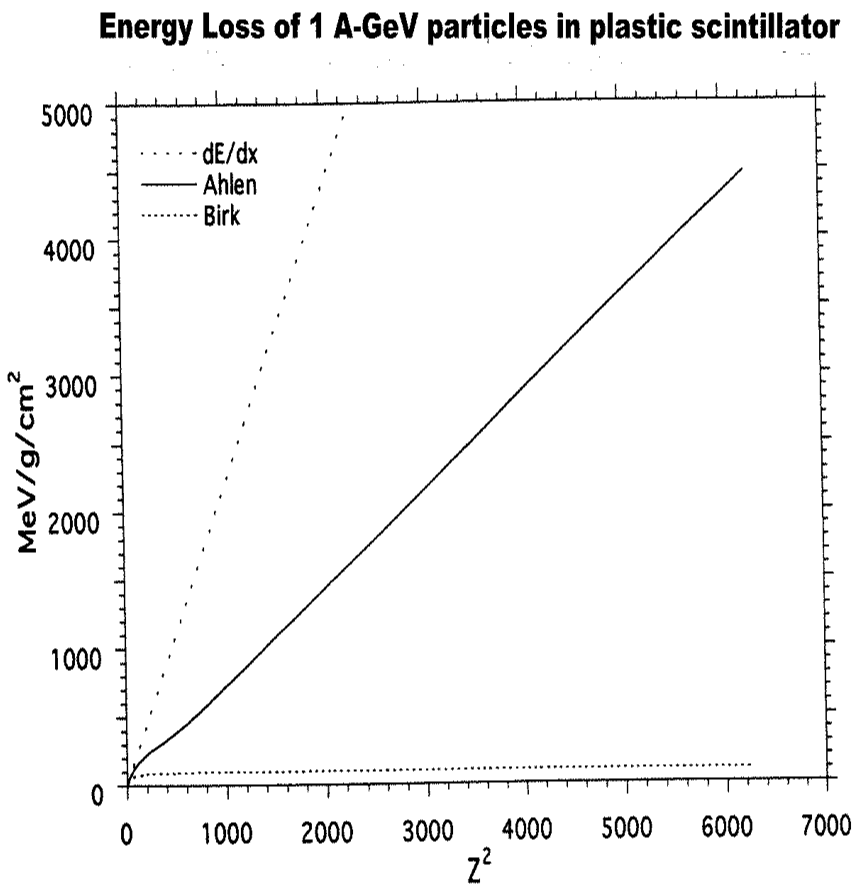

Figure 2.5: Energy converted to light in organic scintillator versus charge. Ahlen takes into account saturation effects due to the light production that limits the conversion of dE/dx to light. Also shown is theory from [Birk64] and dE/dx via Bethe-Block assuming perfect efficiency of conversion. Courtesy of Juan Romero.

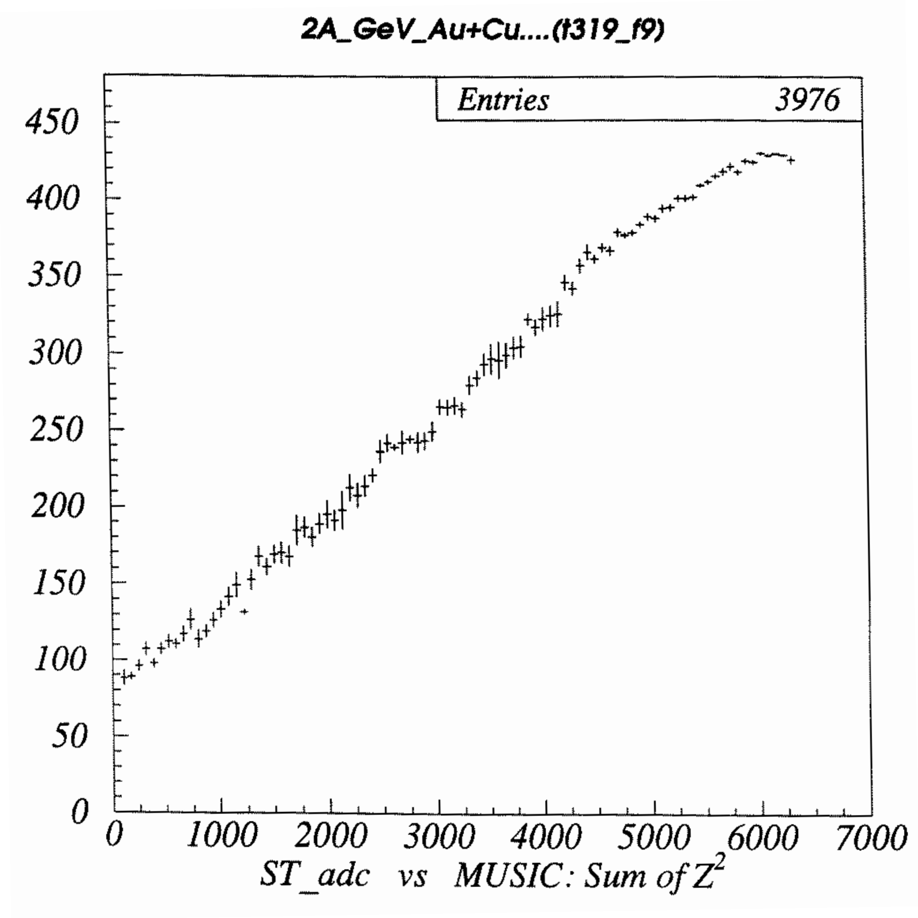

Figure 2.6: ST scintillator ADC spectrum versus the sum of the charged fragments seen in the MUSIC detector. Note that the uninteracted gold beam can be seen in the upper most right hand corner (accounting for the small statistical error bars there). Courtesy of Juan Romero.

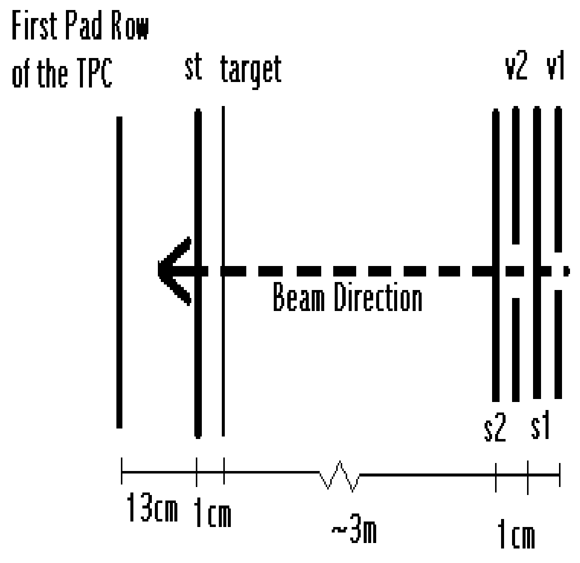

Figure 2.7: Triggering scintillators for the TPC. Shown are S1,S2,V1,V2 and ST upstream of the detector system. "First pad row of the TPC" refers to the active volume of the TPC.

and posted to the Data Acquisition System, which will be discussed below.

2.4 Laser Calibration

The y components of a track in the TPC are reconstructed by measuring the time of drift of the ionization and the speed of that ionization. The TPC drift field is designed such that it is in a stable region of terminal velocity for the drifting electrons. However, this velocity can also depend on other factors such as gas temperature, atmospheric pressure and gas makeup. These can combine to cause shifts in the drift velocity which will have the effect of distorting the events by scaling the y-axis of the events in an arbitrary way. We therefore, established two systems in the 6 and 8 $A-GeV$ runs to detail this velocity on a run-by-run basis. These systems were composed of laser fiducials in the TPC and a separate drift chamber called the Canary Chamber.

The laser system was established by the EOS experiment to measure the drift velocity in the gas and allow a straight line calibration to correct for magnetic field distortions as discussed in Section 3.2. It comprised a Q-switched Nd:YAG laser that was directed into the TPC at various fiducial positions parallel to the nominal beam axis or z direction in the TPC. The laser beams had been frequency quadrupled from the 1064 nm primary frequency of the Nd:YAG to 266 nm ultra-violet for ionizing the gas. These beams would then ionize the gas along straight lines allowing differences in y position from various beams to be used to calculate the proper drift velocity. The laser was set to trigger at 20-50 pulses every few minutes, but only a few of these per run would be saved to tape. The TPC would be triggered as though there had been an interaction, but the event would have a special flag in the CAMAC table designating it as a laser firing. This allowed the laser to be treated in the same way as the real data.

The canary chamber worked on nearly the same principle. A small nitrogen laser ($5\,mW$ $337\,nm$) would cause photo-emission from an aluminum bar at the top of the drift region and a pad at the bottom. The difference in the time of the two arriving signals and the known difference in their generation points allowed the calculation of the drift velocity. The canary chamber was an independent measure of the drift velocity from the TPC electronics. It did, however, have a different gas supply although it was obtained from the same gas lot.

A third method was also employed to achieve the drift velocity. The top of the TPC forms a natural barrier or limit to the active region of the TPC. As tracks travel through the walls of the gas containment region they simply disappear. Averaged over many events the disappearance of the tracks as they approach the top of the TPC (a well known position) can be used to establish the length required for the drift velocity calculation. This is how the 2 and 4 $A-GeV$ data sets were calibrated. A plot of the drift velocities used are displayed in Fig. 2.8.

2.5 Data Acquisition

Once the data was accumulated for the event on the TPC's SCAs it was the job of the data acquisition system to transfer the data to tape for offline data processing. The data from the TPC consisted of ~ 130 time intervals by 15360 pads for the TPC. In addition to the TPC, there was 12 CAMAC modules(scalers, ADC's, TDC's) that registered the signals from the beam profiling, triggering scintillators and the clock signals from the canary chamber. First the SCA information of each pad, which is in an analog format, would be multiplexed at 64:1 and off loaded into one of 128 ADCs. After conversion the data was transferred out of the TPC electronics bay directly below the pad plane via 128 fiber optic cables to a set of VME crates. The VME

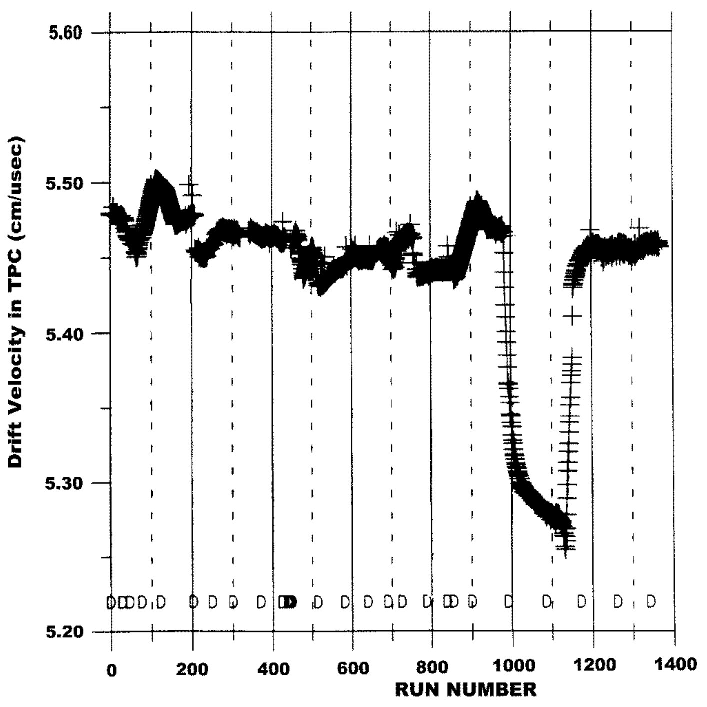

Figure 2.8: Drift velocity of electrons as a function of run number. Note that the D's indicate breaks in the data taking. Courtesy of Jim Draper.

crates removed pedestals combined the event structure and posted the data set to the tape queue system. The tape queue system was composed of 3 DLT tape drives which would be sequentially polled for the ability to take the event that had been buffered by the VME crates. This was done to relieve the bottleneck in the DAQ created by the fact that the tape drives were much slower than the rest of the system.(2 MB/sec for DLT drives used)

Chapter 3

Processing

3.1 Introduction

In order to begin extracting physics observables certain pre-processing of the events must be completed. The events must first be reconstructed from the raw data that was stored on tape by the DAQ which was discussed in Chapter 2. Then the data must be converted into the tracked and identified particle data used to do the physics calculations. This is done by converting the data to space points or hits and then performing pattern recognition to recover the trajectories from the space point distribution.

3.2 Space Points

First, space points must be reconstructed. The ionization distribution is digitized in three dimensions. The y-axis is aligned along the time or drift direction, the z-axis along the 1.2 cm pitch of the pads in the nominal beam direction, and the x-axis is in the $.8cm$ direction of the pads. Note that this comprised the set of local TPC coordinates that are not directly the physics coordinates (see Section 3.6). The raw ionization is separated into smaller segments called clusters by the incremental subtraction of ADC value from each digitized bin. Then a two dimensional gaussian fit is applied to the clusters. This process of pedestal subtraction continues until a 'good' fit is obtained or a subtraction limit is achieved. Remember for 1 pad hits the hit position is taken to be the center of the pad. In the z direction the hit position is always taken to be the center of the pad as this is generally in the track's propagation direction and therefore, does not make distinct hits. The fit establishes the location in the time or y direction and the position in the x direction. This then creates a space of hits in which the tracking algorithm can work. Before the tracking algorithms are applied, the hit space must be corrected for magnetic field distortions. As the electrons drift due to the **E** field they will follow a trajectory given by the Langevin relation

$$\vec{v_D} = \frac{\mu E}{1 + \omega^2 \tau^2} \cdot [\hat{E} + \omega\tau \widehat{\vec{E} \times \vec{B}} + \omega^2 \tau^2 (\hat{E} \cdot \hat{B}) \hat{B}] \tag{3.1}$$

For values of $\omega\tau$ (4.1 from [Drap97]) that are large the third component dominates. The electrons then trace the **B** magnetic field lines following a curved path to the pad plane (typically it is harder to create a uniform magnetic field than a uniform **E** field). This will cause a false position due to the straight line assumption used by the calculation of the y position (drift velocity × drift time = y). The hits are, therefore, corrected using a magnetic field map to calculate their true position and then checked by testing the straightness of the laser tracks as discussed in Chapter 2.

3.3 Tracking

After hitfinding the tracking can be done. The algorithm is based on a Kalman-Filter. It starts at the last pad row where the tracks are presumed to have their best separation and begins by finding 'spores'. A spore is found by taking each of the hits in the last pad row and projecting back toward the target. One then looks in the next-to-last pad row for another hit nearby this trajectory (within 3.2 cm). If one is found then a straight line determined by these two is followed back to the next pad row and so on until five hits are found at < 1 cm distance from the projection. This then becomes a spore. After the spore is found, the tracking software then applies the magnetic field map and fits the 5 points to a helix. The helix is then systematically projected back along each pad row absorbing nearby hits until it fails to find a hit for 8 rows. If the spore has been extended to 7 or more hits it becomes a track. As hits are assigned to tracks they are flagged and removed from the hit space for the next track. This removal insures that single hits are not multiply assigned. After each hit is assigned to the track the helix is redetermined using all of the hits assigned to it before projecting to the next pad row. Left over hits at each pad row are then used to form new spores and then tracked. Once all of the potential spores have had attempts made to extend them into tracks the tracking pass is complete. An additional complication arises at this point. The 2-dimensional gaussian used to fit the hits is actually dependent on the track's direction because of the angular dependence of the drift and diffusion discussed in Chapter 2. The widths used in the gaussian fit are actually calculated from the rough drift distance and diffusion relations. The angle dependence is not known in advance of the ionization's assignment to a track. In order to correct for this, to get a better fit from the tracking software, the hitfinding and tracking are redone using the track information from the first pass. This essentially means that Equations 2.7 are used to modify the fit widths.

3.4 Particle Identification

After tracking is completed we can then perform the particle identification necessary to our study. We begin by taking the accumulated dE/dx signals of the hits associated with each track. It should be noted that there will be no correction for threshold effects due to pedestal subtraction on the ADC value as in [Brad97]. This is because the value of the dE/dx is actually obtained from the integration of the gaussian fit found by the space point reconstruction and, therefore, accounts for the truncation of the ionization tails do to noise pedestal subtraction. It is known that this track dE/dx distribution is Landau, due to the improbable high energy electron tail from delta rays (hard scatters). In order to fit the distribution to quantify the average energy loss of the track in a timely manner we perform a truncated mean analysis. We performed a truncated mean by first removing the top 30% and the lower 10% of the dE/dx ADC spectrum from the hits associated with the tracks. Next, we assume that the remaining distribution is gaussian-like and take its mean value as the mean energy loss of the track in the gas. Plotting these value versus rigidity (Eq. (2.2)) we can get the well known curves of Bethe-Block seen in Fig. 3.1. One can easily see the species separation in this plot, but one can also see significant overlapping of the particle bands. In an attempt to reduce the effect of the overlapping bands and allow quantitative measures of the interspecies contamination, a complex particle identification procedure was developed as reported by [Klay98].

First particle species were identified in areas were they were clearly separated. This set of particles is fit with gaussians for their centroids in mean dE/dx as a function of narrow rigidity bins. These values were plotted versus the calculated $\beta\gamma$ of the particle. This makes the universal energy loss curve of Bethe-Block shown in Fig. 3.2. From this curve we can fit a Bethe-Block parameterization Eq. (3.2). There is a finite gain in the TPC, as was mentioned in Chapter 2 the TPC is designed to have high linearity for signals up to a maximum of 90 times that of the minimum ionizing. As a result it is possible to begin to saturate the gain for the highest ionizing particles. A correction for this saturation was emperically developed by Scott [Scot97] and is shown in Eq. (3.3). The arbitrary units of dE/dx are the same as those of Fig. 3.1.

$$\frac{dE}{dx} = \frac{\zeta}{\beta^2}(\kappa + \log((\beta\gamma)^2) - 2\beta^2) \tag{3.2}$$

$$\frac{dE'}{dx} = \frac{dE}{dx}(A\log(\frac{dE}{dx}10^{-6}) + B) \tag{3.3}$$

This allows the particle band centroids to be tracked on the dE/dx versus rigidity plot even where there is overlap. The dE/dx versus rigidity spectrum can then be refit fixing the centroid of each PID band and finding the amplitude of the multiple gaussians of the bands as they extend into the overlap regions shown in Fig. 3.3. With this information (centroid, width and amplitude) for each species' band, particles can have a probabilistic PID assignment based on their location with respect to each

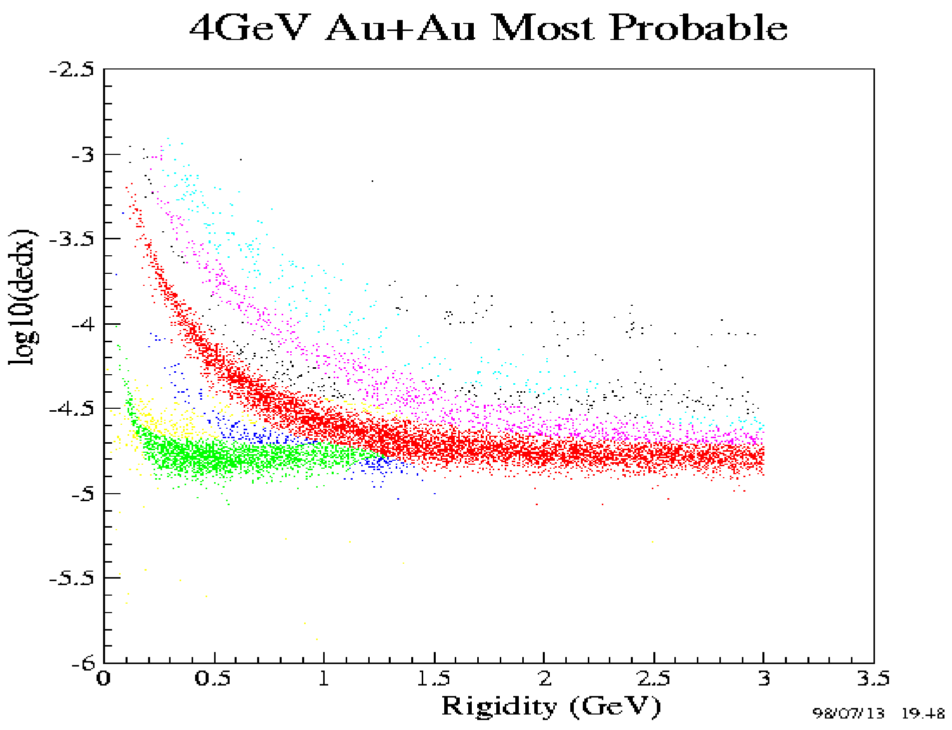

Figure 3.1: The plot shows the identified particle bands for a typical data set at 4 $A - GeV$. Only positively charged species are shown. Each particle is displayed associated with its highest probability band. Starting in the lower left corner the bands are, π^+, K^+, protons, deuterons, and etc. Courtesy Jenn Klay.

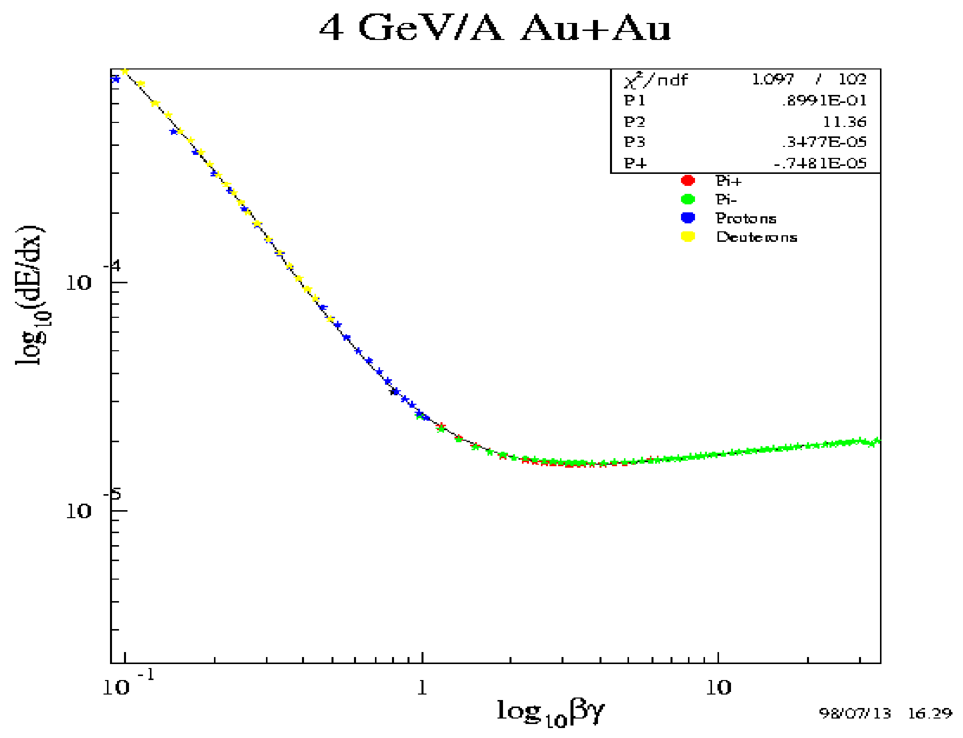

Figure 3.2: Universal curve of the Bethe-Block (parameterization is described in the text). Note that several different species are plotted on the single curve. The different species are fit only in regions of clear identification, but the set allows for the complete determination of the curve. Courtesy Jenn Klay.

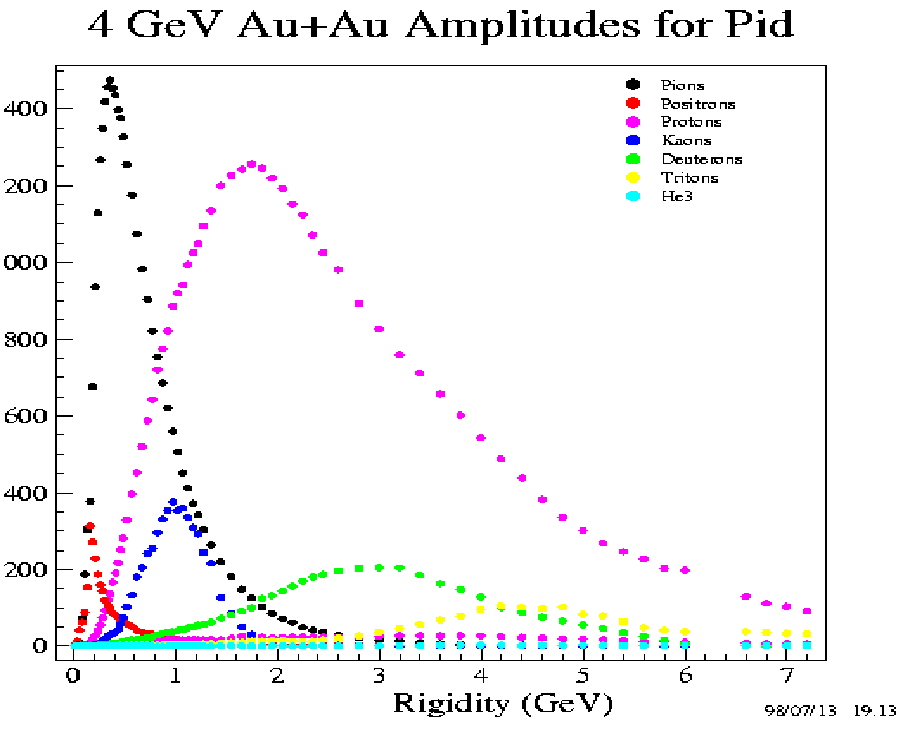

Figure 3.3: Amplitude spectrum for the various species for a typical 4 $A - GeV$ data set. The amplitudes are combined with the width and centroid information to generate the particle's probabilistic identification. Courtesy Jenn Klay.

species' band. This results in the colored bands in Fig. 3.1. These bands are the identified particles that will be used in this analysis respectively. Although one can use this probability as a weighting function for particle spectra and other observables to track through the overlap regions, it is not useful in flow analysis directly. This is because the different species carry different directivity with respect to the reaction plane. This information gets overwhelmed by misidentification. This procedure does, however, allow us to determine our amount of contamination near the overlap regions and limit its effects. Once the species has been identified in this manner, the particle's kinematics can be determined. Note, that up until PID has been established we do not know the particle's mass or charge.

3.5 Vertexing

After the tracking pass is completed the event vertex is determined. This is important for several reasons. The first reason is that the vertex will be a well determined point in space that all tracks related to the event should have in common. It can therefore, be used to insure that the event was target related and that each track is event related. The primary vertex is also used for improving the momentum determination for each track as will be described below. All of the tracks found in an event are projected back through the target plane using their helix fits. A procedure is used to find the common point for which the sum of the squares of the distances of closest approach of all the tracks is a minimum. This method is susceptible to

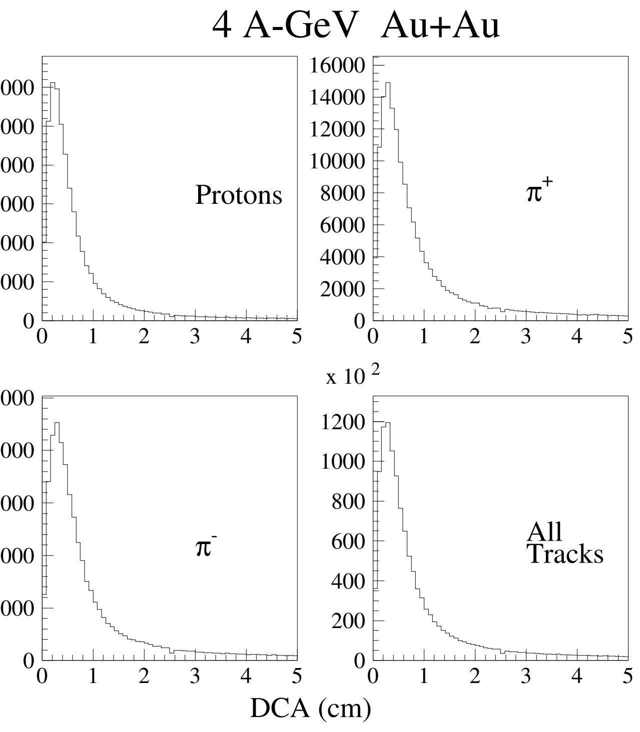

Figure 3.4: DCA (Distance of Closest Approach). Each of the four panels displays the spectrum of the 3-dimensional distance to the vertex of event. The information can then be used to separate out secondary particles. A typical cut is $\leq 2.0\,cm$

distortion due to outliers, therefore, the track the farthest from this point is then rejected from the fit and the remaining ensemble refit. This continues until all of the remaining tracks have a distance of closest approach of $2.5\,cm$ or less to the fitted point. The point is then declared the vertex and all tracks are refit using the vertex for their distance of closest approach (DCA).

The DCA (Fig. 3.4) can then be used to distinguish direct target related tracks from decay products and false tracks. The vertex point determined can be used to eliminate events that were not target related. Figure 3.5 shows a distribution of these found points. Remember that the ST scintillator was $\sim 1\,cm$ away and, therefore, can be distinguished. These two distributions are used to make important cuts on the data.

In addition, the vertex point can be used to aid the momentum resolution of the tracks. This is because the vertex point is well determined by using all of the tracks and is $\sim 13\,cm$ upstream of the first pad row. It can be included as one final point for the refit of the tracks for their helix parameters there-by, improving the momentum resolution.

3.6 Beam Vector

As was mentioned earlier, the TPC resolves the event in the TPC coordinate frame. This is not necessarily the physics frame. In order to move into our physics frame we must determine the beam axis and impact parameter. It is very difficult to specify the exact location of the beam in an actively running facility with respect to the detector system. Extensive surveys were conducted of the experimental area and beam line to define the fiducial marks of the TPC in the laboratory. These must then also be related to the TPC coordinates. We, however, were unable to determine the exact beam location in the beam pipe to sufficient accuracy with respect to the fiducials of the TPC. To compensate for this, we developed an alternative technique. The data sets taken consisted of, among other things, runs of low gain beam trigger data. These data were essentially from a raw beam trigger *i.e.* $S1{\cdot}\overline{V1}{\cdot}\overline{V2}$

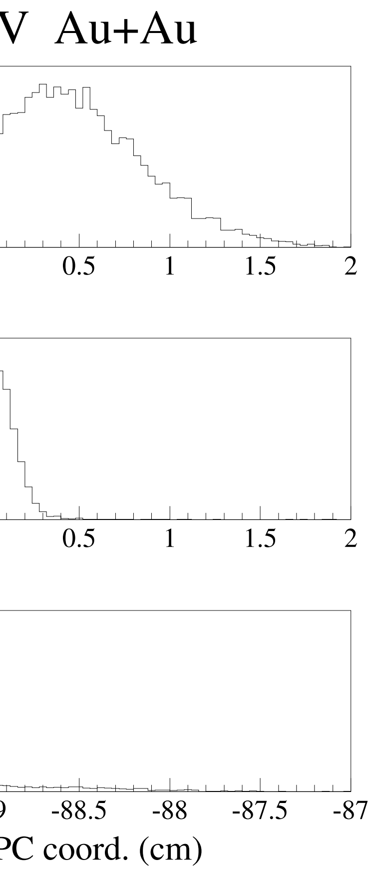

Figure 3.5: The three panels display the distribution of found vertex positions in the x, y and z-axis respectively down the page. The distributions can then be cut upon to remove non-target related events. Typical cuts would be mean ±1.0 cm in x and mean ±.3 to .5 in y and z dimensions.

(with no ST signal in the logic determining the trigger) discussed in Chapter 2. The low gain was accomplished by turning down the voltage on the anodes of the multiwire multiplication region of the TPC. The combination of these two allowed for the tracking of the raw beam through the TPC. With this tracking of the raw uninteracted beam through the TPC we could then determine its location with respect to the TPC in the TPC's coordinate frame. A small correction due to the change in angle of the beam from bending in the magnetic field from the target to the sensitive region of the TPC was necessary. The correction was calculated in the following manner. First the beam angle with respect to each pad plane was determined by the tracking software. Then a curvature ratio was found from the change in the angle versus distance in z travel via the pad planes

$$\frac{\alpha_i - \alpha_{i+10}}{10 \times 1.2cm} \times 13cm = \alpha_{vertex} \tag{3.4}$$

Note that the α angle (angle in the bend plane of the magnet) only was corrected. The λ angle does not curve due to the magnetic field and, therefore, was kept at a constant. Table 3.1 shows a compilation of this study. Once this vector was found the events were then rotated to this frame for further analysis.

3.7 Q-Vector

We next must determine the direction of the impact parameter vector by reconstructing it from the data. The impact parameter is defined as the vector perpen-

Energy	α_{vertex} (degrees)	λ (degrees)
2	-1.01	-.1
4	-.15	-.08
6	.52	-.13
8	-.5	0.0

Table 3.1: Nominal beam angles as tracked through the TPC in degrees for the four incident beam energies. The two angles are defined such that α is the crossing angle in the bend plane of the magnet, λ is the dip angle, and 0° is in the nominal beam direction.

dicular to the direction of travel of the projectile to the center of the target nucleus. The magnitude of the impact parameter will be discussed in the next section. It is believed that the flow signal is due to the compression and repulsion dynamics of the collision that are symmetric about the impact parameter. We therefore can determine the reaction plane by measuring a crude flow signal. This method was first outlined by [Dani85]. The method known as the Q-vector method calculates the anisotropy axis of the event.

$$\vec{Q} = \sum_{i=1}^{N} w(y_i)\vec{p_{i\perp}} \tag{3.5}$$

Here N stands for the number of tracks used to determine the reaction plane. For our purposes this means protons, deuterons and tritons as they all show similar flow characteristics. Essentially this Q-vector is calculated from the $P_\perp$ (Transverse Momentum) distribution of the particles. Ordinarily momentum conservation should call for this quantity to be zero but, if an odd function of rapidity (Eq. (3.6)) is chosen the Q-vector can be made nonzero. The original Q-vector method called for a weight that was a simple Θ function of rapidity (-1 backward and $+1$ forward). Rapidity is a scaler quantity related to the velocity of a particle in the beam direction.

$$y = \frac{1}{2} ln \frac{E + P_z}{E - P_z} \tag{3.6}$$

The rapidity is often normalized by

$$y_N = \frac{y_{part} - y_{cm}}{y_{beam} - y_{cm}} \tag{3.7}$$

This then yields an axis that ranges from -1 to +1 with -1 being target rapidity and +1 beam rapidity independent of incident energy. The center of mass is then at 0, resulting in 'backward' or target related being negative rapidity and 'forward' or beam related positive. This weighting then resulted in reflecting the backward half of the reaction over on top of the forward, resulting in a finite Q-vector in the direction of the impact parameter.

For our purposes, due to acceptance issues, we did not want our Q-vector to be $P_\perp$ dependent so we used unit vectors in the direction of $P_\perp$. By using only unit vectors a simple weighting scheme that is independent of $P_\perp$ could be applied to correct for event distortions due to acceptance. This will be discussed in the next chapter. It still has, however, the negative weighting for backward and positive weighting for forward rapidity. The particles used in this distribution were the identified baryons only (please see Section 3.4 for a description of these). The particle species of protons, deuterons, alphas and high order baryons have all been shown to carry the same qualitative distributions with respect to the reaction plane direction [Part97]. Pions exhibit a different behavior and, therefore, are not added to the summation [Kint98].

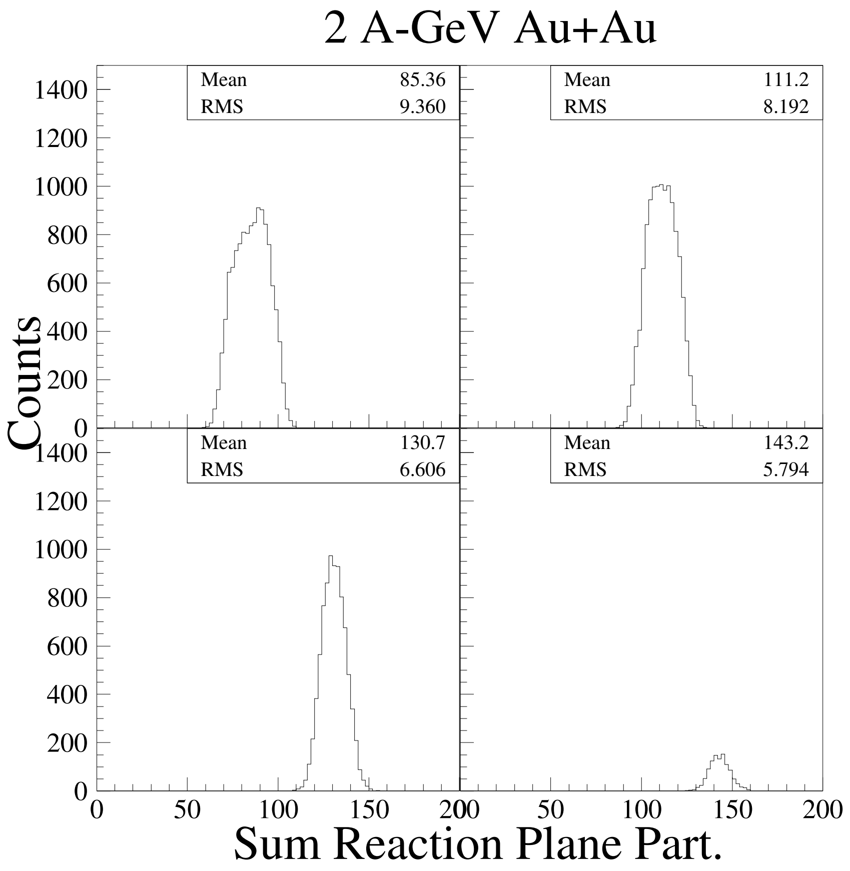

Figure 3.6: Distribution of particles used in determining the Reaction Plane for each of the multiplicity determined impact parameter bins. Shown is a sample from the $4\ A-GeV$ data set.

We want to include as many species as possible so that the determination is not dominated by statistical fluctuations. Figure 3.6 shows one such study of the particle statistics used for the reaction plane determination. Table 3.2 displays the values for each of the energy and multiplicity selections. We must study and understand the resolution of this method in the light of these statistical fluctuations due to the finite event sizes. The most popular method of doing this is to use the so called subevent

Energy	Impact Parameter (fm)	Mean	RMS deviation
2	0-2	143	6
	2-4	130	7
	4-6	111	8
	6-8	85	9
4	0-2	157	8
	2-4	140	9
	4-6	113	10
	6-8	80	11
6	0-2	157	9
	2-4	137	10
	4-6	109	11
	6-8	74	13
8	0-2	159	10
	2-4	140	11
	4-6	110	11
	6-8	74	13

Table 3.2: Catalog of the number of particles used to determine the reaction plane for the various incident energies and impact parameters.

method. The event is split into two subevents by randomly assigning the particles used to determine the reaction plane to one or the other of two groups. The two groups or subevents then have reaction planes determined for each of them. If there is a truly correlated reaction plane in the event then the two subevents reaction planes will also be correlated. To test this, we can plot Φ_1 - Φ_2, the difference between the two determined reaction planes from the subevents. Figure 3.7 shows this test. Using this measure of the resolution one can construct a correction factor for the flow signals due to finite event resolution. This is outlined in [Posk98]. I have reproduced the relevant equations here, where Eq. (3.8) determines the measure of the resolution, Eq. (3.9) determines the correction factor for $\langle P_x \rangle$ and V1. While Eq. (3.10) is used for correction of the V2 or elliptic flow. These signals are described later in Chapter 5.

$$\chi = \sqrt{4.0 \log \frac{1.0}{2(N_{events}(m|\Psi_m^a - \Psi_m^b| > \pi/2)/N_{total})}} \tag{3.8}$$

$$\frac{1}{\langle cos[m(\Psi_m - \Psi_r)] \rangle} = .626657\chi - .09694\chi^3 + .02754\chi^4 - .002283\chi^5 \tag{3.9}$$

$$\frac{1}{\langle cos[2m(\Psi_m - \Psi_r)] \rangle} = .25\chi^2 - .011414\chi^3 - .034726\chi^4 - .006815\chi^5 \tag{3.10}$$

$$m = order\ of\ Fourier \tag{3.11}$$

It should be noted here that all of the data in this document will be corrected for this dispersion of the reaction plane. One must also be careful that this procedure be followed for each event selection made, as the resolution has a multidimensional dependence on multiplicity, particle identifications etc. Table 3.3 presents the resolutions and corresponding correction factors. In the table the "Resolution" represents a measure of the reaction plane resolution. This measure is made by finding the mean value of the $(\Phi_1 - \Phi_2)/2$ distribution and can be used as a very rough approximation of the correction factor (Eq. (3.9) and Eq. (3.10)) by taking its cosine value.

Once the reaction plane has been determined and studied we can then determine the signals of interest with respect to it. These will be discussed in Chapter 5.

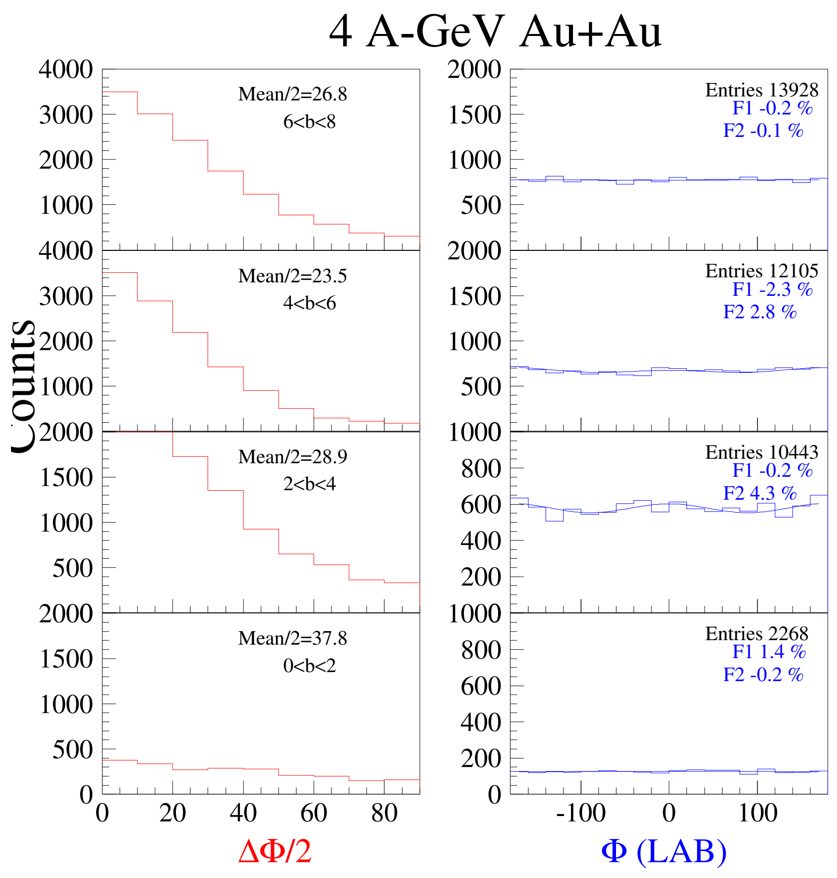

Figure 3.7: Reaction Plane Resolution Test. On the left is the subevent comparison $(\Phi_1 - \Phi_2)/2$ on the right is the reaction plane determined in the lab frame with the weighting for acceptance correction applied and the fit measure of its effect (F1 and F2 the percent of non-flatness as measured by Eq. (4.1) from Section 4.2). Down the page are different centrality selections.

0 20 40 60 80 -100 0 100

0 20 40 60 80 -100 0 100

0 20 40 60 80 -100 0 100

Energy	Impact	Resolution (degrees)	χ	Correction Factor ($\langle P_x \rangle$,V1) Eq. (3.9)	Correction Factor V2 Eq. (3.10)	Multiplicity Range
2	0-2	21	$2.31 \pm .167$	$1.13 \pm .100$	$1.53 \pm .084$	190-
	2-4	18	$2.46 \pm .046$	$1.11 \pm .027$	$1.46 \pm .023$	160-190
	4-6	24	$2.32 \pm .042$	$1.13 \pm .025$	$1.52 \pm .021$	125-160
	6-8	34	$2.27 \pm .037$	$1.13 \pm .022$	$1.55 \pm .018$	85-125
4	0-2	27	$1.69 \pm .1$	$1.27 \pm .060$	$2.12 \pm .050$	260-
	2-4	24	$1.83 \pm .023$	$1.23 \pm .014$	$1.93 \pm .012$	210-260
	4-6	29	$1.74 \pm .021$	$1.26 \pm .013$	$2.05 \pm .011$	155-210
	6-8	38	$1.68 \pm .035$	$1.28 \pm .021$	$2.15 \pm .018$	90-155
6	0-2	34	$1.12 \pm .175$	$1.65 \pm .105$	$3.92 \pm .088$	285-
	2-4	30	$1.25 \pm .093$	$1.52 \pm .056$	$3.27 \pm .047$	230-285
	4-6	33	$1.23 \pm .062$	$1.54 \pm .037$	$3.36 \pm .031$	170-230
	6-8	41	$1.18 \pm .051$	$1.59 \pm .031$	$3.59 \pm .026$	95-170
8	0-2	38	$.74 \pm .428$	$2.31 \pm .257$	$8.09 \pm .214$	320-
	2-4	37	$.78 \pm .165$	$2.21 \pm .099$	$7.41 \pm .083$	260-320
	4-6	39	$.74 \pm .104$	$2.30 \pm .062$	$8.03 \pm .052$	190-260
	6-8	43	$.73 \pm .086$	$2.34 \pm .052$	$8.35 \pm .043$	105-190

Table 3.3: List of correction factors, Correction given by Eq. (3.9) where χ is found by Eq. (3.8). Also displayed are the multiplicity cuts for each of the impact parameter bins. See Section 3.8 for discussion of these cuts. Note that for example in column 3 the 6 $A-GeV$ (41) and the 8 $A-GeV$ (39,43) do not agree with the correction factors, presumably because the distributions of V1 and V2 are very different fot the two energies in those bins.

3.8 Impact Parameter

In the above discussion we were able to determine the direction of the impact parameter that is used with the beam vector as the reaction plane. The other component of the impact parameter vector, it's magnitude, can also be used as a probe to flow dynamics. With control of the trigger system as outlined in Chapter 2 we were able to take a variety of centrality selections (impact parameter ranges).

We can not directly measure the impact parameter in heavy ion collisions. In order to determine this vector we have to make some assumptions. We assume that the event multiplicities vary monotonically with the magnitude of the impact parameter. We then use the event multiplicities to determine the impact parameters magnitude. With a very simple geometric model for the nucleus cross section and the multiplicity distribution we can calculate impact parameter ranges for study. This is shown in Appendix E. We will use the scalers that were recorded during the run to determine the cross section (trigger) and the TPC will be used to determine the multiplicity distribution.

The scaler information (stored from the various triggering scintillators discussed in Chapter 2) is used to determine the trigger cross section σ_{trig} (See Appendix E) for details on this). Next we decide on a window of impact parameter that we desire to investigate by choosing the radius values (for the window) and calculating the geometric cross section of interest with Eq. (3.12). The ratio of the two can then be used to set the multiplicity selections with Eq. (3.13).

$$\sigma_{geo} = \pi r^2 \tag{3.12}$$

$$\frac{\sigma_{M_c}}{\sigma} = \frac{\int_{M_c}^{MAX} \frac{dN}{dm} dm}{\int_0^{MAX} \frac{dN}{dm} dm} \tag{3.13}$$

Where in Eq. (3.13) the integration of the multiplicity distribution is from its maximum value down to a multiplicity value that determines the proper ratio of the two cross sections. Once this iterative process is complete the values are used to make selections (or "cuts") on the data for study. Figure 3.8 shows the various multiplicity distributions and cut values for the energy ranges studied.

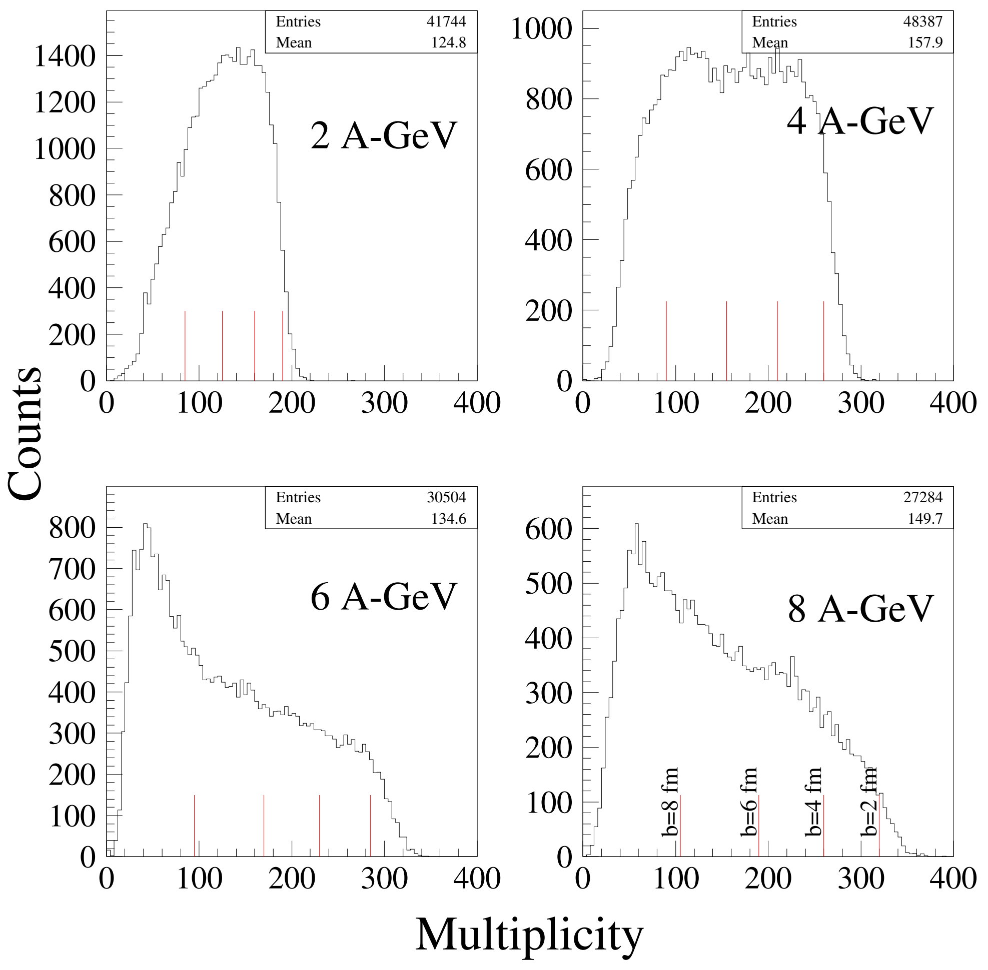

Figure 3.8: Multiplicity distributions for the analyzed "min bias" data sets at 2,4,6 and $8\,A-GeV$ nominal incident beam energies. Also displayed are the cut boundaries between each of the cross section determined impact parameters. See appendix E for details on the cuts used.

Chapter 4

Calibration

4.1 Introduction

In order to interpret and study the results from the TPC, care must be taken not to introduce artificial event distortions. Due to imperfect detection and reconstruction of particles, detector based anisotropies are produced. In order to analyze the flow signals of the events these distortions must be studied and attempts made to limit there effects on the results. In this chapter, I discuss how I measure and attempt to correct for event anisotropies using the data itself.

4.2 Reaction Plane Correction

Theoretically, the event planes should be completely random with respect to an azimuthal angle defined in the laboratory frame. Therefore, distributions of the found reaction plane angles with respect to a fixed angle in the laboratory should be flat. Any non-flatness behavior of the found reaction planes in the laboratory frame is an indication of a systematic distortion of the events. As seen in Fig. 4.2 significant distortion is seen in the raw data. To correct for this, we assume that the events should have had an azimuthally isotropic distribution of particles in the laboratory frame. We then bin the particle distributions used for determining the reaction plane into Φ_{lab}(the azimuth angle with respect to the laboratory), rapidity y_N, and multiplicity of the event. If there are no distortions in the data, then averaged over many events there should be no difference for particles scattered at different angles within the same rapidity and centrality window. A weighting function is developed based on the occupation of the various Φ_{lab} bins. A typical weighting function is shown in Fig. 4.1. This weighting function is then applied to the data to modify the rapidity weighting of the Q-vector method to negate the effect of artificial event plane bias. The results are shown in Fig. 4.2. The flatness of the found reaction plane with respect to the laboratory is important due to the fact that any distortion of this nature leads to a false enhancement of the flow signal. Once the reaction plane is made flat, then the event structures can be projected onto the reaction plane without being artificially distorted by the Φ_{lab} azimuthal acceptance. To quantify the success of removing the distortions in the reaction plane determination we fit the distribution of found reaction planes to

$$\frac{dN}{d\Phi} = F_0(1 + F_1(cos(\Phi))/100 + F_2(cos(2\Phi))/100) \tag{4.1}$$

This allows quantitative measurement of the flatness, and a typical set was displayed in Fig. 3.7 in Chapter 3. Table 4.1 shows all of the fits gathered together. Due to the small values of this measure I display and catalog the values of F1 and F2 as percentages. Note that the effect of a given F1 on the flow is expected to be small. For detailed plots of the acceptance functions for all of the energies, the reaction plane resolutions and measured flatness (F1 and F2) see Appendix A.

Only the particles used to determine the reaction plane are weighted in this manner. Once the reaction plane is found, the projections are not weighted in this way. This is due to the fact that if the reaction planes are truly random then any distortion

Figure 4.1: Displayed is a typical weighting function used to correct for azimuthal anisotropies, due to acceptance, when determining the reaction plane of the event.

in the Φ_{lab} azimuth will be averaged over. Therefore, weighting versus no weighting of the projections produces nearly the same numarical result. This averaging removes nearly any net effect on the flow signal when averaged over many events.

4.3 Transverse Momentum Correction

Acceptance in the forward rapidity region is different from the backward region. However, in a symmetric system this should be symmetric. This idea is used to correct the $P_\perp$ distribution of the particles. I follow the same scenario mentioned above, bin the particles in y_N, $P_\perp$, and Φ. In this instance the Φ binning is in Φ_{flow} (with respect to the reaction plane), not in the lab frame. Theoretically, a symmetric

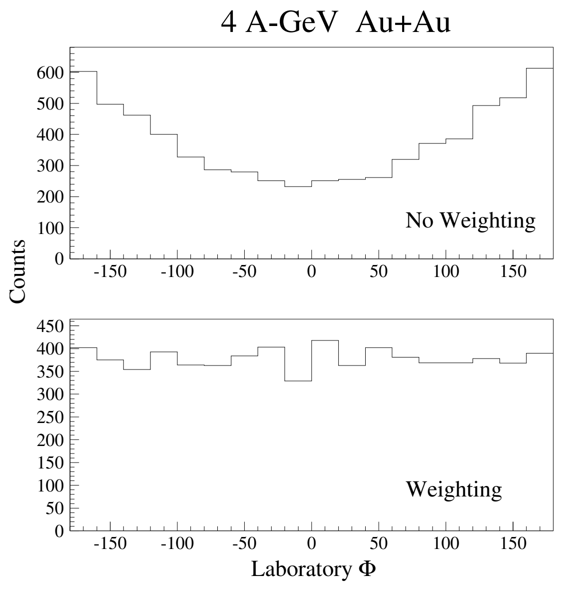

Figure 4.2: The upper panel shows the distribution of found reaction planes without any correction for acceptance. The lower panel shows the effect of the acceptance correction.

collision should scatter as many particles at a given angle on the projectile side of midrapidity as on the target side of midrapidity with a 180° rotation from projectile to target side. This symmetry is in the frame of the reaction plane and, therefore, the need to bin in Φ_{flow}. Figure 4.3 is a cartoon of this effect for discussion.

Note that the $P_\perp$ distributions are a function of the rapidity with respect to the center of mass. That is, one unit of rapidity forward of center of mass should look the same as one unit backward of center with the 180° rotation in Φ_{flow}. I therefore, can bin all of the particles of a given species in $P_\perp$, y_N, and Φ_{flow} and compare the mirror images forward and backward. Differences from forward and backward rapidity comparisons are then used to build another weighting function used to correct for $P_\perp$

Energy	Impact Parameter (fm)	F1 %	F2 %
2	0-2	0.0	-2.7
	2-4	-.8	5.2
	4-6	-.9	2.8
	6-8	-5.6	3.5
4	0-2	1.4	-.2
	2-4	-.2	4.3
	4-6	-2.3	2.0
	6-8	-.2	-.1
6	0-2	-3.5	-4.7
	2-4	-1.0	1.6
	4-6	-1.1	3.5
	6-8	-1.4	-1.5
8	0-2	-7	.2
	2-4	0.0	-1.6
	4-6	1.0	2.9
	6-8	.6	2.5

Table 4.1: Catalog reaction plane flatness achieved through calibration. Columns 3 and 4 are determined by the fit of $\frac{dN}{d\Phi} = F_0(1 + F_1(cos(\Phi))/100 + F_2(cos(2\Phi))/100)$ to the $dN/d\Phi_{lab}$ to the distribution of the found reaction plane in the laboratory frame (i.e. the right hand side of Fig. 3.7).

distortions. One thing to note here is that the method assumes that either the forward or backward bin has 100% efficiency. Figure 4.4 shows the result of the correction as a function of $P_\perp$.

What we note here is that the TPC has competing acceptance effects. The forward direction of the TPC is hindered by two track resolution below a $P_\perp$ of 450 MeV/c for protons in the most forward rapidities. This creates a hole in the $P_\perp$ distribution in the forward direction. In the backward direction the particle spectrum is limited by the geometrical acceptance of the TPC. That is, above about 60° in the lab frame

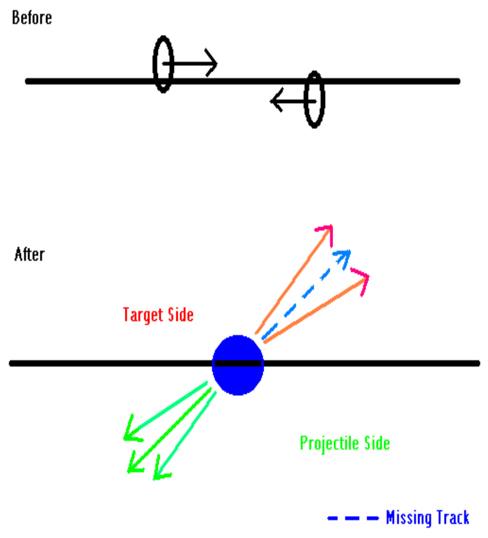

Figure 4.3: Here is a cartoon demonstrating the symmetry exploited in the $P_\perp$ calibration. The dotted track indicates a lost track based on the comparison of forward (projectile) and backward (target) occupation statistics

the particles no longer scatter into the active region of the TPC. This creates an acceptance hole above a $P_\perp$ of about $250\,MeV/c$. The corrections scheme then takes advantage of the areas of good acceptance in the forward versus backward direction. It should be noted that the acceptance near midrapidity is better as can be seen in Fig. 4.4.

Appendices B, C, and D show all of the $P_\perp$ acceptance distributions for protons, π^+, and π^- respectively.

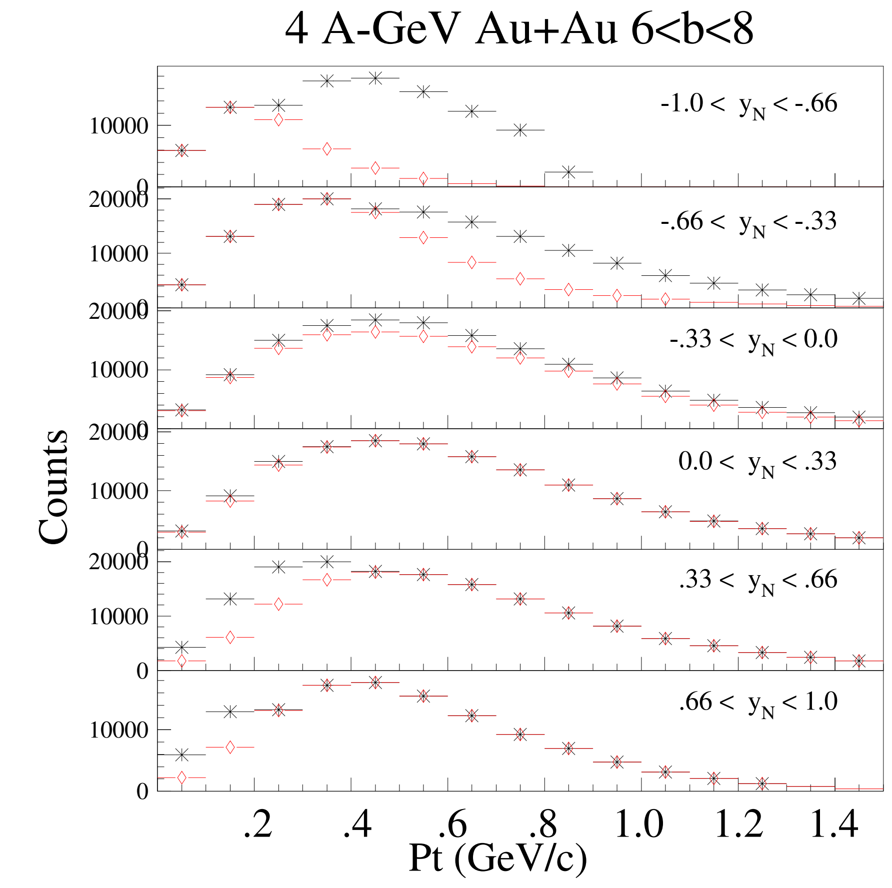

Figure 4.4: $P_\perp$ acceptance shown for $4A-GeV$ proton, in the $6-8\,fm$ bin. Down the page are the 6 rapidity binnings used in the S-curves. *'s represent corrected data, diamonds uncorrected or raw data. Note that the plot is integrated over the Φ_{flow} dependence.

4.4 S-curve Weighting

In addition to the above weighting schemes which attempt to remove distortions, one additional weight was applied. The reaction plane is found through the weighting of the rapidity distribution as mentioned in Section 3.7. In order to improve the efficiency of this weighting function we used the S-curve shape as a guide. Looking to Fig. 5.1 we can see that the flow signal follows this S like curve as a function of rapidity. I therefore give stronger weighting when determining the reaction plane to particles in rapidity windows that exhibit the most flow. The weight function is actually the normalized strength of the flow signal as determined by a first pass flow measurement.

Chapter 5

Flow Signals

5.1 Flow Signals

Once we have the reaction plane on an event-by-event basis, we can then set about calculating our various flow signals. I will begin with the traditional signal, the mean transverse momentum, or $\langle P_{x'} \rangle / m$, with respect to the reaction plane. This method has been studied in [Kint97], [Part97], [Pink96] and others. More recently several other signals have been explored most notably the Fourier Component Method. This method was studied by [Appl98], [Barr97] and [Olli95]. The fundamental difference between these two measures of flow is the momentum weighting of the $\langle P_{x'} \rangle$ method. The first fourier memoment is a measure of the population or "number" anisotropy where as the $\langle P_{x'} \rangle$ method measures the $P_\perp$ weighted population anisotropy. I will outline each of these methods here.

5.2 Transverse Method

First we will discuss the traditional flow measurement method. This method, sometimes called directed or sideward flow, is the observation of anisotropic event shapes when $< P_\perp >$ is projected onto the reaction plane. To calculate this quantity we take the reaction plane determined in Chapter 3 and rotate all of the events to this common coordinate system. Note that the corrections of Chapter 4 are always applied. By definition of the x'-axis, the reaction planes are rotated such that the Q-vector found is aligned with the x'-axis. The y'-axis is then perpendicular to the

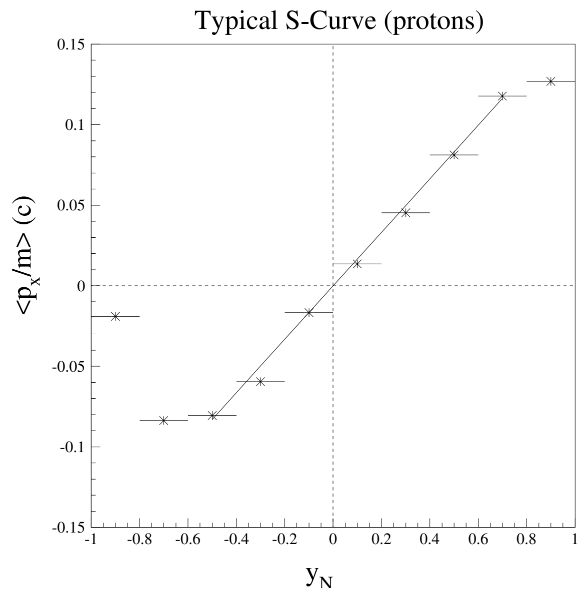

Figure 5.1: This is a typical S-Curve with a linear fit through the mid-rapidity point.

reaction plane. We then analyze the particle $P_\perp$ distribution in Φ_{flow} with respect to the reaction plane as a function of rapidity as defined by Eq. (3.6). We essentially sum up all of the particle projections onto the reaction plane and take the average of the projections. When plotted versus rapidity the net result is the S-Curve shown in Fig. 5.1.

The signal can then be quantified by fitting the S-Curve distribution to a line or function at the midrapidity ($y_N = 0$) point where there should be a (0,0) crossing due to the symmetry of the event. This method can be applied to a variety of event selections which then can be compared. Event selections will be discussed in a later section. I should note that rotating all of the events such that their flow planes are aligned along the x'-axis, places the anisotropy of the events in this direction. The

y'-axis should then be symmetric and display no flow signal if a projection of the particles is made against it. This was checked and found to be true.

The corrections of Chapter 4 (reaction plane weighting and acceptance correction for the $P_\perp$ distribution) will of course have been applied to the reaction plane to effect the removal of distortions in the Φ azimuth. $P_\perp$ distortions as mentioned in Chapter 4 are not averaged out. We use the $P_\perp$ weighting function here to remove these distortions. This is accomplished by modifying the $P_\perp$ values with the weighting function in the calculation of the $< P_{x'} >$.

$$< P_{x'} >= \frac{\sum_{i=1}^{N} w_{P_{\perp i}} \vec{P_{\perp}}_i sin(\Phi_i)}{N} \tag{5.1}$$

There is one additional complication to the calculation. In Eq. (5.1) the reaction plane for particle "i" is obtained by omitting particle "i", otherwise a falsely large flow is found. This is called auto-correlation. This is necessary only for the protons as it is included in the determination of the reaction plane. This is not the case for pions because pions are not used to find the reaction plane.

5.3 Fourier Method

The next method is to deconvolve the event shape by Fourier components. Essentially the events are once again rotated such that they have a common reaction plane. Next, the particles distribution $\frac{dN}{d\Phi}$ is studied via Fourier components.

$$\frac{dN}{d\Phi} = \sum_{n=0} 2v_n cos(n\Phi) \quad (5.2)$$

A typical distribution is displayed in Fig. 5.2 and one can see the development of particles concentrated at 0° (in the flow plane) as the rapidity space is traversed from backward to forward down the page. For comparison to the more traditional methods the v_1 component can be related to the directed flow of the event and one aspect of the v_2 component can be related to the squeeze out or elliptic flow of the event. We are interested here to once again study this signal as a function of rapidity and in addition as a function of $P_\perp$.

This method is essentially looking at the population density as a function of Φ with respect to the reaction plane. Acceptance distortions in the $P_\perp$ dimension will distort this signal. So the $P_\perp$ weighting of Fig. 4.4 is applied here as well. This is accomplished by weighting each particle as it is added to the histogram depicting all the particles with respect to the reaction plane as is in Figure 5.2. Then the fit of the data (Fourier Deconvolution) is performed.

The V2 signal is rapidity dependent and is maximum at midrapidity in the experiments to date. Therefore, the V2 component fit is done for a narrow ($\pm .1$) window in rapidity y_N to minimize the V1 contribution. As you can see from the typical $\langle P_{x'} \rangle$ (Fig. 5.1) and V1 (Fig. 5.2) distributions these signals are small in this narrow window. Figure 5.3 then shows the Fourier fit to this narrow window in rapidity. We can then easily see the elliptic flow effect of preferential particle emission out of the

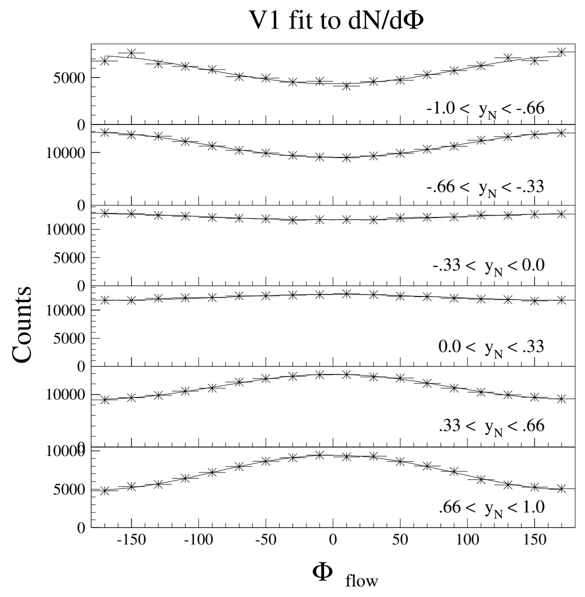

Figure 5.2: This is a typical V1 fit to the dN/$d\Phi$ spectrum of the particles. The six panels downwards represent each of the 6 rapidity bins of the S-like curves shown in Figures 6.15, 6.16, 6.17 and 6.18. The displayed V1 values from the fit are -.13,-.10,-.02,.02,.10,and .16 downwards.

-150 -100 -50 0 50 100 150

-150 -100 -50 0 50 100 150

-150 -100 -50 0 50 100 150

-150 -100 -50 0 50 100 150

-150 -100 -50 0 50 100 150

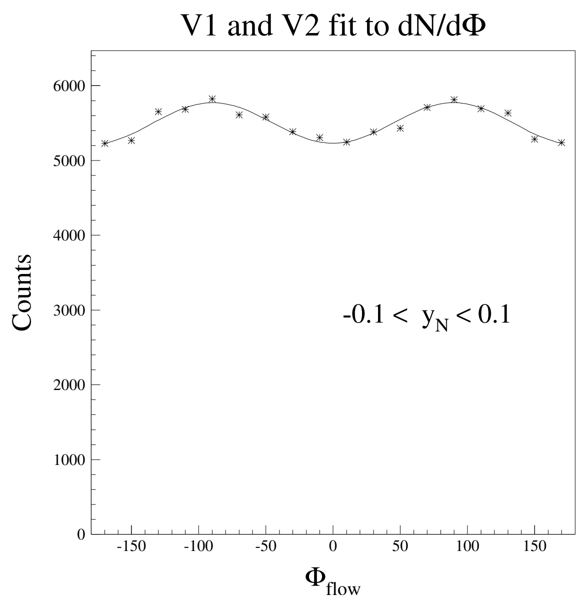

Figure 5.3: This is a typical V2 fit to the dN/$d\Phi$ spectrum of the particles in a narrow midrapidity window of ±.1. One can easily see the enhancement of particle emission at ±90° indicating elliptical flow. The graph displays a V2 of $-3.6 \pm .3$ %.

reaction plane at ±90°.

Chapter 6

Results

6.1 Results

In this chapter we have compiled the results of the various observables previously discussed. We will also present the various details that pertain to each of the observables. The next chapter will attempt to study the observables presented here in the light of theories and event models.

6.2 Directed Flow $\langle P_x \rangle$

The traditional method of measuring flow, $\langle P_{x'} \rangle$ is presented here for protons, π^+s, and π^-s. The data has been corrected for reaction plane dispersion, and $P_\perp$ inefficiencies.

6.2.1 Protons

First we will discuss the proton results for comparative purposes. Figures 6.1, 6.2, 6.3 and 6.4 show the S-curves for each of the incident energies of the experiment. It should be noted that the error bars in the plots (often smaller than the plot symbols) are statistical in nature and are only modified by the uncertanty of the reaction plane resolution correction factor. Also, linear fits to quantify the flow of the S-curves have been made with a fixed y intercept of zero.

We see several trends here. As we change the centrality of the collisions (as measured by the method discussed in Section 3.8) we see that the protons experience a maximum flow in the mid-central bin of $4-6\,fm$. This mid-central peaking of the proton flow signal has been observed by several other experiments [Part97], [Barr97]. It should be noted here that the y-axis of the flow plots has been normalized by dividing by the mass of the particle under consideration. Flow as originally studied is believed to be a velocity dependent variable, by dividing the momentum by the mass it is easier to plot the various observables for the different species on the the same axis. Qualitatively we see that the data are reasonably symmetric from forward to backward in rapidity indicating that the acceptance has been reasonably accounted for. We also see that the S-curve crosses nicely at midrapidity, again indicating that the acceptance has been addressed. The flow values presented in each of the plots will be accumulated in summary plots and tables, later in the chapter. It should also be noted that the protons used in the S-curves have been handled correctly with respect to autocorrelation.

6.2.2 π^+

Now we will discuss the traditional $\langle P_{x'} \rangle/m$ S-curves of the π^+. Figures 6.5, 6.6, 6.7 and 6.8 display these curves. First we note that the signal is inverted from that of the protons, showing the anti-flow behavior of the pions. Note that the pions are projected onto the same plane determined by the protons. Next we note that the pion signal is smaller than the proton signal for all energies. We can also see that the pion signal has no maximum flow value. As we increase to more peripheral impact

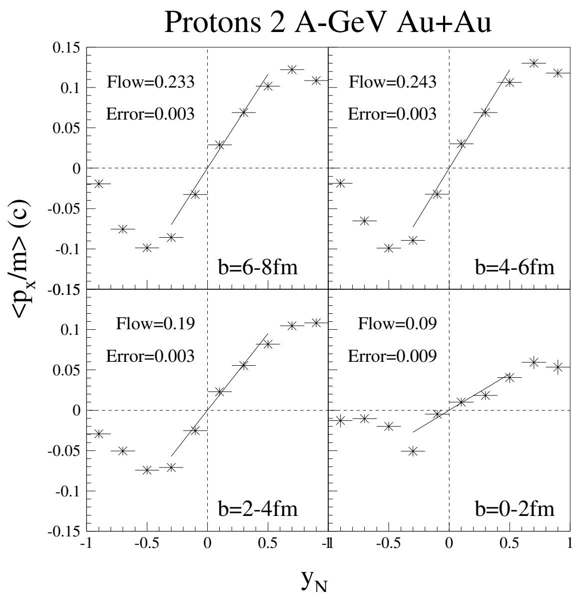

Figure 6.1: Extracted flow for protons at $2\,A-GeV$ (as defined by the slope of $\langle p_x\rangle/m$ versus normalized rapidity at mid-rapidity). The panels are for increasing centrality. It should be noted that the error bars (smaller than the *'s) are statistical in nature and are only modified by the systematics of the reaction plane resolution correction factor.

parameters the signal increases. We were unable to continue the measurement beyond the 8 fm cut due to the trigger bias imposed.

In addition to the trigger biases there were several other limitations on the pions. As was noted in Section 3.4 we have overlapping bands of particle identification. For the π^+ this means that the most forward pions are cut by the overlapping Proton band. Unfortunately, the cut from the proton band is in the rigidity or $|P|$ (total momentum) space and this bias in the $\langle P_{x'}\rangle$ rapidity space of the S-curve is a curve due to the kinamatic relations relating the the two spaces. Therefore, the π^+ distributions in the forward direction have a high $P_\perp$ cut that is a function of the rapidity. Fortunately,

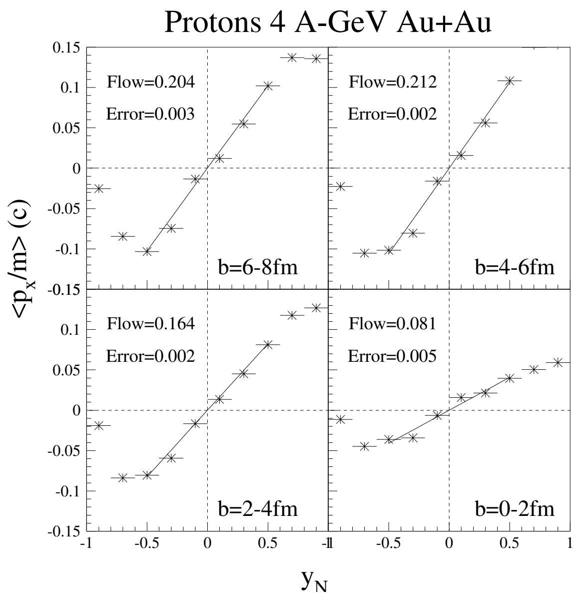

Figure 6.2: Extracted flow for protons at $4\,A\!-\!GeV$ (as defined by the slope of $\langle p_x \rangle/m$ versus normalized rapidity at mid-rapidity). The panels are for increasing centrality.

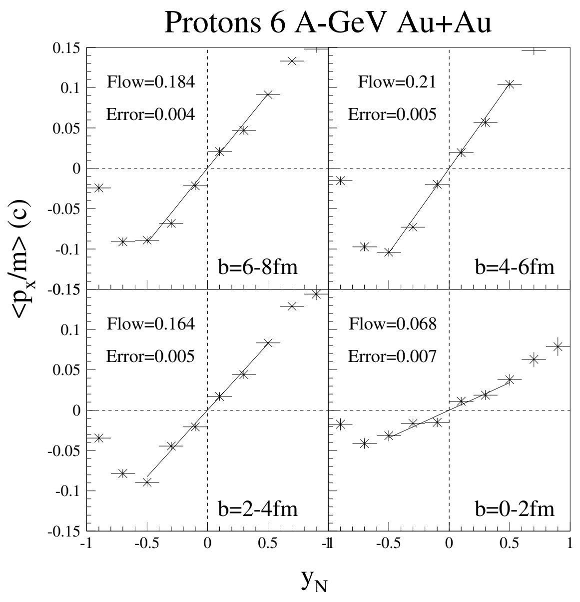

Figure 6.3: Extracted flow for protons at $6\,A\!-\!GeV$ (as defined by the slope of $\langle p_x \rangle/m$ versus normalized rapidity at mid-rapidity). The panels are for increasing centrality.

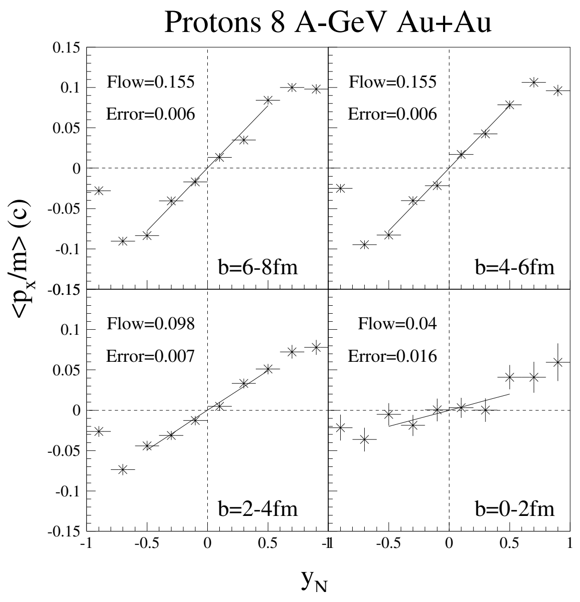

Figure 6.4: Extracted flow for protons at $8A-GeV$ (as defined by the slope of $\langle p_x \rangle /m$ versus normalized rapidity at mid-rapidity). The panels are for increasing centrality.

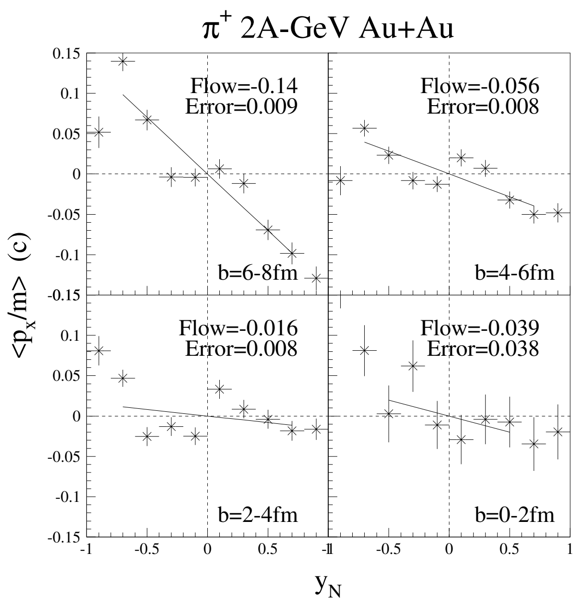

Figure 6.5: Extracted flow for π^+ at $2\,A-GeV$ (as defined by the slope of $\langle p_x \rangle /m$ versus normalized rapidity at mid-rapidity). The panels are for increasing centrality.

0.15
0.1
0.05
0
-0.05
-0.1
-0.15
0.1
0.05
0
-0.05
-0.1
-0.15

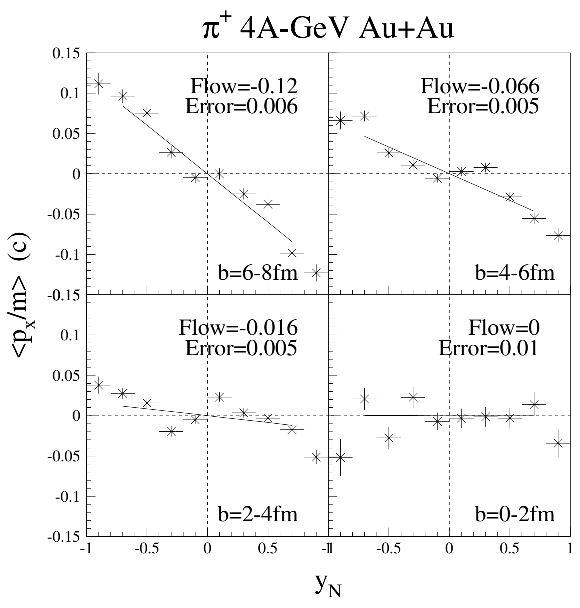

Figure 6.6: Extracted flow for π^+ at 4 $A - GeV$ (as defined by the slope of $\langle p_x \rangle / m$ versus normalized rapidity at mid-rapidity). The panels are for increasing centrality.

0.15
0.1
0.05
0
-0.05
-0.1
-0.15
0.1
0.05
0
-0.05
-0.1
-0.15

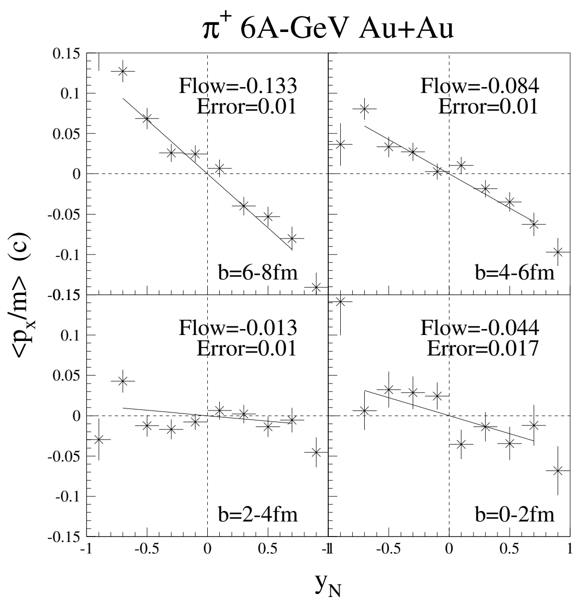

Figure 6.7: Extracted flow for π^+ at 6 $A - GeV$ (as defined by the slope of $\langle p_x \rangle / m$ versus normalized rapidity at mid-rapidity). The panels are for increasing centrality.

-1 -0.5 0 0.5 -1 -0.5 0 0.5 1

-1 -0.5 0 0.5 -1 -0.5 0 0.5 1

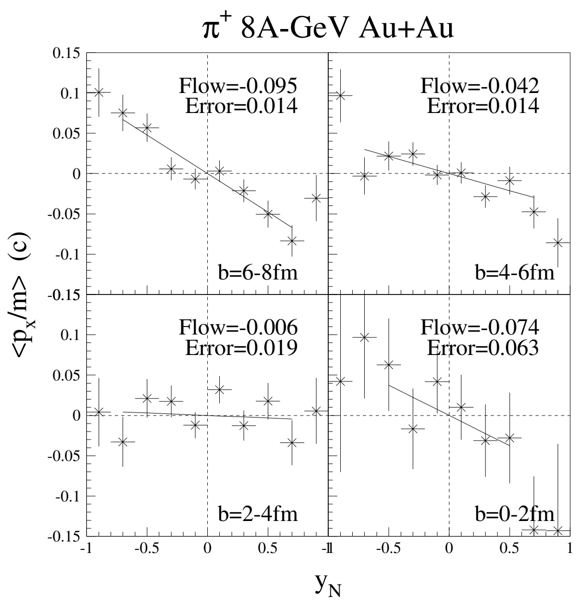

Figure 6.8: Extracted flow for π^+ at 8 $A-GeV$ (as defined by the slope of $\langle p_x \rangle/m$ versus normalized rapidity at mid-rapidity). The panels are for increasing centrality.

the cut has been found to have no effect on the S-curve in the mid—rapidity region where the flow measurement is made.

6.2.3 π^-

The π^- S-curves are shown in Figures 6.9, 6.10, 6.11 and 6.12. We see that the π^- signal still demonstrates the anti-flow signal, though diminished from the π^+, and in turn the proton signal. We do still see that the pions are still showing the maximum signal in the most peripheral centrality bins. We see that at the most central bins the signal becomes not inconsistent with zero, but may indicate a change in sign to positive flow. It should be noted that the π^-'s do not suffer from the hard

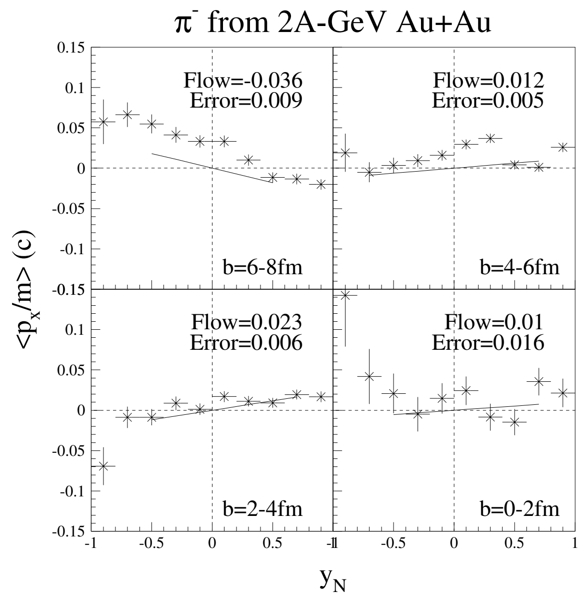

Figure 6.9: Extracted flow for π^- at 2 $A-GeV$ (as defined by the slope of $\langle p_x\rangle/m$ versus normalized rapidity at mid-rapidity). The panels are for increasing centrality.

cut imposed by the proton identification band. The π^-'s would be competing with anti-protons who are at or below their production threshold and therefore, provide very little production cross section. These trends will also be summarized in a later section.

6.2.4 Flow Excitations

Here we can look at the trends of the signal with respect to beam energy and as a function of centrality. As was discussed in the introduction this is the real power of the E895 experiment. It allows us to study all of the variables over a range of initial conditions with the same equipment. We can then compare the results to

0.15
0.1
0.05
0
-0.05
-0.1
-0.15
0.1
0.05
0
-0.05
-0.1
-0.15

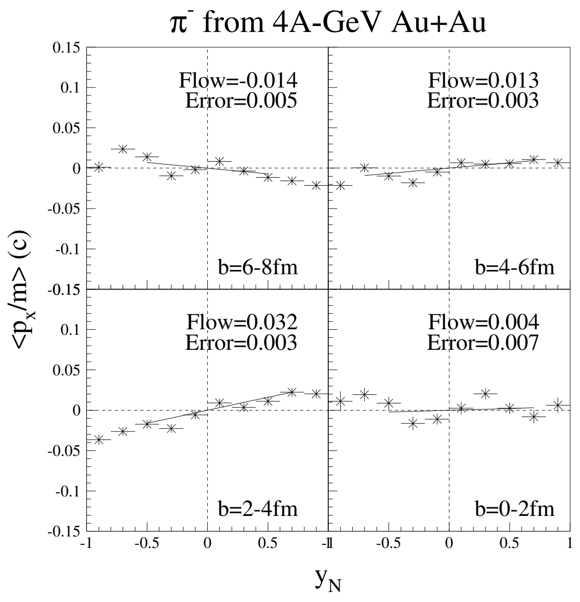

Figure 6.10: Extracted flow for π^- at 4 $A - GeV$ (as defined by the slope of $\langle p_x \rangle / m$ versus normalized rapidity at mid-rapidity). The panels are for increasing centrality.

0.15
0.1
0.05
0
-0.05
-0.1
-0.15
0.1
0.05
0
-0.05
-0.1
-0.15

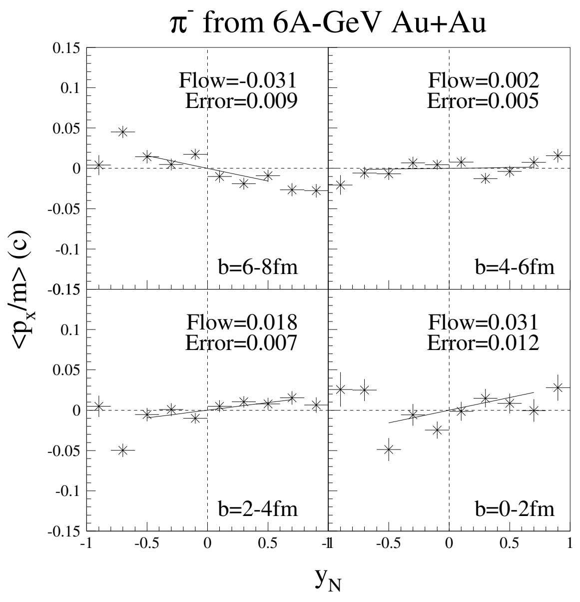

Figure 6.11: Extracted flow for π^+ at 6 $A - GeV$ (as defined by the slope of $\langle p_x \rangle / m$ versus normalized rapidity at mid-rapidity). The panels are for increasing centrality.

-1 -0.5 0 0.5 -1 -0.5 0 0.5 1

-1 -0.5 0 0.5 -1 -0.5 0 0.5 1

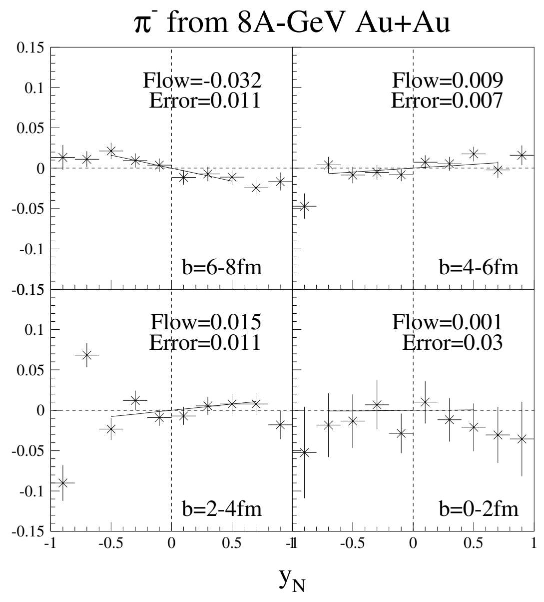

Figure 6.12: Extracted flow for π^- at $8\,A-GeV$ (as defined by the slope of $\langle p_x \rangle/m$ versus normalized rapidity at mid-rapidity). The panels are for increasing centrality.

other experiments at the periphery, as well as theoretical predictions. Table 6.1 is a compilation of the entire data set as measured by the $\langle P_{x'} \rangle/m$ observable. Figure 6.13 shows the beam energy excitation function compiled with other experiments for comparison. The flow signal extracted for the data points displayed here is from the selected centrality bins that gave the maximum signal. For the protons this is the mid-central bin of $4-6\,fm$ as shown in the Figures 6.1, 6.2, 6.3 and 6.4. For the pions it is the most peripheral bins from Figures 6.5, 6.6, 6.7 and 6.8 and Figures 6.9, 6.10, 6.11 and 6.12 for the π^+,π^- respectively. Effort was made to compare to maximal selections for the other experiments as well [Part97], [Kint97] [Pink96] and [Barr96,Barr97]. First we see that, in the protons, the trends seen by the EOS and FOPI groups of a leveling off of the flow signal at about 1 $A-GeV$ is not the case as in [Chan98]. This trend was seen in scaled Ni+Cu or Ni+Ni data from these experiments. In Fig. 6.13 we have the complete excitation function for Au+Au only. We see that the flow increases beyond the .200 c at 1 $A-GeV$ and appears to saturate at a value of 0.240 c at 1.85 $A-GeV$. It then begins to fall smoothly through the 8 $A-GeV$ and matches well with the point at 10.8 $A-GeV$ from E877.

The pions can be seen showing both a species (π^+ versus π^-) dependence as well as differences from the protons. The π^+'s start at a maximum value of 0.220 c at 1.0 $A-GeV$ (the lowest measured energy). They then fall smoothly to about 0.150 c at 1.85 $A-GeV$ and then appear to level off significantly from 1.85 to 10.8 $A-GeV$ with only a slight slope downward. π^-'s, on the other hand, start at relatively low value of about .055 c and continue at a low value for nearly all of the energy range covered, with only a slight increase at the 8 to 10.8 $A-GeV$ region. The pions do not demonstrate any striking features at the 1.85 $A-GeV$ peaking point of the protons.

We now address the issue of centrality dependent signals. Figure 6.14 shows the trends of the $\langle P_{x'} \rangle / m$ versus the centrality selections made. Once again we have protons, π^+s and π^-s displayed. The protons as mentioned before show a peaking in their value in the $4-6\ fm$ area. The pions however show that they continue to increase in flow with more peripheral events. The π^+s seem to indicate that their signal starts at the maximum at the most peripheral (measured here) selection and trends linearly to small or zero anti-flow at the most central collisions. Note that

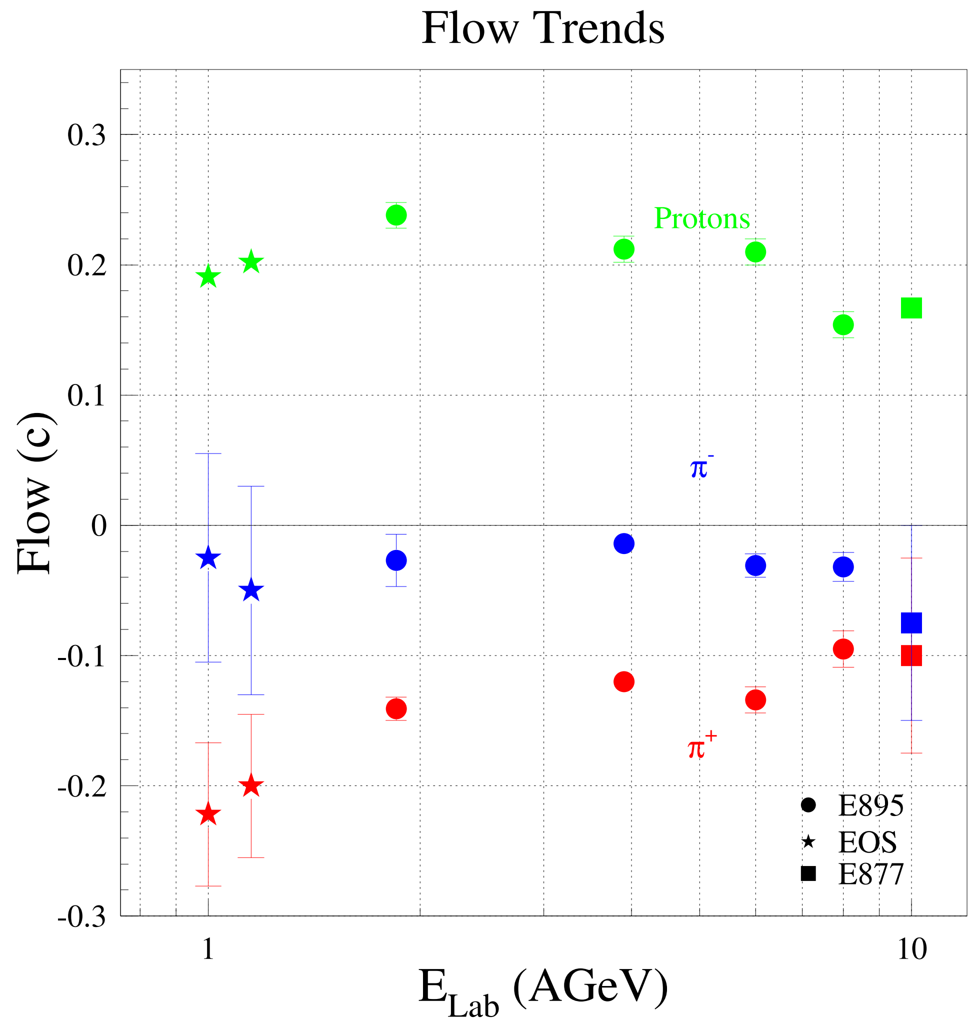

Figure 6.13: Extracted flow for Protons, π^+ and π^- as a function of incident beam energy. The data are taken from the centrality of maximum flow signal for $\langle p_x \rangle/m$ versus normalized rapidity ($4-6\ fm$ for protons, $6-8\ fm$ for pions).

Energy	Impact	$\langle P_x \rangle / m$		
		Protons	π^+	π^-
2	0-2	$.090 \pm .009$	$-.039 \pm .038$	$.001 \pm .016$
	2-4	$.190 \pm .003$	$-.016 \pm .008$	$-.023 \pm .006$
	4-6	$.243 \pm .003$	$-.056 \pm .008$	$.012 \pm .005$
	6-8	$.233 \pm .003$	$-.140 \pm .009$	$-.036 \pm .009$
4	0-2	$.081 \pm .005$	$.00 \pm .010$	$.004 \pm .007$
	2-4	$.164 \pm .002$	$-.016 \pm .005$	$.032 \pm .003$
	4-6	$.212 \pm .002$	$-.066 \pm .005$	$.013 \pm .003$
	6-8	$.204 \pm .003$	$-.120 \pm .006$	$-.014 \pm .005$
6	0-2	$.068 \pm .007$	$-.044 \pm .017$	$.031 \pm .012$
	2-4	$.164 \pm .005$	$.013 \pm .010$	$.018 \pm .007$
	4-6	$.210 \pm .005$	$-.084 \pm .010$	$.002 \pm .005$
	6-8	$.184 \pm .004$	$-.133 \pm .010$	$-.031 \pm .009$
8	0-2	$.040 \pm .016$	$-.074 \pm .063$	$-.001 \pm .030$
	2-4	$.098 \pm .007$	$-.006 \pm .019$	$.015 \pm .011$
	4-6	$.155 \pm .006$	$-.042 \pm .014$	$.009 \pm .007$
	6-8	$.155 \pm .006$	$-.095 \pm .014$	$-.032 \pm .011$

Table 6.1: Compilation of the flow ($\langle P_x \rangle / m$) signal for protons, π^+ and π^-. The reader is referred to Table 3.3 for a listing of the reaction plane resolution correction factors applied to the data listed above.

the protons still have significant flow for the most central collisions. The π^-s on the other hand appear to start at a maximum anti-flow signal at the most peripheral and tend to zero at mid-central collisions. There is even some small evidence of a sign change in the π^- flow for the most central collisions. However, this determination is difficult due to the poor resolution of the determination of the reaction plane at this centrality.

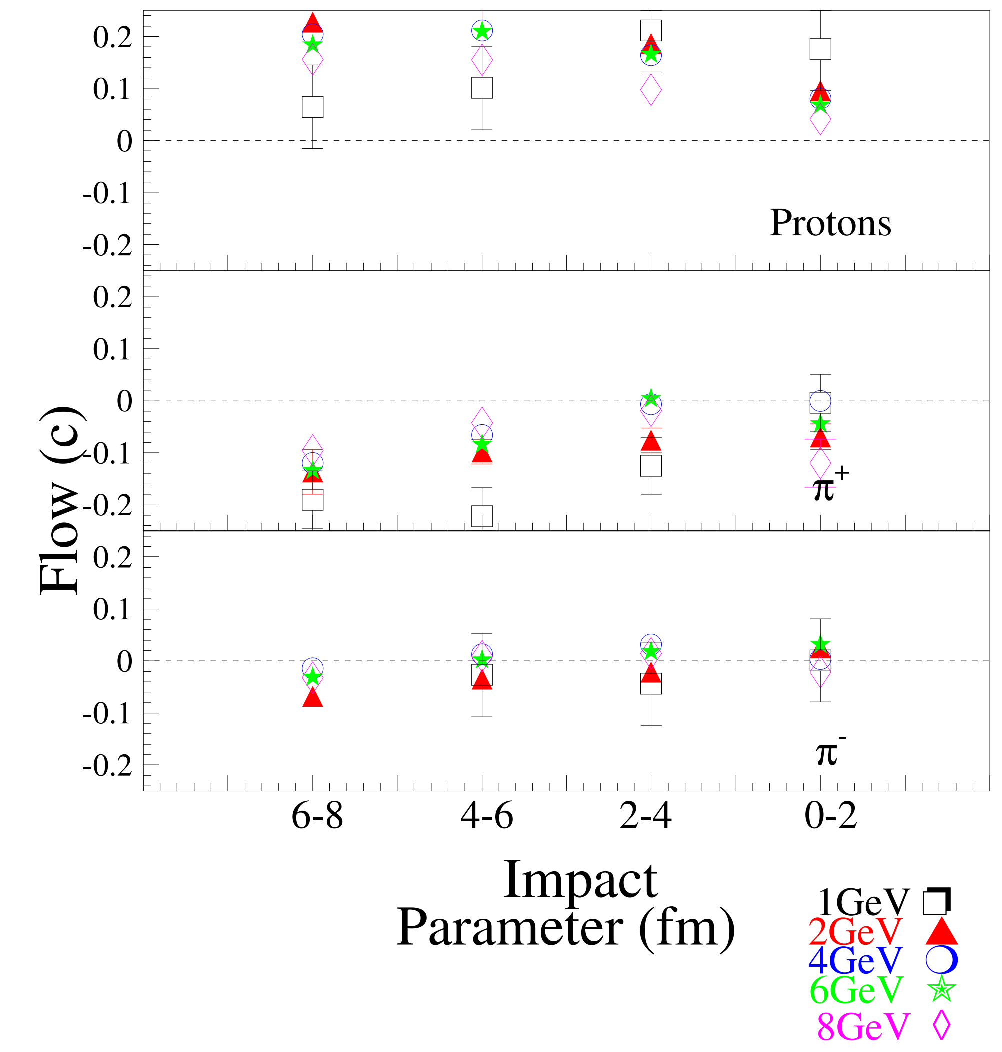

Figure 6.14: Extracted flow for Protons, π^+ and π^- as a function of centrality. The data are taken from the slope of $\langle p_x \rangle / m$ versus normalized rapidity for each of the incident beam energies.

Energy	Impact	Protons				
		$\langle P_x \rangle / m$			V2	
		Liu	Pinkenberg	Caskey	Pinkenberg	Caskey
2	4-6	$.265 \pm .025$	$.308 \pm .001$	$.243 \pm .002$	$-.051 \pm .005$	$-.041 \pm .004$
4	4-6	$.225 \pm .025$	$.277 \pm .001$	$.212 \pm .002$	$-.002 \pm .005$	$-.007 \pm .004$
6	4-6	$.170 \pm .025$	$.229 \pm .001$	$.210 \pm .004$	$.0115 \pm .005$	$.031 \pm .011$
8	4-6	none	$.218 \pm .001$	$.155 \pm .005$	$.0136 \pm .005$	$.044 \pm .021$

Table 6.2: Compilation of the flow ($\langle P_x \rangle / m$) and V2 signals for protons by Chris Pinkenberg and Heng Liu of the E895 collaboration [Liu97,Pink99]. The "Caskey" columns represents the results from this dissertation.

6.3 Fourier Flow

To remind the reader this signal is derived from the fitting of the dN/dΦ spectrum of particles with fourier components see Section 5.3. It differs from the above discussion in that the signal is not weighted by the individual $P_{\perp}$ contributions of the particles. It demonstrates the collective population distributions of the the particles. It can be however related to the Flow signals above through proper $P_{\perp}$ weighting and integration of the signal with respect to $P_{\perp}$. I will once again show protons as well as pions for comparison. Table 6.3 tabulates all of the data for each of the incident energies and centrality selections.

6.3.1 Protons V1 component

Figures 6.15, 6.16, 6.17 and 6.18 are the compilation of the V1 signal. We have attempted to keep the same structure for the plots as was used previously. That is, the x-axis is the same normalized rapidity but the y-axis is now the percent or population anisotropy. We see also the same centrality selections as before in the four panels of each incident beam energy. We note again that the error bars displayed in the graphic are mostly statistical in nature only. The only systematic consideration made, is for the reaction plane resolution correction factor that is applied.

First, we note that the V1 signal has the same "sign" as the proton flow. Indicating the the population of protons is concentrated on the projectile side in the forward direction the same as the flow signal was. We see that it also is dependent on the rapidity just as the flow signal was and is very linear at mid-rapidity. I have therefore chosen to quantize the signal by fitting a line through mid-rapidity and taking the slope as the "V1" signal that will be used in later comparisons. Doing this we see that it peaks in the mid-central $4-6\,fm$ bin just as the proton flow signal did before.

6.3.2 π^+ V1 component

Once again we have the complete set of incident beam energy plots displayed in Figures 6.19, 6.20, 6.21 and 6.22 for discussion. In these plots we again see that the signal roughly follows that of the previously discussed flow signal. It also remains fairly linear and therefore, has been quantized by a linear fit through mid-rapidity. In looking at the trends of the four panels we see that the signal again is maximal in the most peripheral and trends down to zero as we go to the most central collisions. We also see that the signal is still diminished from that of the protons, by more than a factor of 2.

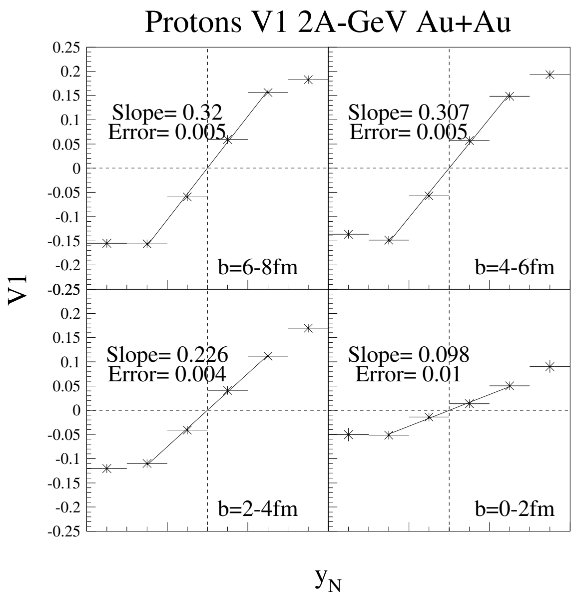

Figure 6.15: Extracted V1 for Protons at 2 $A - GeV$ (as defined by the $cos\phi$ of the dN/dΦ distribution). The panels are for increasing centrality.

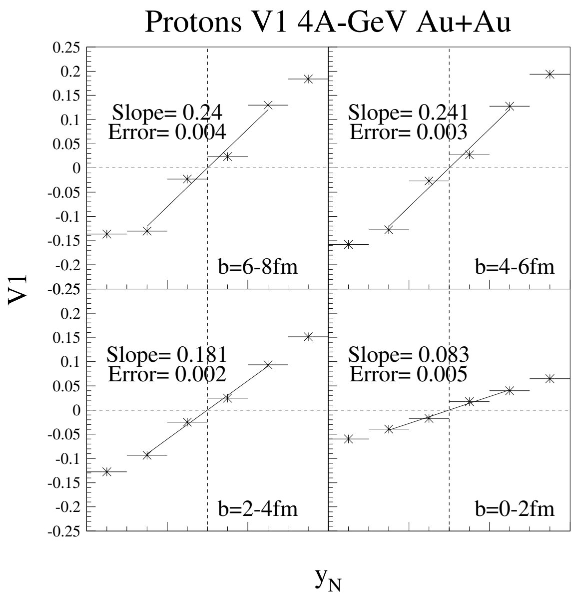

Figure 6.16: Extracted V1 for Protons at 4 $A - GeV$ (as defined by the $cos\phi$ of the dN/dΦ distribution). The panels are for increasing centrality.

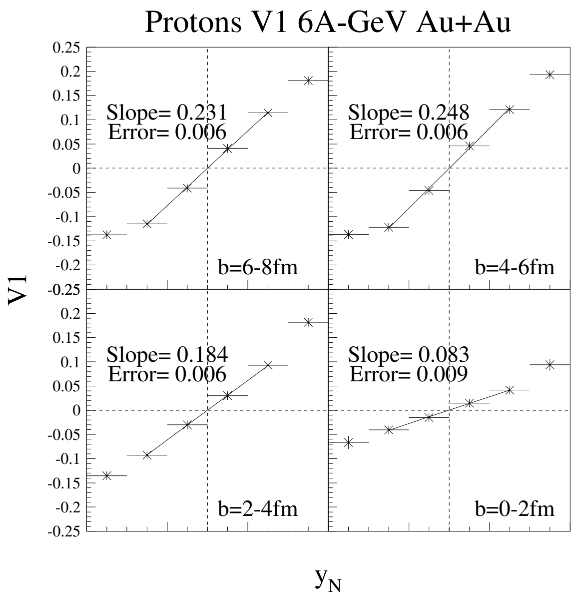

Figure 6.17: Extracted V1 for Protons at 6 $A-GeV$ (as defined by the $cos\phi$ of the dN/dΦ distribution). The panels are for increasing centrality.

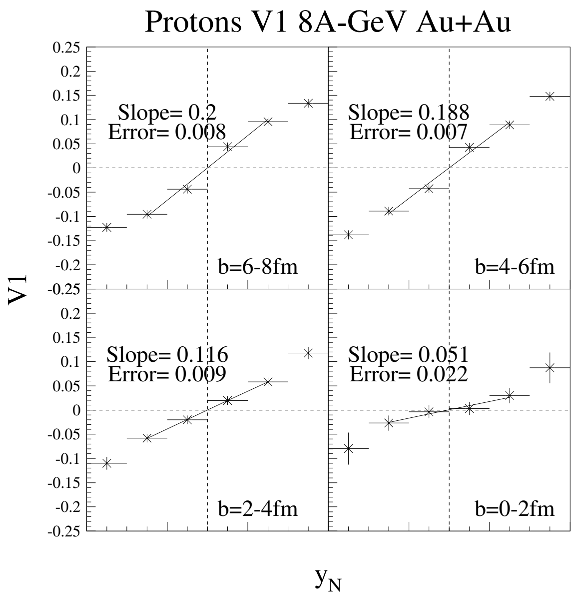

Figure 6.18: Extracted V1 for Protons at 8 $A-GeV$ (as defined by the $cos\phi$ of the dN/dΦ distribution). The panels are for increasing centrality.

0.25
0.2
0.15
0.1
0.05
0
-0.05
-0.1
-0.15
-0.2
-0.25
0.2
0.15
0.1
0.05
0
-0.05
-0.1
-0.15
-0.2
-0.25

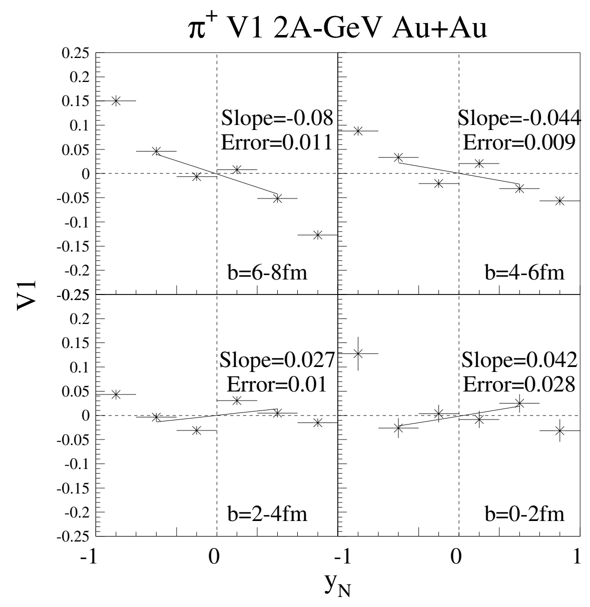

Figure 6.19: Extracted V1 for π^+ at $2\,A-GeV$ (as defined by the $cos\phi$ of the dN/dΦ distribution). The panels are for increasing centrality.

0.25
0.2
0.15
0.1
0.05
0
-0.05
-0.1
-0.15
-0.2
-0.25
0.2
0.15
0.1
0.05
0
-0.05
-0.1
-0.15
-0.2
-0.25

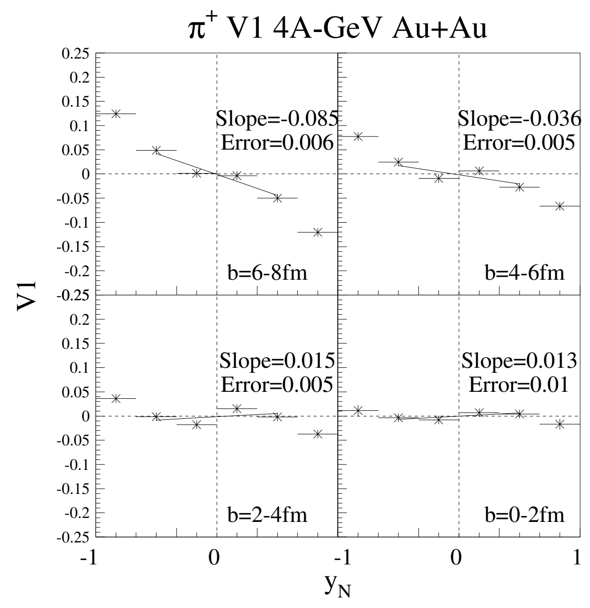

Figure 6.20: Extracted V1 for π^+ at $4\,A-GeV$ (as defined by the $cos\phi$ of the dN/dΦ distribution). The panels are for increasing centrality.

0 2 4 6 2 4 6

0 2 4 6 2 4 6

0 2 4 6 2 4 6

0 2 4 6 2 4 6

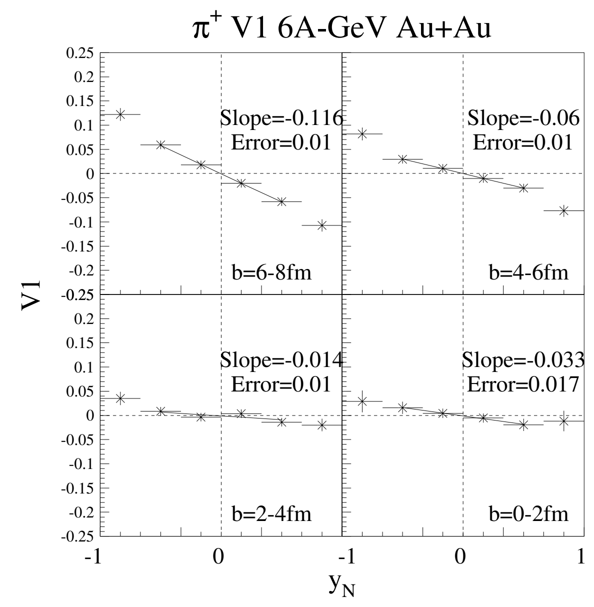

Figure 6.21: Extracted V1 for π^+ at $6\,A-GeV$ (as defined by the $cos\phi$ of the dN/dΦ distribution). The panels are for increasing centrality.

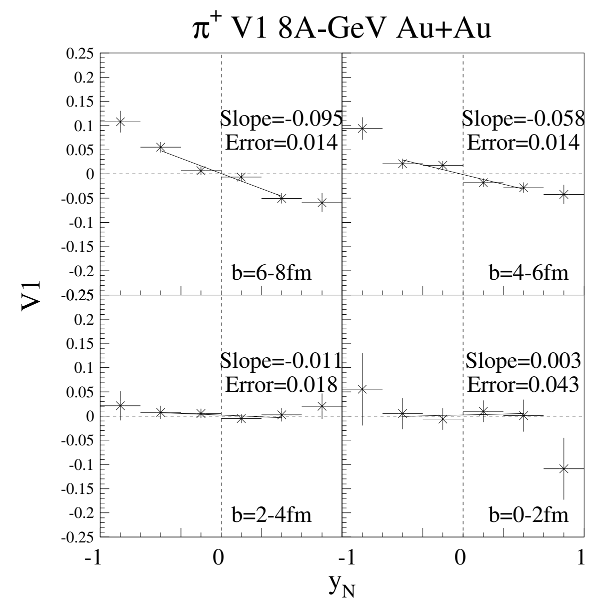

Figure 6.22: Extracted V1 for π^+ at $8\,A-GeV$ (as defined by the $cos\phi$ of the dN/dΦ distribution). The panels are for increasing centrality.

0.25
0.2
0.15
0.1
0.05
0
-0.05
-0.1
-0.15
-0.2
-0.25
0.2
0.15
0.1
0.05
0
-0.05
-0.1
-0.15
-0.2
-0.25

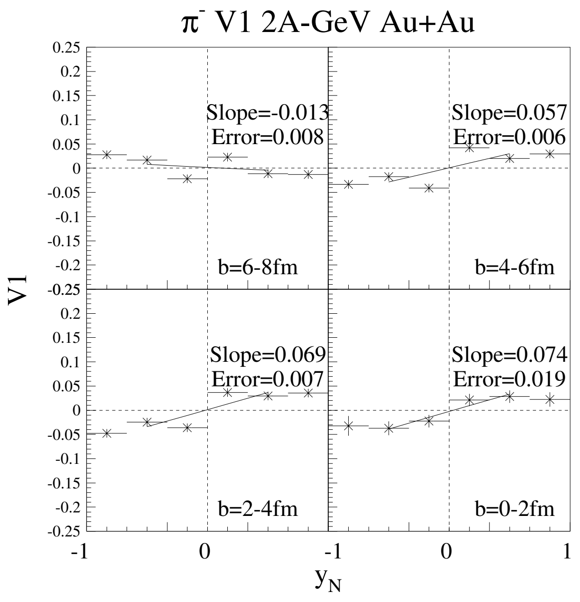

Figure 6.23: Extracted V1 for π^- at $2\,A-GeV$ (as defined by the $cos\phi$ of the dN/dΦ distribution). The panels are for increasing centrality.

6.3.3 π^- V1 component

The π^- Figures 6.23, 6.24, 6.25 and 6.26 are reproduced here for discussion as well. In them we see that the V1 trends are once again similar to that of the flow signal. We see the maximal value appearing towards the most peripheral, roughly zero at mid-central and some indication of a sign change at the most central.

6.3.4 Fourier V1 component Excitations

We can once again compile all of the data above into a set of composite plots. Figure 6.27 shows the signal (slope at mid-rapidity) as a function of the incident beam energy. We see that the protons start at a maximum of about 30% at $1.85\,A-GeV$

0 2 4 6 2 4 6

0 2 4 6 2 4 6

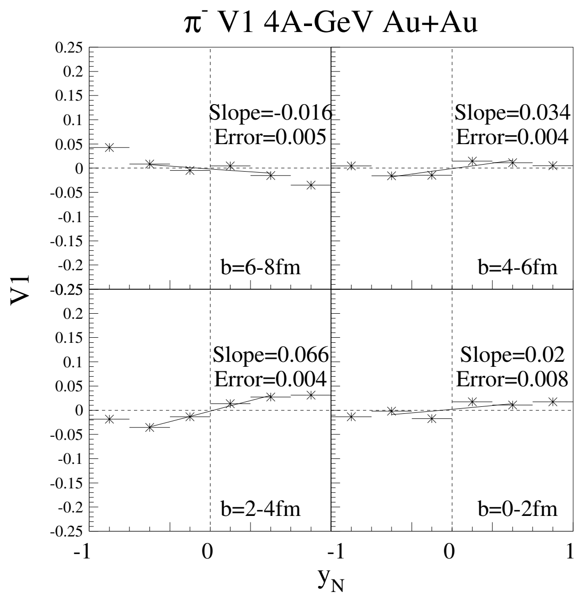

Figure 6.24: Extracted V1 for π^- at $4\,A-GeV$ (as defined by the $cos\phi$ of the dN/dΦ distribution). The panels are for increasing centrality.

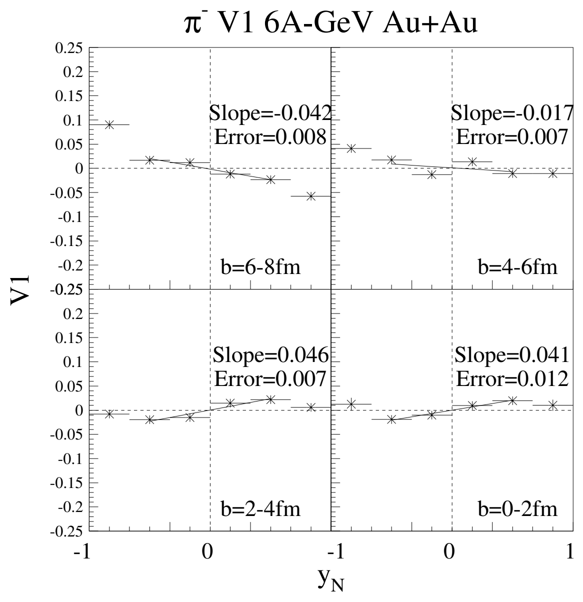

Figure 6.25: Extracted V1 for π^- at $6\,A-GeV$ (as defined by the $cos\phi$ of the dN/dΦ distribution). The panels are for increasing centrality.

0.25
0.2
0.15
0.1
0.05
0
-0.05
-0.1
-0.15
-0.2
-0.25
0.2
0.15
0.1
0.05
0
-0.05
-0.1
-0.15
-0.2
-0.25

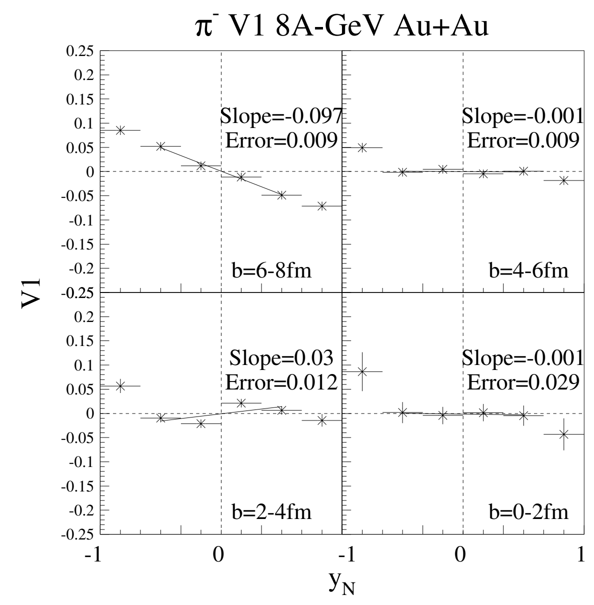

Figure 6.26: Extracted V1 for π^- at $8\,A-GeV$ (as defined by the $cos\phi$ of the dN/dΦ distribution). The panels are for increasing centrality.

and drop smoothly to about 20% at $8\,A-GeV$. The π^+ and π^- start at about 8% and 1% respectively at $1.85\,A-GeV$.

In Fig. 6.28 we see the signals compiled versus centrality. In this plot we see that the trend closely follows the trends established in the $\langle P_{x'}\rangle/m$ flow versus centrality plot displayed in Fig. 6.14. I should note here that the signals presented in these plots are extracted from the data with the same centrality cuts used in the previous excitation functions.

0 2 4 6 6 2 4 6

0 2 4 6 6 2 4 6

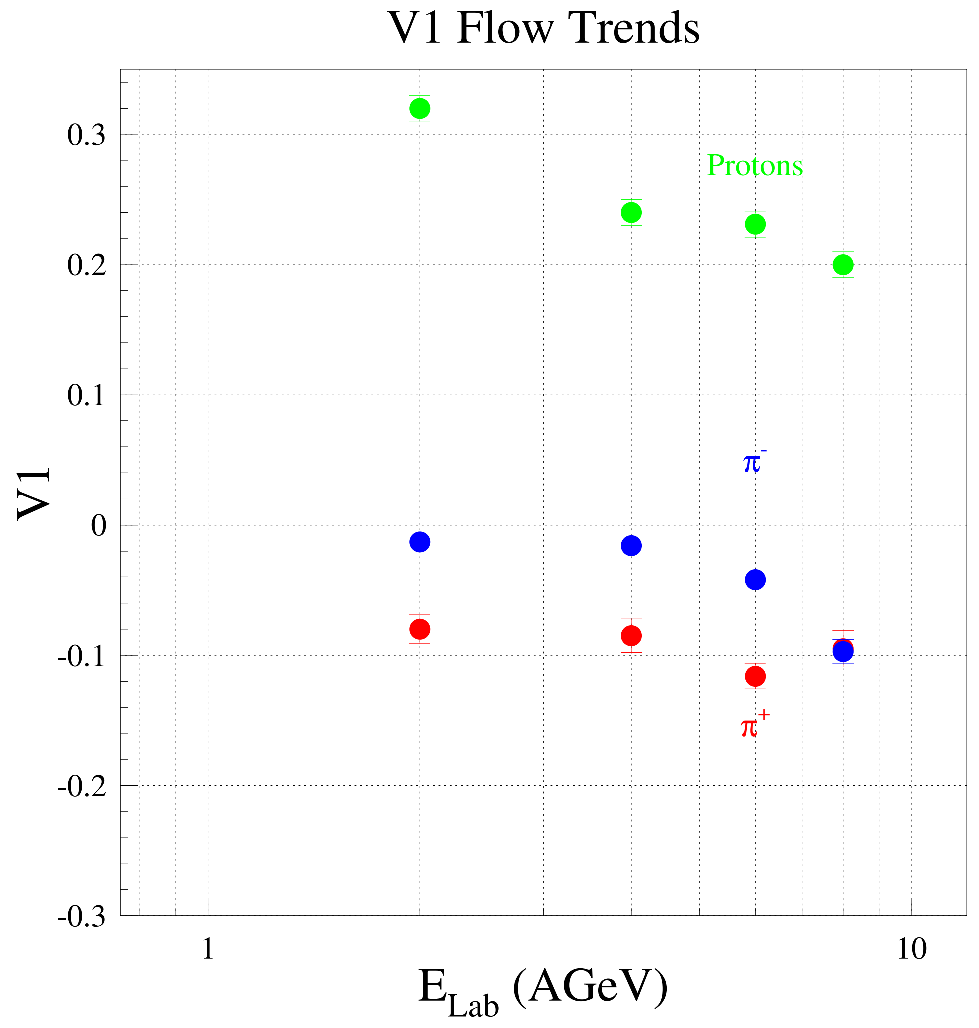

Figure 6.27: Extracted V1 flow for Protons, π^+ and π^- as a function of incident beam energy. The data are taken from the centrality of maximum flow signal for V1 versus normalized rapidity ($4-6\ fm$ for protons, $6-8\ fm$ for pions).

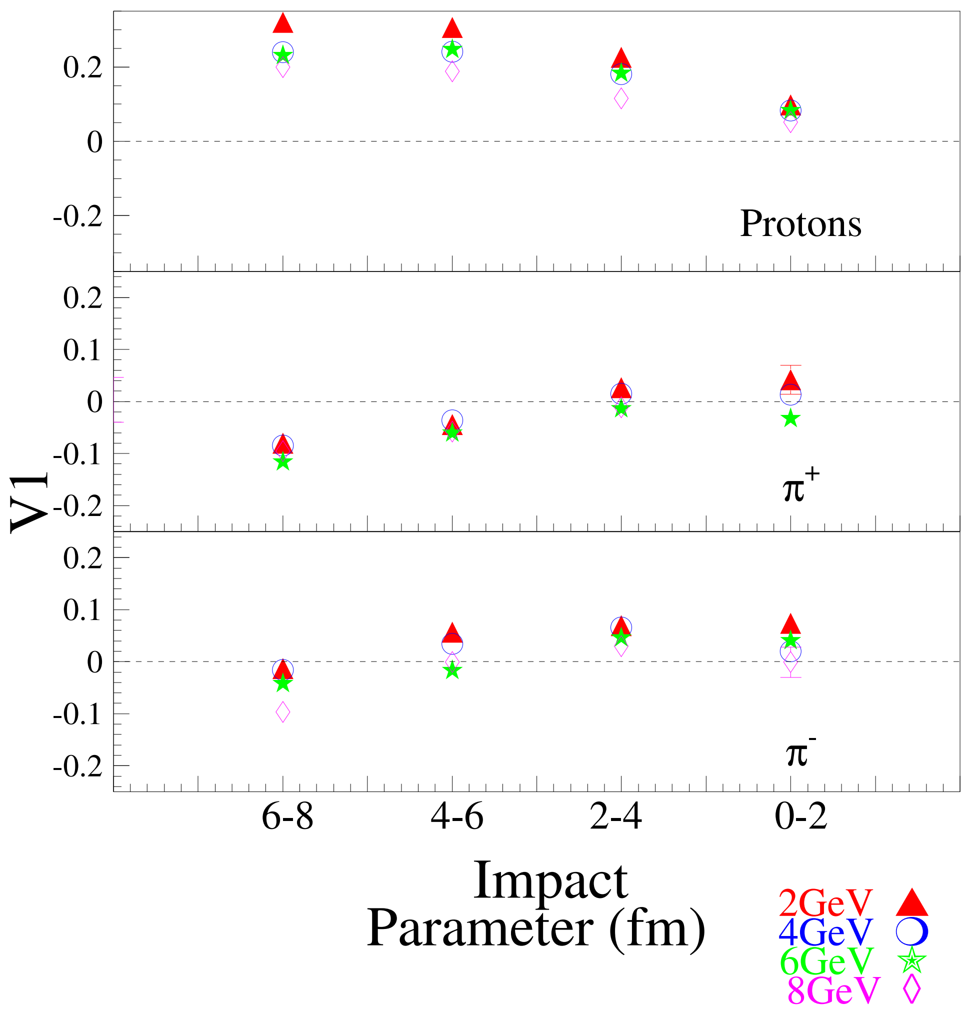

Figure 6.28: Extracted V1 flow for Protons, π^+ and π^- as a function of centrality. The data are taken from the slope of V1 versus normalized rapidity for each of the incident beam energies.

Energy	Impact	Fourier V1		
		Protons	π^+	π^-
2	0-2	$.098 \pm .019$	$.042 \pm .028$	$.074 \pm .019$
	2-4	$.226 \pm .004$	$.027 \pm .010$	$.069 \pm .007$
	4-6	$.307 \pm .005$	$-.044 \pm .009$	$.057 \pm .006$
	6-8	$.320 \pm .005$	$-.080 \pm .011$	$-.013 \pm .008$
4	0-2	$.083 \pm .005$	$.013 \pm .010$	$.020 \pm .008$
	2-4	$.181 \pm .002$	$.015 \pm .005$	$.066 \pm .004$
	4-6	$.241 \pm .003$	$-.036 \pm .005$	$.034 \pm .004$
	6-8	$.240 \pm .004$	$-.085 \pm .006$	$-.016 \pm .005$
6	0-2	$.083 \pm .009$	$-.033 \pm .017$	$.041 \pm .012$
	2-4	$.184 \pm .006$	$-.014 \pm .010$	$.046 \pm .007$
	4-6	$.248 \pm .006$	$-.060 \pm .010$	$-.017 \pm .007$
	6-8	$.231 \pm .006$	$-.116 \pm .010$	$-.042 \pm .008$
8	0-2	$.051 \pm .022$	$.003 \pm .043$	$-.001 \pm .029$
	2-4	$.116 \pm .009$	$-.011 \pm .018$	$.030 \pm .012$
	4-6	$.188 \pm .007$	$-.058 \pm .014$	$-.001 \pm .009$
	6-8	$.200 \pm .008$	$-.095 \pm .014$	$-.097 \pm .009$

Table 6.3: Compilation of the flow (Fourier V1) signal for protons, π^+ and π^-. The reader is referred to Table 3.3 for a listing of the reaction plane resolution correction factors applied to the data listed above.

6.3.5 Proton V1 $P_\perp$ dependence

As has been mentioned one of the powerful bonuses of calculating the flow observable via the Fourier components is that there is no explicit $P_\perp$ dependence. This then allows us to study the dependence of the observable differentiated on this variable. Figures 6.29, 6.30, 6.31 and 6.32 show a sampling of the V1 component versus $P_\perp$. The panels are rapidity selections going from the most backward (forward) at the top (bottom). The binning of the panels is the same as the binning for the S like curves for V1 versus rapidity shown in Figures 6.15, 6.16, 6.17 and 6.18. In studying this signal we note some of its features. The signal goes to zero as $P_\perp$ goes to zero the signal is developed in the higher $P_\perp$ region. At midrapidity the signal is zero for all $P_\perp$ demonstrating that flow has been completely removed in this region.

6.3.6 π^+ V1 $P_\perp$ dependence

Figures 6.33, 6.34, 6.35 and 6.36 show a sampling of the V1 component versus $P_\perp$ for π^+. Note that the x-axis has changed as the phase space of the pions is limited to lower $P_\perp$. Comparing to the protons we see that there are different features here. We see that, for the pions, the signal appears to manifest itself in the low $P_\perp$ region and then tend to zero as we go higher in $P_\perp$. We do still however see that the signal is once again completely removed for all $P_\perp$ at the mid-rapidity region. It should be noted that the particle identification issues discussed earlier are here manifested. We can see that in the most forward bin (lower right corner of Fig. 6.33) the data have

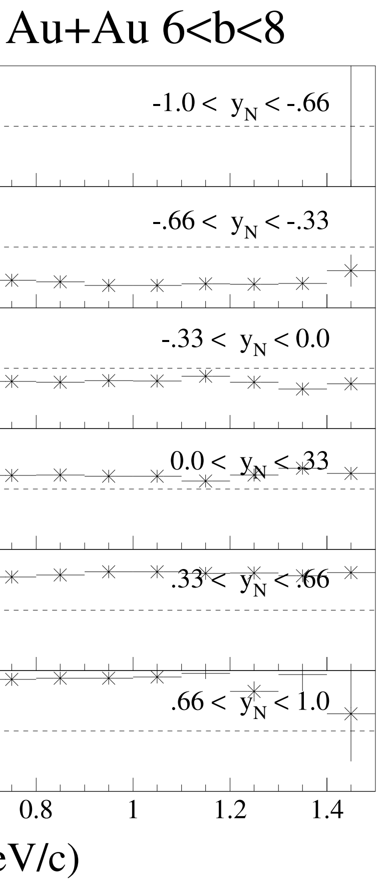

Figure 6.29: Displayed is the V1 flow value versus Transverse Momentum for $2A-GeV$ protons from a centrality selection of $6-8\,fm$. Down the page are the six rapidity bins used for the S like curves shown in Figures 6.15, 6.16, 6.17, 6.18.

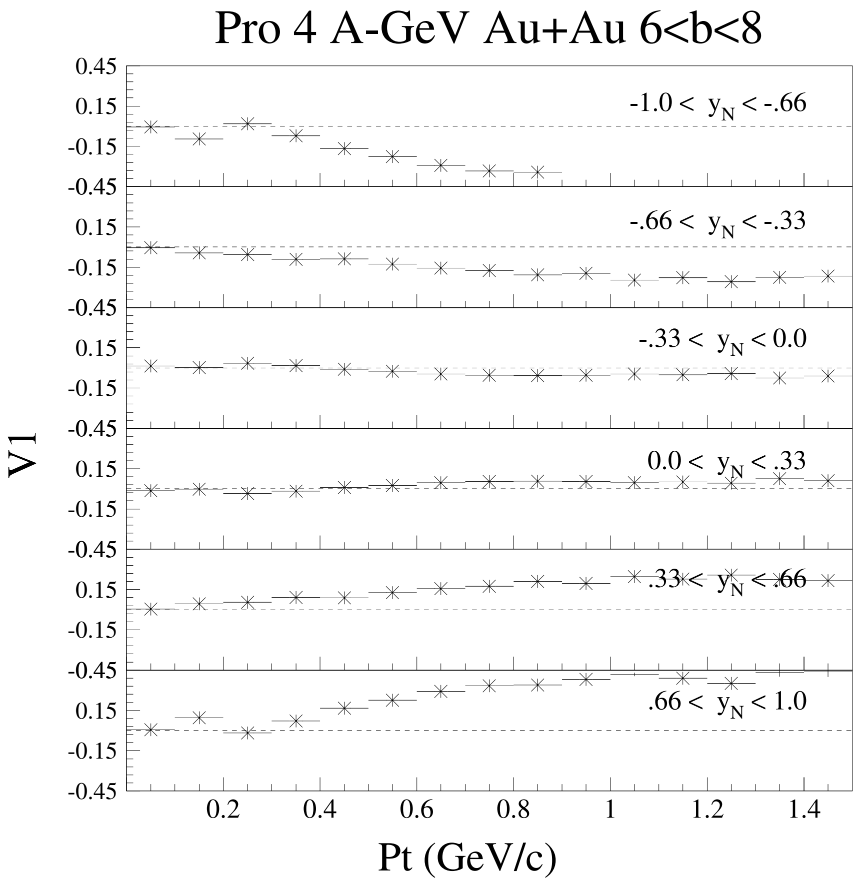

Figure 6.30: Displayed is the V1 flow value versus Transverse Momentum for $4A-GeV$ protons from a centrality selection of $6-8\,fm$. Down the page are the six rapidity bins used for the S like curves shown in Figures 6.15, 6.16, 6.17, 6.18.

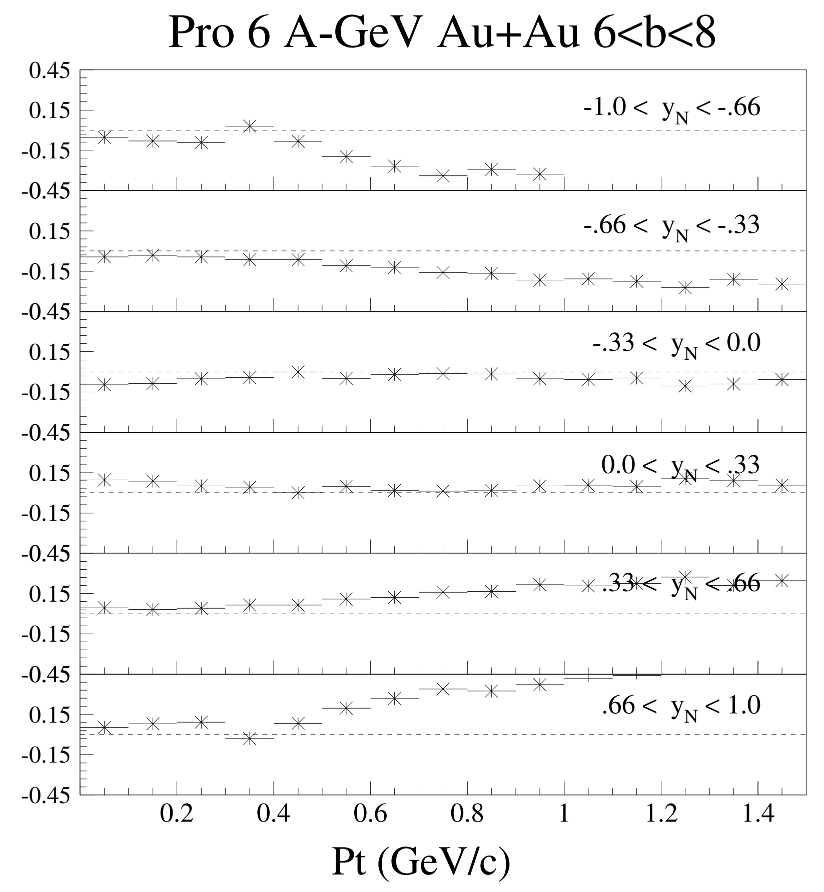

Figure 6.31: Displayed is the V1 flow value versus Transverse Momentum for $6A-GeV$ protons from a centrality selection of $6-8\,fm$. Down the page are the six rapidity bins used for the S like cvrves shown in Figures 6.15, 6.16, 6.17, 6.18.

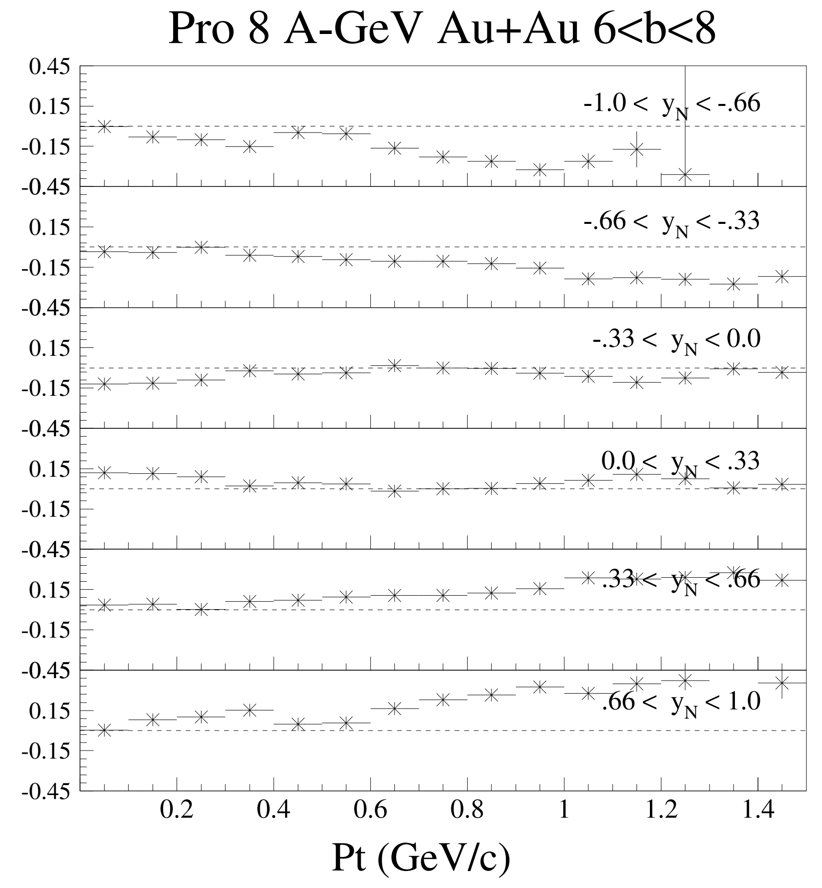

Figure 6.32: Displayed is the V1 flow value versus Transverse Momentum for $8A{-}GeV$ protons from a centrality selection of $6-8\,fm$. Down the page are the six rapidity bins used for the S like curves shown in Figures 6.15, 6.16, 6.17, 6.18.

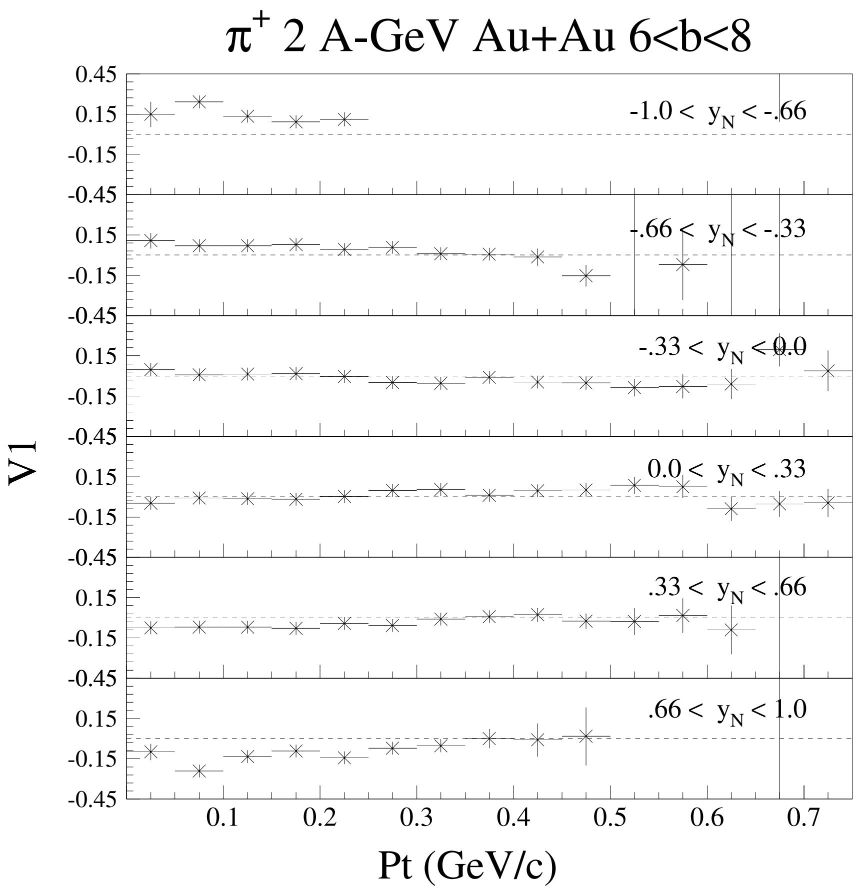

Figure 6.33: Displayed is the V1 flow value versus Transverse Momentum for $2A{-}GeV$ π^+ from a centrality selection of $6 - 8\ fm$. Down the page are the six rapidity bins used for the S like curves shown in Figures 6.19, 6.20, 6.21, 6.22.

a high $P_\perp$ cut from the proton identification band. In the backward direction we see a similar cut from the geometry of the detector.

6.3.7 π^- V1 $P_\perp$ dependence

Figures 6.37, 6.38, 6.39 and 6.40 are a set of graphs showing the trends of the π^-s. We note here that the π^-s demonstrate still different behavior. Their signal

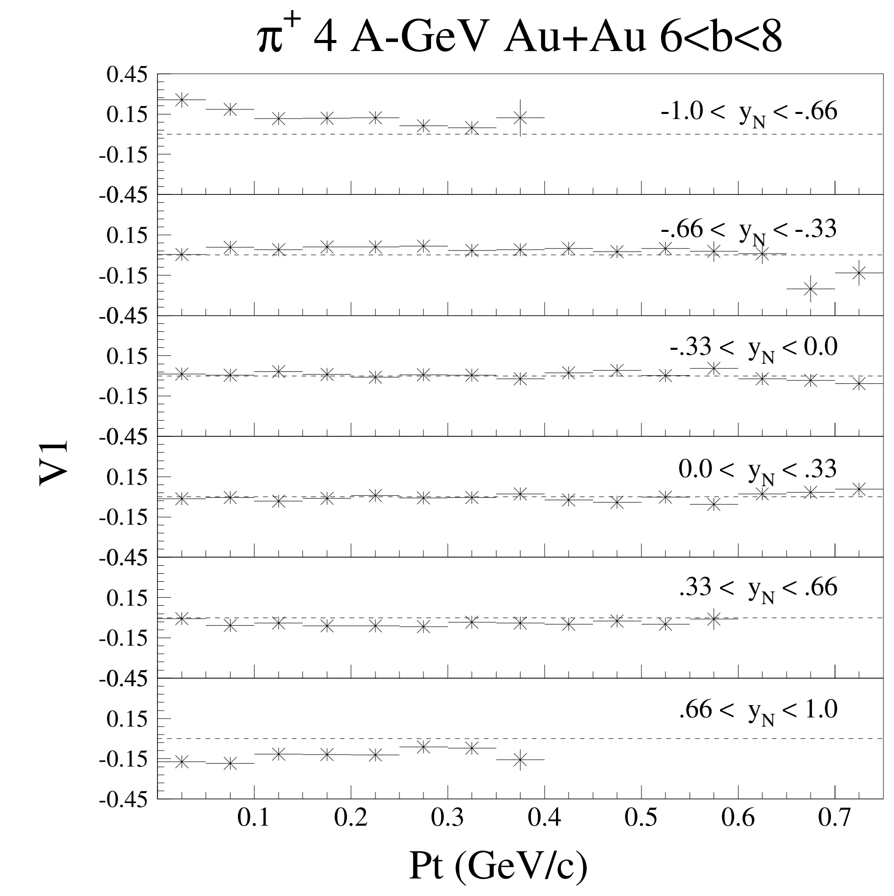

Figure 6.34: Displayed is the V1 flow value versus Transverse Momentum for $4A\!-\!GeV$ π^+ from a centrality selection of $6-8\ fm$. Down the page are the six rapidity bins used for the S like curves shown in Figures 6.19, 6.20, 6.21, 6.22.

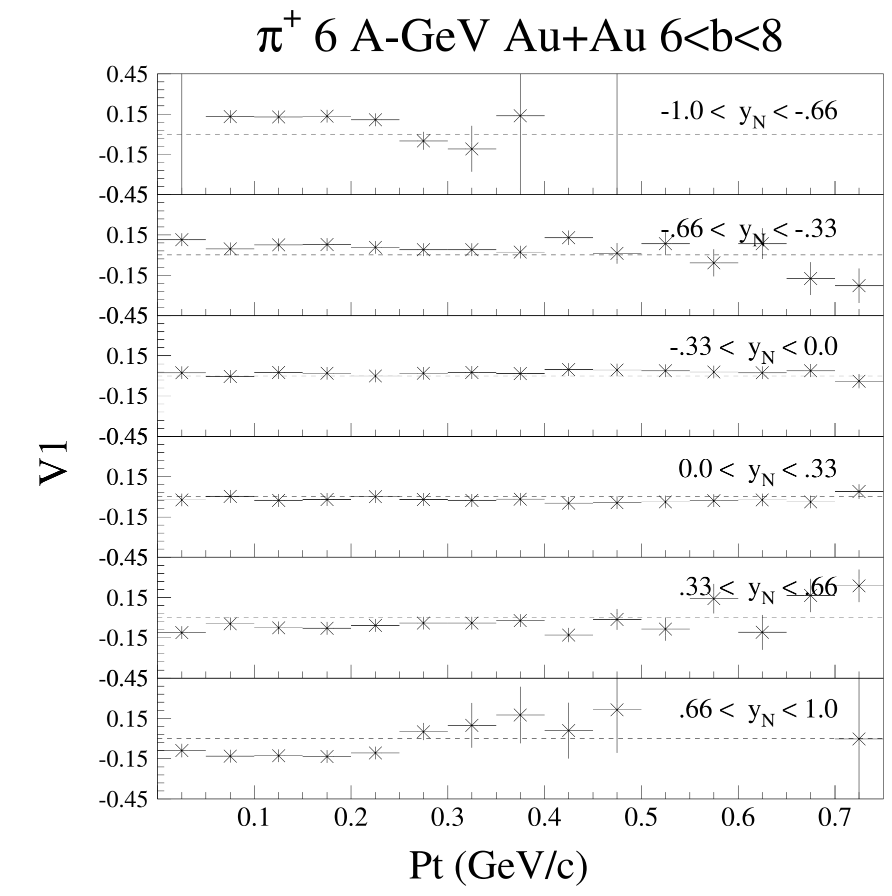

Figure 6.35: Displayed is the V1 flow value versus Transverse Momentum for $6A-GeV$ π^+ from a centrality selection of $6-8\ fm$. Down the page are the six rapidity bins used for the S like curves shown in Figures 6.19, 6.20, 6.21, 6.22.

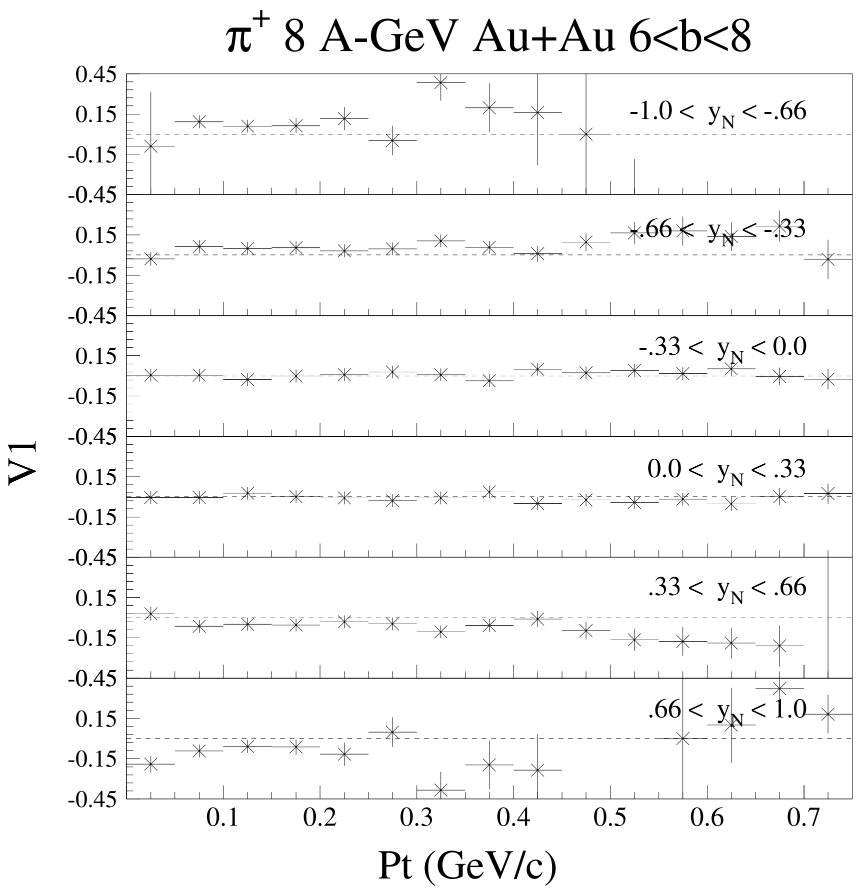

Figure 6.36: Displayed is the V1 flow value versus Transverse Momentum for $8A-GeV$ π^+ from a centrality selection of $6-8\ fm$. Down the page are the six rapidity bins used for the S like curves shown in Figures 6.19, 6.20, 6.21, 6.22.

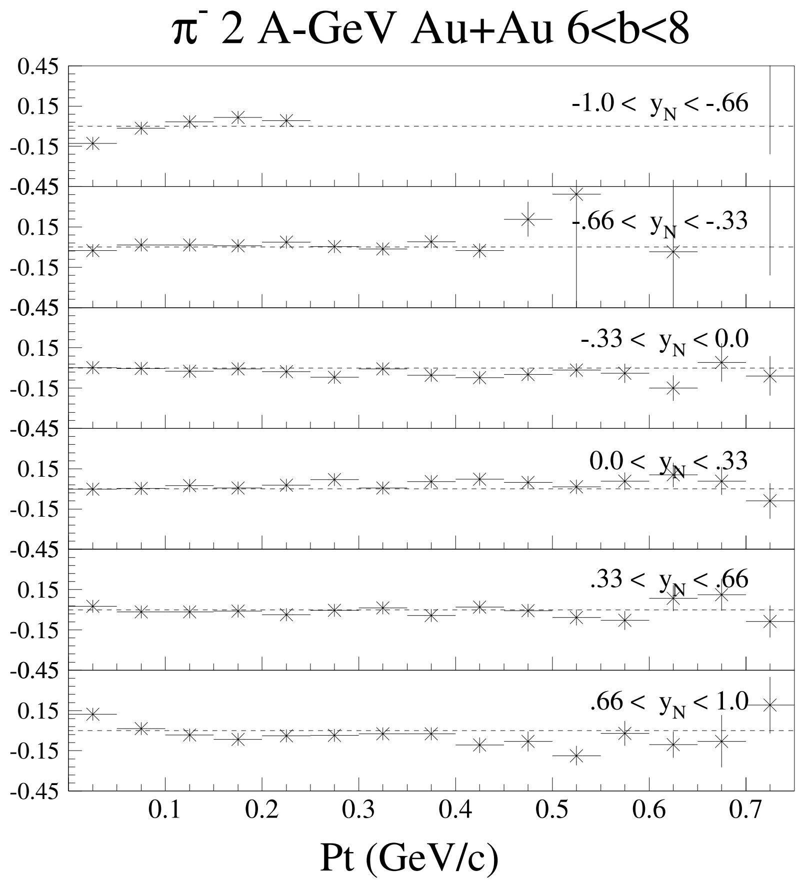

Figure 6.37: Displayed is the V1 flow value versus Transverse Momentum for $2A{-}GeV$ π^- from a centrality selection of $6-8\ fm$. Down the page are the six rapidity bins used for the S like curves shown in Figures 6.23, 6.24, 6.25, 6.26.

appears to be developing in the high $P_\perp$ region unlike the π^- signal. It looks more like the proton signal, with however a sign change denoting the anti-flow behavior. We do still see that the signal is removed in the mid-rapidity region as required.

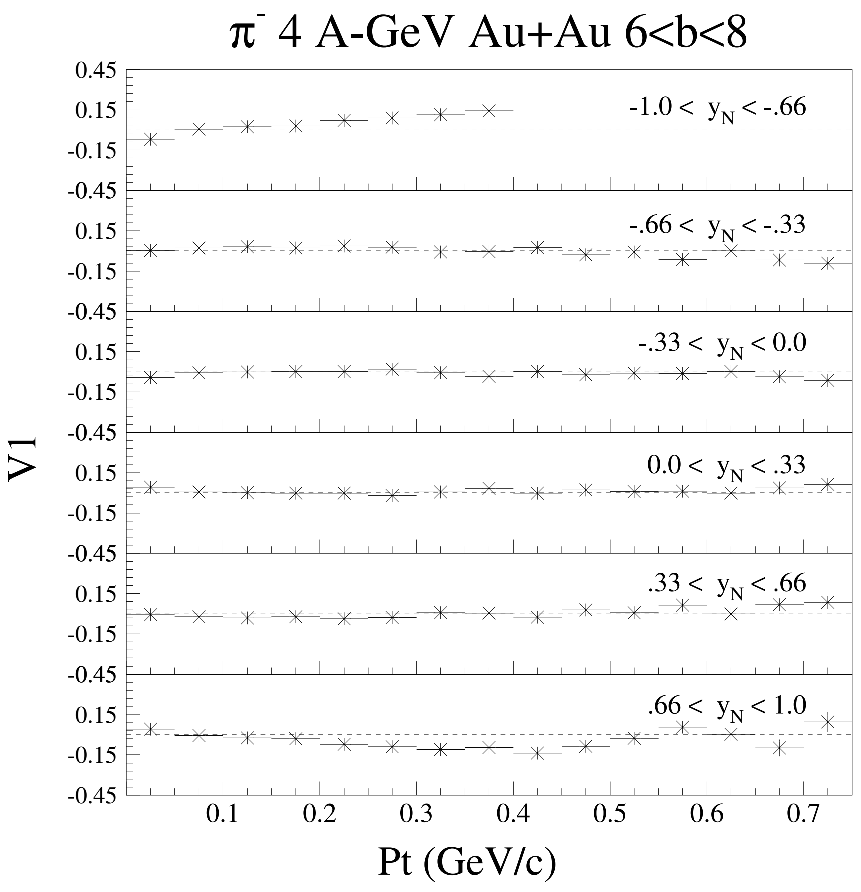

Figure 6.38: Displayed is the V1 flow value versus Transverse Momentum for $4A\!-\!GeV$ π^- from a centrality selection of $6-8\ fm$. Down the page are the six rapidity bins used for the S like curves shown in Figures 6.23, 6.24, 6.25, 6.26.

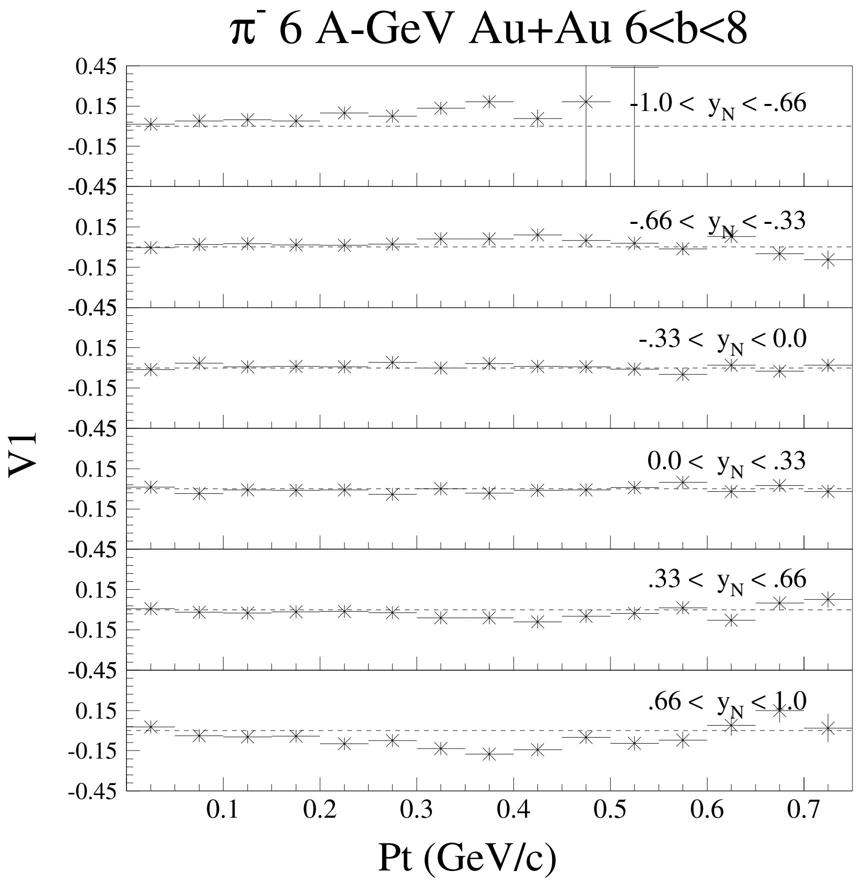

Figure 6.39: Displayed is the V1 flow value versus Transverse Momentum for $6A-GeV$ π^- from a centrality selection of $6-8\ fm$. Down the page are the six rapidity bins used for the S like curves shown in Figures 6.23, 6.24, 6.25, 6.26.

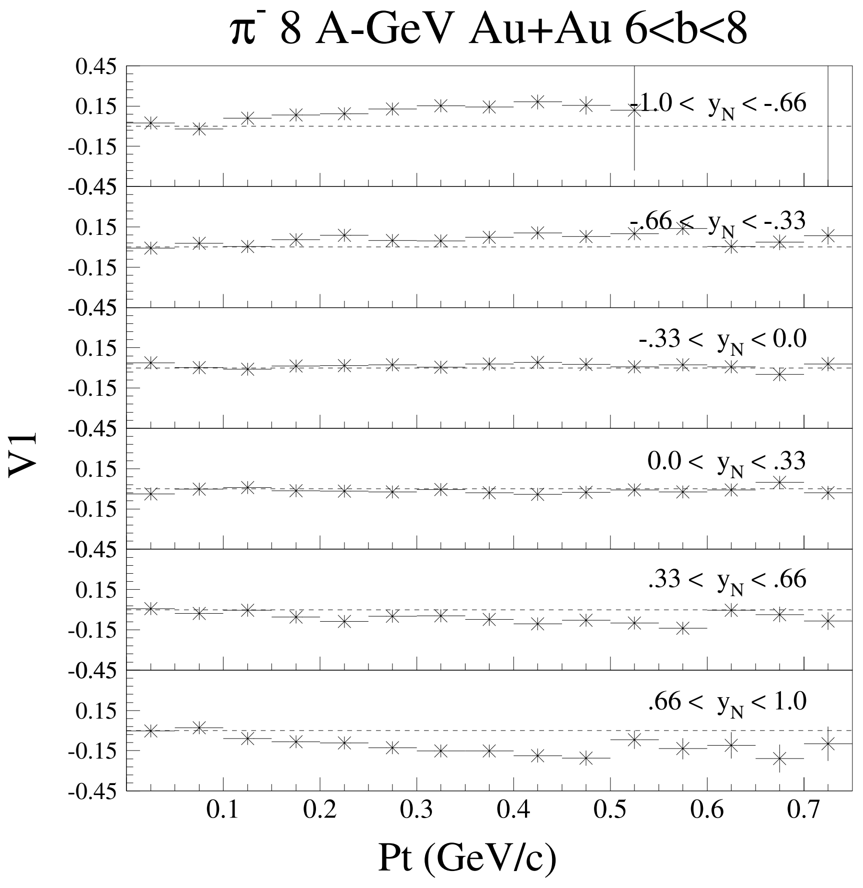

Figure 6.40: Displayed is the V1 flow value versus Transverse Momentum for $8A-GeV$ π^- from a centrality selection of $6-8\ fm$. Down the page are the six rapidity bins used for the S like curves shown in Figures 6.23, 6.24, 6.25, 6.26.

6.3.8 Protons V2 component

Figures 6.41, 6.42, 6.43 and 6.44 are the compilation of the V2 signal for the protons. As was discussed in Chapter 5 the V2 or elliptical flow signal is a maximum in the mid-rapidity region, so these plots were generated using only the window of rapidity in $\pm.1$ units of rapidity. The four panels displayed are once again the same centrality selections that have been used before. Note that the plots display the fit results which have been corrected for reaction plane dispersion. The "error" reported is the combination of the statistical error and the systematic error of the reaction plane correction factor included. The plots themselves have had no dispersion correction factor applied.

First we note that in the $2\,A-GeV$ energy sample we see an enhancement of particles in the $\pm 90^\circ$ bins. This indicates a squeeze out or negative elliptic flow signal. As we proceed to the more central collisions we see that the V2 flow weakens. It becomes not inconsistant with zero at the most central bin of $0-2\,fm$ as required.

As we continue up in incident beam energy we see that the elliptic flow signal effectively disappears at the $4\,A-GeV$ energy sample as in [Pink99]. This indicates a transition point from out of plane to in plane as we will see by the 6 and $8\,A-GeV$ energies.

Once we reach the energies of 6 and $8\,A-GeV$ we see that indeed the elliptical flow signal has changed signs to positive elliptic flow. This is in agreement with [Pink99]. This indicates that the particles are being emitted in the reaction plane rather that

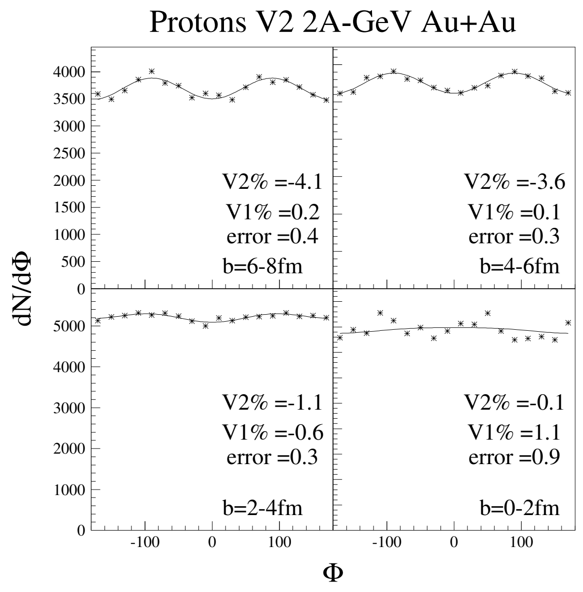

Figure 6.41: Extracted V2 for Protons at 2 $A-GeV$ in the narrow rapidity window of ±.1. The panels are for increasing centrality.

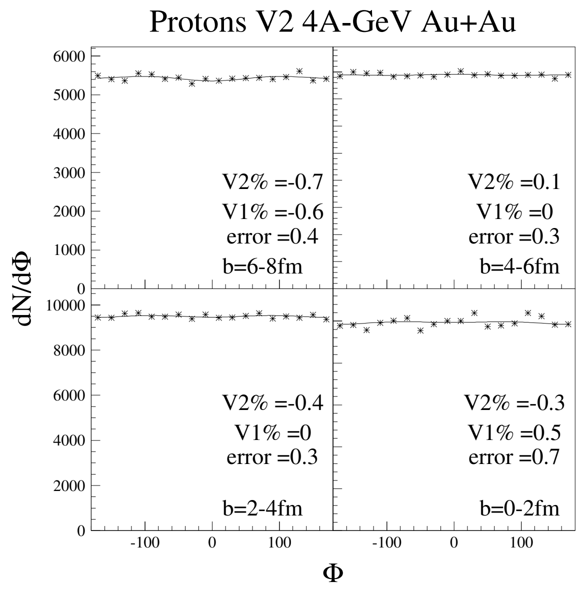

Figure 6.42: Extracted V2 for Protons at 4 $A-GeV$ in the narrow rapidity window of ±.1. The panels are for increasing centrality.

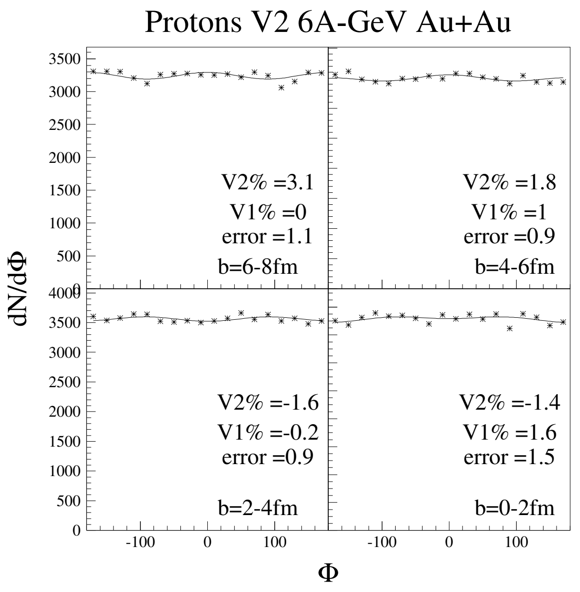

Figure 6.43: Extracted V2 for Protons at 6 $A - GeV$ in the narrow rapidity window of ±.1. The panels are for increasing centrality.

perpendicular to as before. We can see this in the Figures 6.43, 6.44.

6.3.9 π^+ V2 component

Figures 6.45, 6.46, 6.47 and 6.48 are the compilation of the V2 signal for the π^+. The structure used here is the same as that of the protons above. We see here that the pions follow the trends of the protons. They do not appear to be generating an anti-elliptic flow signal as compared to the protons.

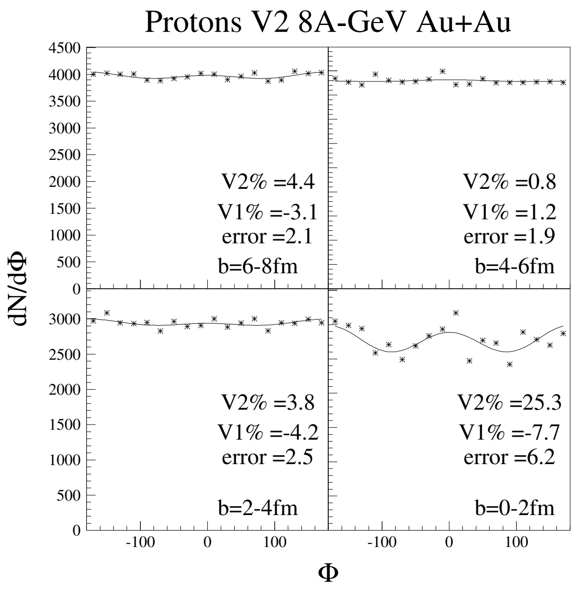

Figure 6.44: Extracted V2 for Protons at 8 $A-GeV$ in the narrow rapidity window of ±.1. The panels are for increasing centrality.

600
500
400
300
200
100
0
90
80
70
60
50
40
30
20
10
0

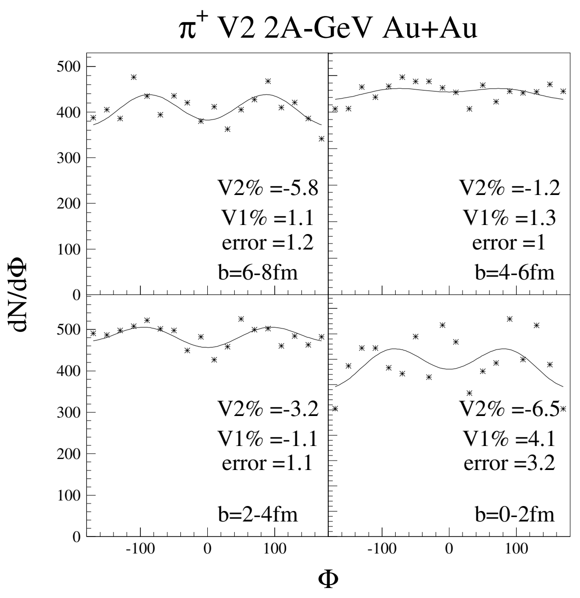

Figure 6.45: Extracted V2 for π^+ at 2 $A-GeV$ in the narrow rapidity window of ±.1. The panels are for increasing centrality.

-100 0 100 -100 0 100

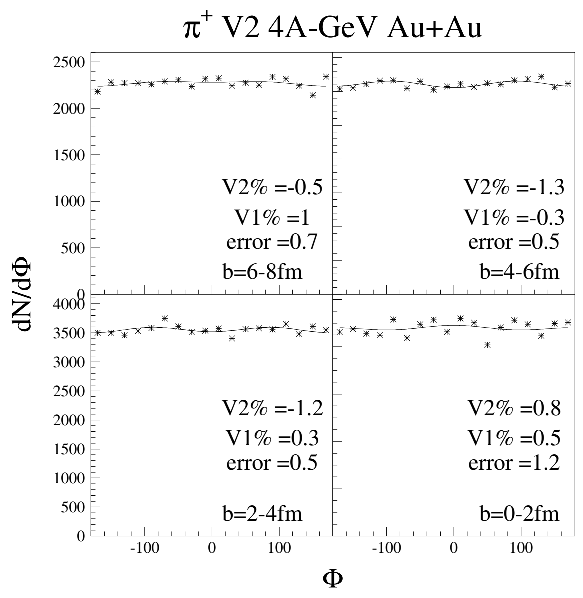

Figure 6.46: Extracted V2 for π^+ at 4 $A - GeV$ in the narrow rapidity window of ±.1. The panels are for increasing centrality.

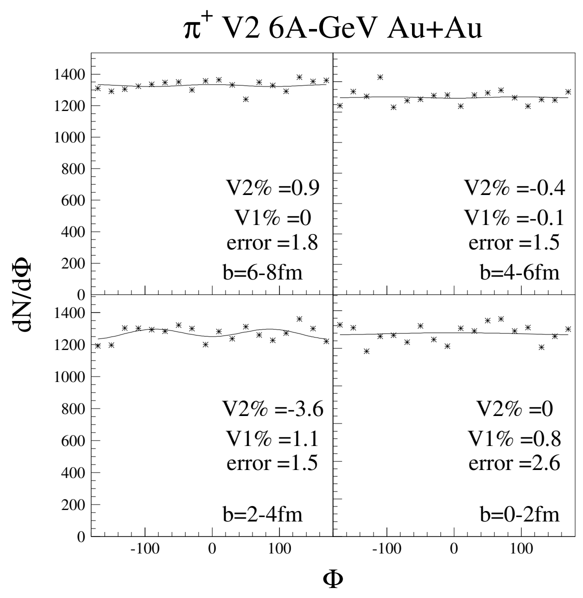

Figure 6.47: Extracted V2 for π^+ at 6 $A - GeV$ in the narrow rapidity window of ±.1. The panels are for increasing centrality.

1800
1600
1400
1200
1000
800
600
400
200
250
200
150
100
50
0

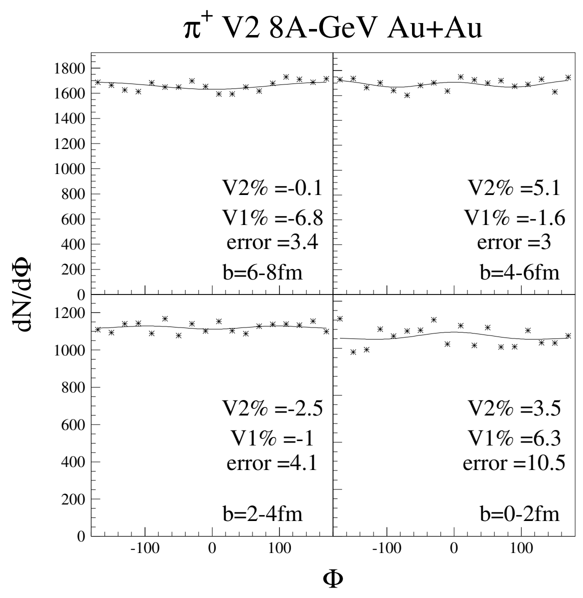

Figure 6.48: Extracted V2 for π^+ at 8 $A-GeV$ in the narrow rapidity window of ±.1. The panels are for increasing centrality.

6.3.10 π^- V2 component

Figures 6.49, 6.50, 6.51 and 6.52 are the compilation of the V2 signal for the π^-. The structure used here is the same as above. We see here that the pions follow the trends of the protons. They do not appear to be generating an anti-elliptic flow signal as compared to the protons. Table 6.4 and Figures 6.53 and 6.54 depict the trends of the observable as before.

6.3.11 Fourier V2 component Excitations

Here we have compiled the trends of the Fourier V2 component in Table 6.4. I have also displayed the beam energy dependence in Fig. 6.53 and the centrality

-100 0 100 -100 0 100

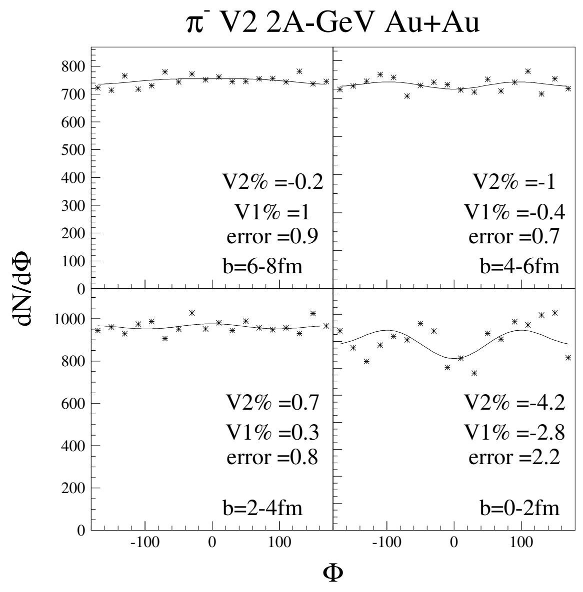

Figure 6.49: Extracted V2 for π^- at 2 $A-GeV$ in the narrow rapidity window of ±.1. The panels are for increasing centrality.

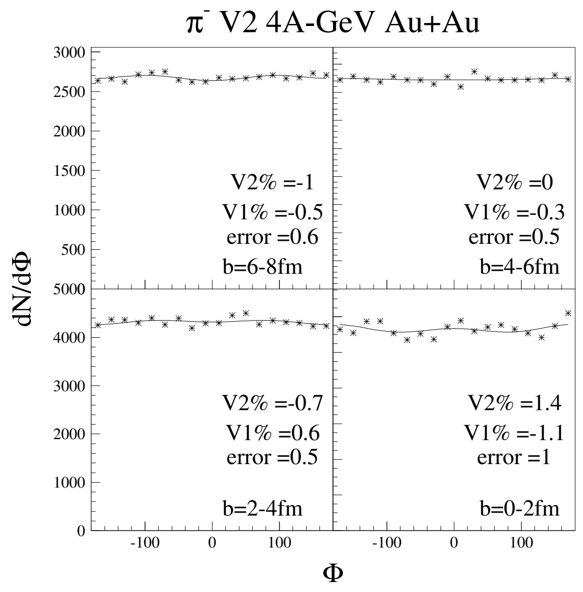

Figure 6.50: Extracted V2 for π^- at 4 $A-GeV$ in the narrow rapidity window of ±.1. The panels are for increasing centrality.

2000
1750
1500
1250
1000
750
500
250
0
800
700
600
500
400
300
200
100
0

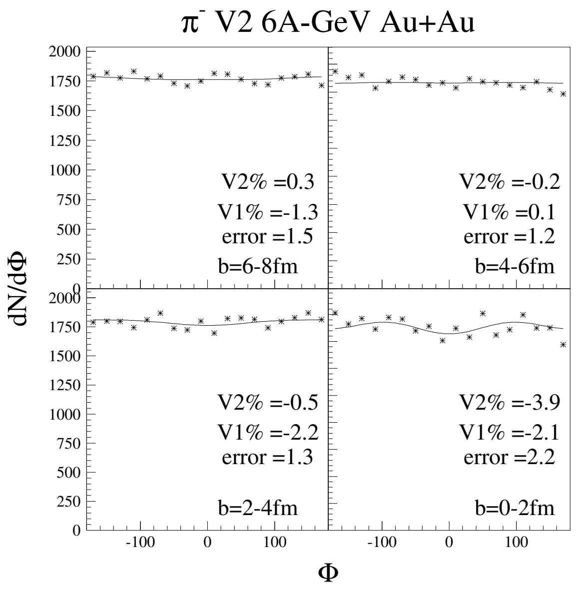

Figure 6.51: Extracted V2 for π^- at 6 $A-GeV$ in the narrow rapidity window of ±.1. The panels are for increasing centrality.

3000
2500
2000
1500
1000
500
0
350
300
250
200
150
100
50
0

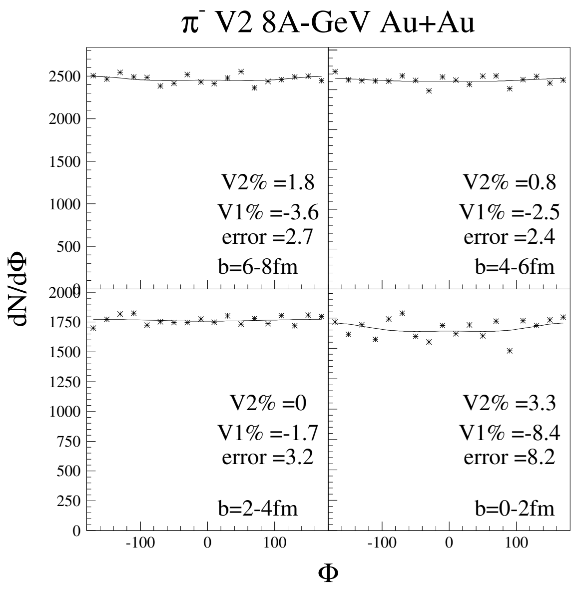

Figure 6.52: Extracted V2 for π^- at 8 $A-GeV$ in the narrow rapidity window of ±.1. The panels are for increasing centrality.

-100 0 100 -100 0 100

-100 0 100 -100 0 100

Energy	Impact	V2 %		
		Protons	π^+	π^-
2	0-2	$-.1 \pm .9$	-6.5 ± 3.2	-4.2 ± 2.2
	2-4	$-1.1 \pm .3$	-3.2 ± 1.1	$.7 \pm .8$
	4-6	$-3.6 \pm .3$	-1.2 ± 1.0	$-1. \pm .7$
	6-8	$-4.1 \pm .4$	-5.8 ± 1.2	$-.2 \pm .9$
4	0-2	$-.3 \pm .7$	$.8 \pm 1.2$	1.4 ± 1.0
	2-4	$-.4 \pm .3$	$-1.2 \pm .5$	$-.7 \pm .5$
	4-6	$.1 \pm .3$	$-1.3 \pm .5$	$0 \pm .5$
	6-8	$-.7 \pm .4$	$-.5 \pm .7$	$-1 \pm .6$
6	0-2	1.4 ± 1.5	0 ± 2.6	-3.9 ± 2.2
	2-4	$1.6 \pm .9$	-3.6 ± 1.5	$-.5 \pm 1.3$
	4-6	$1.8 \pm .9$	$-.4 \pm 1.5$	$-.2 \pm 1.2$
	6-8	3.1 ± 1.1	$.9 \pm 1.8$	$.3 \pm 1.5$
8	0-2	25.3 ± 6.2	3.5 ± 10.5	3.3 ± 8.2
	2-4	3.8 ± 2.5	-2.5 ± 4.1	0.0 ± 3.2
	4-6	$.8 \pm 1.9$	5.1 ± 3.0	$.8 \pm 2.4$
	6-8	4.4 ± 2.1	$-.1 \pm 3.4$	1.8 ± 2.7

Table 6.4: Compilation of the elliptic flow (V2) signal for protons, π^+ and π^-. In the narrow rapidity window of $\pm .1$. The reader is referred to Table 3.3 for a listing of the reaction plane resolution correction factors applied to the data listed above.

(impact parameter) dependence in Fig. 6.54. In Fig. 6.53 we can easily see the transition from out of plane to in plane elliptic flow at about 4 $A - GeV$ in support of the findings in [Pink99].

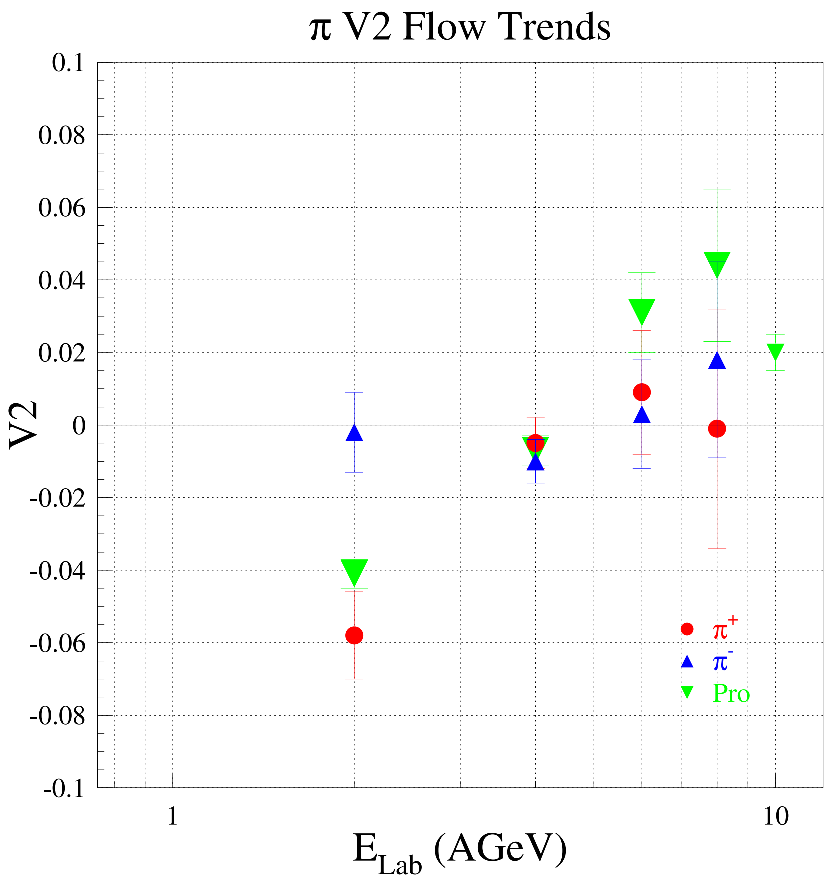

Figure 6.53: Extracted V2 for π^-, π^+, and protons for the 4 incident beam energies. The data are taken from the $6-8\,fm$ range for pions and the b=$4-6\,fm$ bin for the protons. Data from 2,4,6 and 8 $A-GeV$ from E895 and 10.8 $A-GeV$ from E877 are shown.

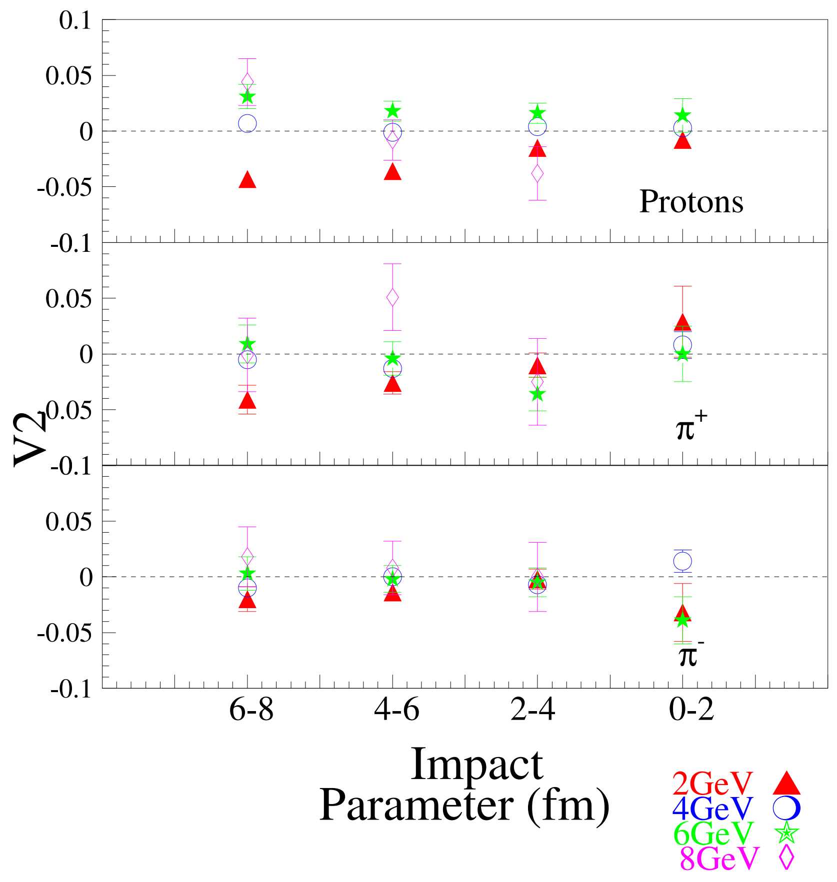

Figure 6.54: Extracted V2 for π^-, π^+, and protons for the 4 incident beam energies as a function of impact parameter. All have been corrected for dispersion of the reaction plane. Note that all points are displayed with the exception of the $8\,A-GeV$ proton point for the $0-2\,fm$ bin, which is off scale at $25 \pm 6.2\%$ (note that this uncertainty is anomalously large.

Chapter 7

Theory

7.1 Present Day Theories

Present day theories can be generalized into two large categories. These are hydrodynamic and transport theories. Hydrodynamic theories attempt to model Heavy Ion interactions by using fluid transport equations and assuming that the nucleus and interactions can be modeled as a fluid. These models have been notoriously difficult to interpret and at present require assumptions such as equilibrium conditions that are difficult to justify.

Transport models are based fundamentally on the nucleon interactions and attempt to model heavy ion interactions by Monte Carlo. This is accomplished, in general, by propagating each of the parent nucleons through phase space independently. As they approach each other (based on some criterion) they are interacted using known measured cross sections. The resultants (with the possibility of particle production) are then continued on until the density of the phase space reaches a low enough threshold that the model declares the reaction over. These interactions are of course inherently two body and in general assume that the cross sections that have been measured are applicable in medium. That is to say that protons and pions do not interact with each other differently in free space as opposed to when they are bound in a nucleus.

Modifications to this general premise include scaling or changing the cross sections to attempt in medium dependence, including mean fields that are responsible for keeping the nucleus in a bound state at low excitation energies, and introducing angular momentum conservation schemes. Two notable theories in this category are RQMD and ART. Each will be discussed below.

In each of these there are many settings that affect the various parameters used in the model. Some changes that can be made to the models include scaling of the cross sections, the distance at which nucleons are interacted or setting limits on densities. As a result the possibility of inadvertent mistakes due to not fully understanding the settings of the model are a significant possibility. I therefore, choose to compare to published data by the authors of the various models whenever possible, rather than attempting to use the models myself.

7.2 RQMD

In the case of RQMD (Relativistic Quantum Molecular Dynamics), or its updated version UrQMD, we did run the event simulator to produce simulated data for comparison to our pion flow ($\langle P_x/m \rangle$) data sets only. The reader is referred to the following articles for a description of the model [Bass98]. The version used here was RQMD 2.3. This model has had reasonable success in describing heavy ion collisions in this energy region. For reference [Bass98]. The proton signals have been studied by some of the authors of the RQMD model. Figure 7.1 shows the comparison of the model to the E895 6 $A - GeV$ data set. The figure is taken from [Soff99]. One sees here reasonable agreement between the model and the proton flow signal.

The elliptic flow signal (V2) for the protons is displayed in Fig. 7.2 also taken

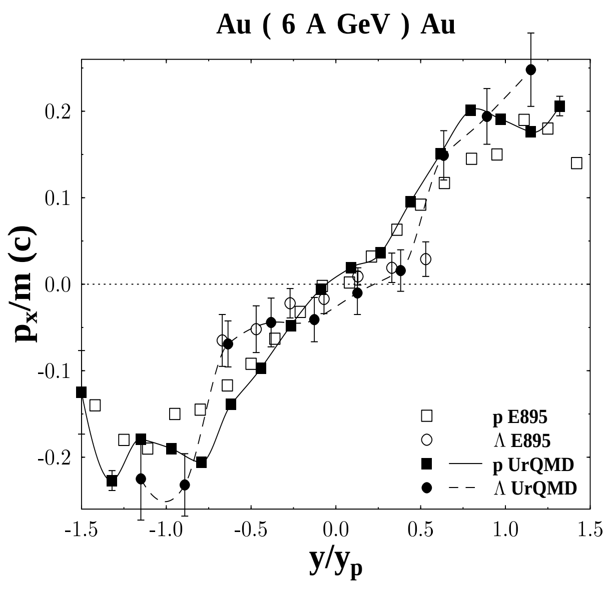

Figure 7.1: UrQMD comparison to E895 proton $\langle P_{x'} \rangle / m$ data. The plot has been taken from [Soff99].

from [Soff99] and in Fig. 7.3. It should be noted that the impact parameter selections for the two plots are different. The point here is that the data are reproduced only if the effects of a meanfield are present in the model. The cascade mode is unable to reproduce the squeeze-out or negative elliptic flow observation. We therefore, conclude that the meanfield is an important aspect of the nucleon interactions, with the reservation that the pions are not well described by the models as will be seen below.

As mentioned above the pion flow signal has not been studied by the authors of RQMD. We therefore, ran the model ourselves and display the results in Fig. 7.4 which shows the flow excitation. The RQMD was run in two modes, one with the

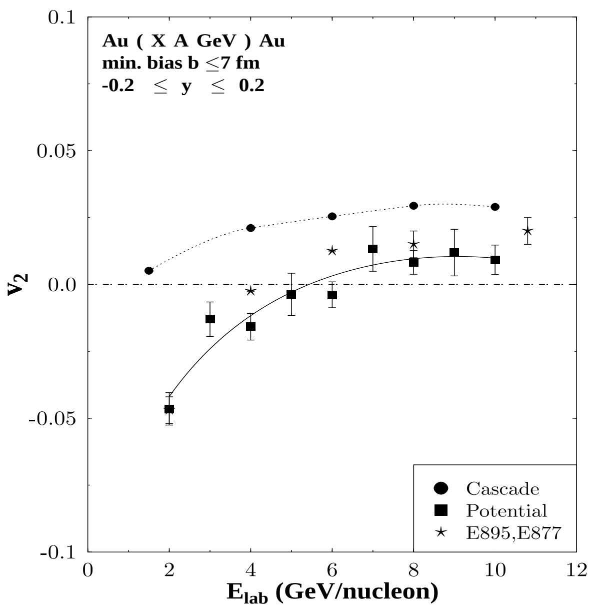

Figure 7.2: UrQMD V2 flow ([Soff99]) comparison with E895 proton data ([Pink99]). The impact parameter selections made here are different from those in this document. Note that the $2\,A - GeV$ data point falls under the "Potential" plot point at a V2 of -0.05.

meanfield and one in a pure cascade mode. The two are displayed on the graph. We see that neither completely describes the pion data. It is interesting to note that all of the present meanfields used in the models are for nucleons only. No meanfield has been added for pion interactions. The difference in the flow with and without the nucleon meanfield is due to the strong interaction of the pions with the nucleon distributions in phase space. As the meanfield moves the nucleons around in phase space the shadowing and absorption of the pions change. When looking at the pions we note that the meanfield appears to better match the π^- signal and the cascade mode does better for the π^+ signal.

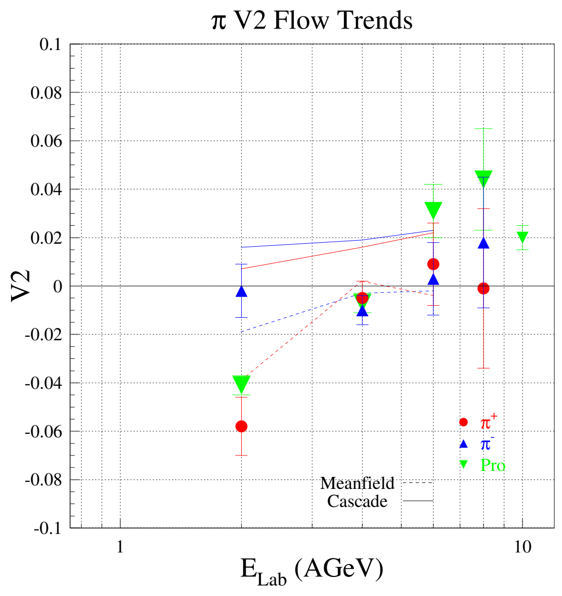

Figure 7.3: RQMD (v2.3) V2 flow comparison with E895 proton and pion data. Note that the impact parameter selections here are consistant with the rest of those made in this document. Proton signals are taken for impact parameter bin $4 - 6\ fm$ while pions are from $6 - 8\ fm$.

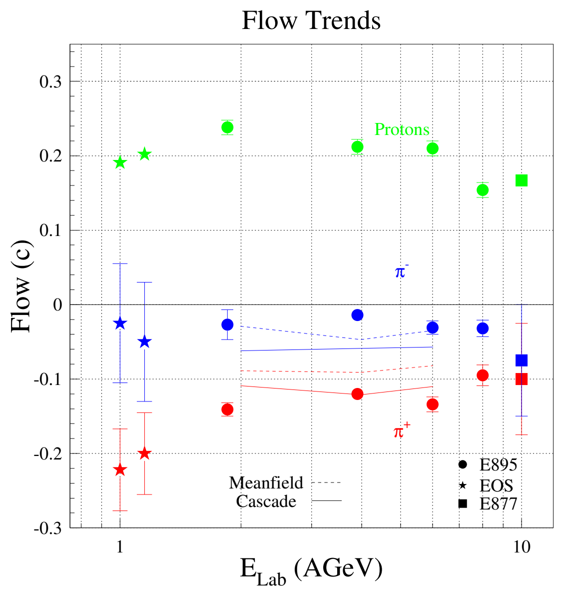

Figure 7.4: Flow excitation with RQMD theory.

Here we must conclude that the pions are not well addressed by the model RQMD. A meanfield approach to the pions appears to be needed. As a result of the strong interaction of the nucleons and pions, the conclusions concerning the nucleons may change as the model better addresses the pion observations.

One of the most important aspects of the flow data is that of the EoS (Equation of State). Comparisons such as Figures 7.2 and 7.1 led the authors of the UrQMD code to a nuclear compressibility of $\kappa = 380\,MeV$. This is the stiff equation of state. To remind the reader this is the compressibility that was determined to be necessary for the lower energy BEVALAC [Part97] and SIS/GSI data [FOPI96]

7.3 ART

Another cascade theory has been developed by Li and Ko, with details of the model discussed in [LiKo95] and is called ART (A Relativistic Transport). The authors have shown some agreement with experimental data [LiKo96], [LiKo96b], [LiKo96c], [LiKo96d], [LiKo98] and [LiKo99]. The model includes some in medium and mean field effects. The authors have used this model to make predictions and comparisons to various flow signals. These will be recapped and comparisons will be made to the data presented here. Li and Ko studied the impact parameter dependence of the pion flow signal in their paper [LiKo96]. They argued that the pion signal develops from the competition between two effects. The first is from the nucleon resonances. The participant nucleons and resonances form a strong flowing system and therefore, with their subsequent decays they produce pions with flow. The second effect is from shadowing due to the nucleon spectator matter that is in the flow plane. As pions leave the hot dense central interaction region, they strongly interact (See Section 1.3) with this spectator matter and are rescattered or absorbed, leaving a depletion of pions in the flow plane and therefore, anti-flow. The amount of spectator influence is dependent on impact parameter. They argue that as one approaches central collisions the spectator matter diminishes. They then predict a transition for the more central collisions (below 7 fm for 10.8 $A-GeV$ Au+Au) for the pions from anti-flow to flow. They support this with measurements made at the BEVALAC [Kint97] and SIS/GSI [Fopi93] which established the transition at about 3 fm. They argue that as the energy increases the spectator matter moves out of the way in phase space due to large longitudinal momentum. Note that since the spectator matter velocity is nearly c, this explanation is a bit difficult to follow. This then leads to the decreasing effect of the spectator matter and therefore, the increase in the beam energy of the transition point. Measurements of this effect can be made at E895 as well. The minimum bias data set covers impact parameters from 0 to 8 fm and was shown in Chapter 6 in Figure 6.14. In this plot we see that the impact parameter dependence shows a possible transition at $2 - 4$ fm for the π^+ and a shift of the transition out to $4 - 6$ fm for the π^-. This would indicate that either the spectator matter has not moved far enough in phase space to stop competing with the baryon resonances or their is another mechanism involved. The differences in the two species pions may shed some light on this. It has been argued that π^- signal is weaker because they are drawn back into the flow plane possibly by coulomb interactions. They therefore, should interact more strongly with the spectator matter. When looking at the data we see that the π^- transition is indeed moving out to the higher impact parameter. As mentioned above, this model does not have a pion meanfield either. This interaction may be needed to explain the transition point of the pion data from flow to anti-flow as in Fig. 6.14.

In addition to the analysis above, the same authors have published another article with the same ART model. This paper [LiKo99] discusses the V2 components of protons and pions (no pion species dependence was studied) in the Fourier method. The plot is reproduced here for discussion. Figure 7.5 shows the ART models comparison to the E895 proton V2 data published by [Pink99]. The same figure also displays predictions for the pion V2 signal as well and I have added the pion measurements from this dissertation to that of Li and Ko's graphic. We will compare these in a moment. The authors were led by their models conclusions to an EoS with a κ of 380. This agrees with the findings of the UrQMD model discussed above. The authors however, disagree with the findings of [Pink99] which found evidence of a change in the EoS from stiff to soft after the V2 transition from negative to positive elliptic flow for protons. The findings of [Pink99] were based on the BEM [Dani98] model. Li and Ko found that only a stiff equation of state was needed to explain the proton findings with their ART model. Li and Ko then argue that the pions may be the key to disentangling the differences between the competing models.

Considering this, as stated above I have added the E895 pion V2 signals to Fig. 7.5 for comparison. We see that the stiff EoS prediction does not match the pions well. Differentiating the species of pions in the model may be necessary for a clearer understanding of the models predictions. It should be noted however that it is the stiff EoS that most nearly approaches the data. Once again we are forced to conclude that although the nucleons are well described, the pions are not.

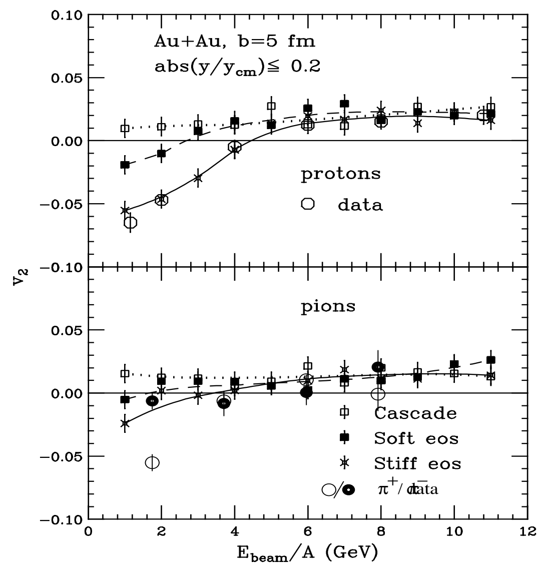

Figure 7.5: Comparison of ART (reference in the text) and E895 proton and pion data. Note that the curves have been placed on the plot to guide the eye.

Chapter 8

Conclusions

In conclusion, we have observed many of the flow signals from both pions and protons. I have shown that the proton flow $\langle P_{x'} \rangle / m$ signal is falling smoothly throughout the incident energy range of $2 - 8\,A - GeV$ from a maximum value at $\sim 2\,A - GeV$ of $.240\,c$. The data match quite well with the data of EOS and E877 which bounded the energy region. The protons were seen to peak their flow signal in the mid-central collisions of $4 - 6\,fm$. The V1 signal for the protons was seen to be very linear with rapidity, and its slope was seen to follow the trends $\langle P_{x'} \rangle / m$ signal very closely. The V1 signal was seen to be at its maximum of $\sim 30\%$ in the $4 - 6\,fm$ bin of the $2\,A - GeV$ data set.

The pions were shown to anti-flow in both the $\langle P_{x'} \rangle / m$ signal as well as the V1 signal. The pions always showed a much weaker signal than the protons in the directed flow signals as well as the V1 and V2 signals. The pions were seen to be falling smoothly throughout the energy region with no indication of a maximum value in the measured data sets to date. The largest flow for protons and pions being in the $1.0\,A - GeV$ data sets measured by EOS and FOPI experiments. The pions were shown to also have no maximum observed flow value in their centrality dependence. The largest flows for the pions was in the most peripheral bin of $6 - 8\,fm$. The pions exhibited a strong species dependence in each of these observables. The π^- flow was always smaller than the π^+. The π^- flow also indicated a transition from anti-flow behavior to flow behavior in the $2 - 4\,fm$ region, whereas the π^+s showed generally a smooth trend to zero flow for the most central collisions.

In the case of the elliptical flow or V2 observable, the pions and protons exhibited very similar trends. They both were shown to have negative elliptic flow or squeeze-out for energies less than $4A-GeV$. They then transitioned to preferentially in- plane elliptic flow or squeeze-in for energies greater than $4\,A-GeV$ as seen in Figures 7.2 and 7.3.

The various theory models that were studied did a very good job of describing the proton signals. Conclusions as to the EoS (Equation of State) were reached, indicating a stiff equation. That is a bulk compressibility for nuclear matter of $\kappa \sim 380\,MeV$ is preferred over the soft bulk modulas $\kappa \sim 200\,MeV$. The models did not address the pions well. This casts some doubt on these conclusions due to the strong interactions between the pions and the nucleons. This leads me to conclude that theoretical work needs to be done to better understand the pions in the light of these values of the studied observables in this dissertation.

Appendix A

Reaction Plane Calibration

This appendix contains graphics of the reaction plane weighting function for each of the incident beam energies. Chapter 4 discusses how these are made and used. Also, included is the reaction plane resolution test done by finding the correlations between two sub-events as described in Chapter 3.

Figure A.1: Displayed is the weighting function used to correct for azimuthal anisotropies due to acceptance of the $2\,A-GeV$ reaction plane determination. Note that the weigting scheme removes all data from a Φ azimuth in which a weight of any given bin exceeds 5.0.

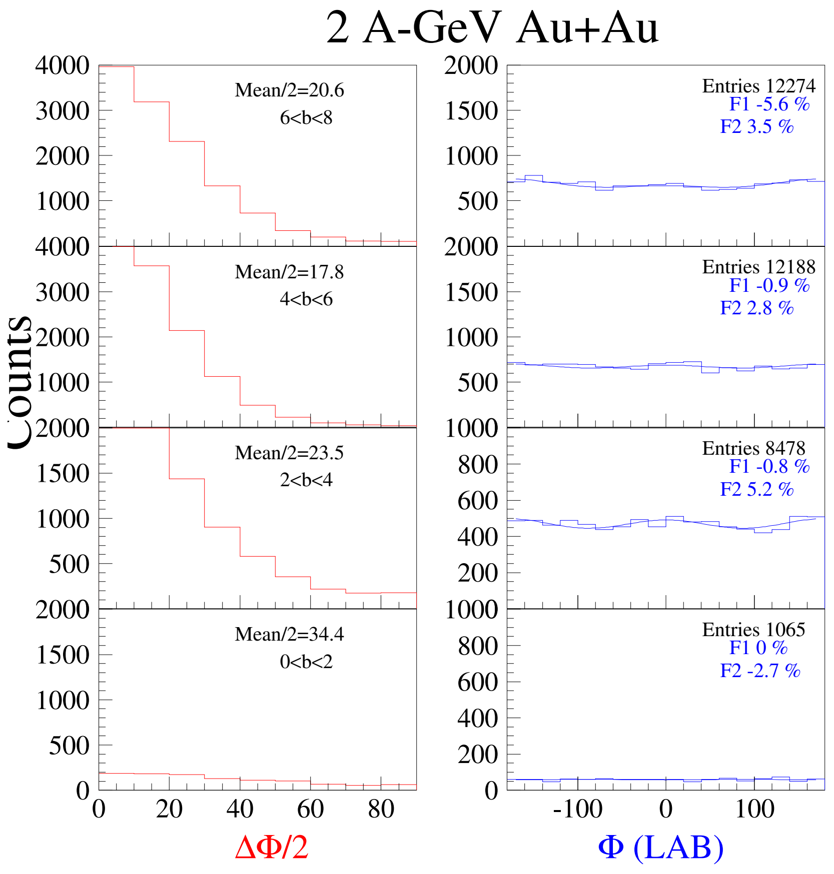

Figure A.2: Reaction Plane Resolution Test for $2\,A-GeV$ On the left is the subevent comparison (Φ_1 -Φ_2)/2 on the right is the reaction plane determined in the lab frame with the weighting for acceptance correction applied and the fit measure of its effect (Eq. (4.1)). Down the page are different centrality selections. Table 3.3 catalogs the reaction plane dispersion correction factors associated with the 4 panels on the left.

0 20 40 60 80 -100 0 100

0 20 40 60 80 -100 0 100

0 20 40 60 80 -100 0 100

Figure A.3: Displayed is the weighting function used to correct for azimuthal anisotropies due to acceptance of the 4 $A-GeV$ reaction plane determination.

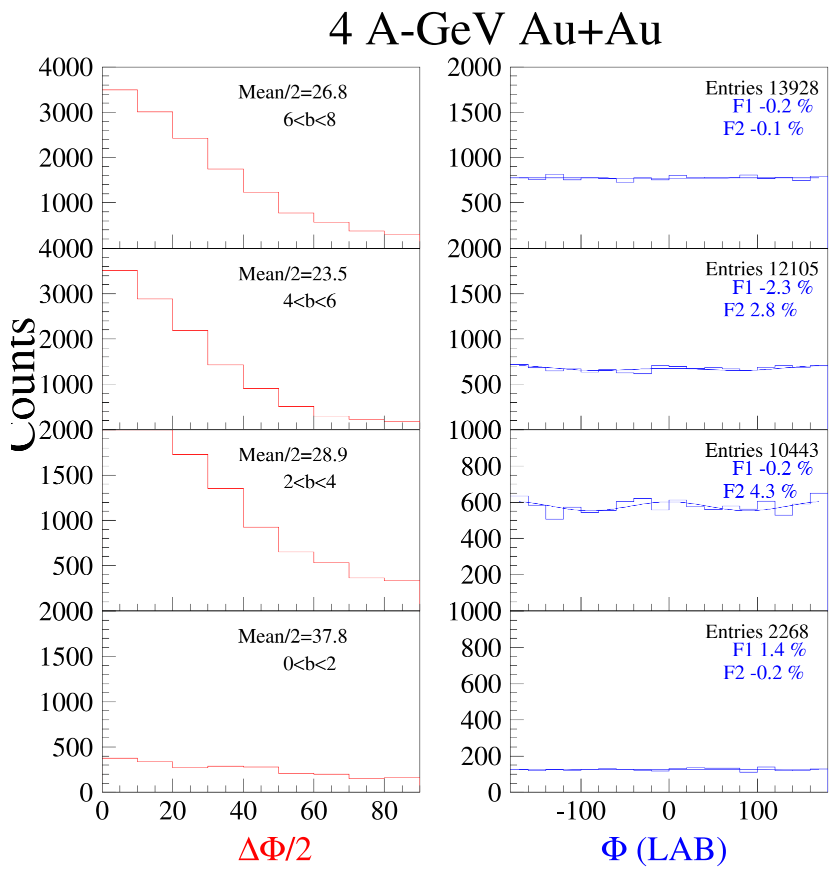

Figure A.4: Reaction Plane Resolution Test for $4\,A-GeV$ On the left is the subevent comparison (Φ_1 - Φ_2)/2 on the right is the reaction plane determined in the lab frame with the weighting for acceptance correction applied and the fit measure of its effect (Eq. (4.1)). Down the page are different centrality selections. Table 3.3 catalogs the reaction plane dispersion correction factors associated with the 4 panels on the left.

0 20 40 60 80 -100 0 100

0 20 40 60 80 -100 0 100

0 20 40 60 80 -100 0 100

Figure A.5: Displayed is the weighting function used to correct for azimuthal anisotropies due to acceptance of the 6 $A-GeV$ reaction plane determination.

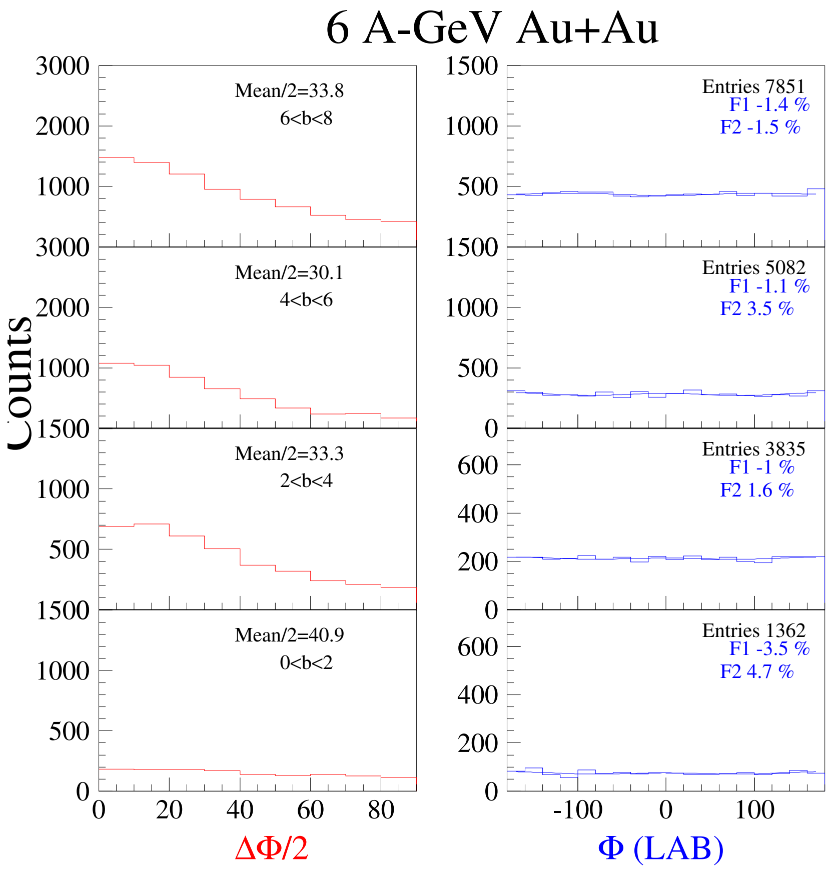

Figure A.6: Reaction Plane Resolution Test for $6\,A-GeV$ On the left is the subevent comparison (Φ_1 - Φ_2)/2 on the right is the reaction plane determined in the lab frame with the weighting for acceptance correction applied and the fit measure of its effect (Eq. (4.1)). Down the page are different centrality selections. Table 3.3 catalogs the reaction plane dispersion correction factors associated with the 4 panels on the left.

0 20 40 60 80 -100 0 100

0 20 40 60 80 -100 0 100

0 20 40 60 80 -100 0 100

Figure A.7: Displayed is the weighting function used to correct for azimuthal anisotropies due to acceptance of the 8 $A - GeV$ reaction plane determination.

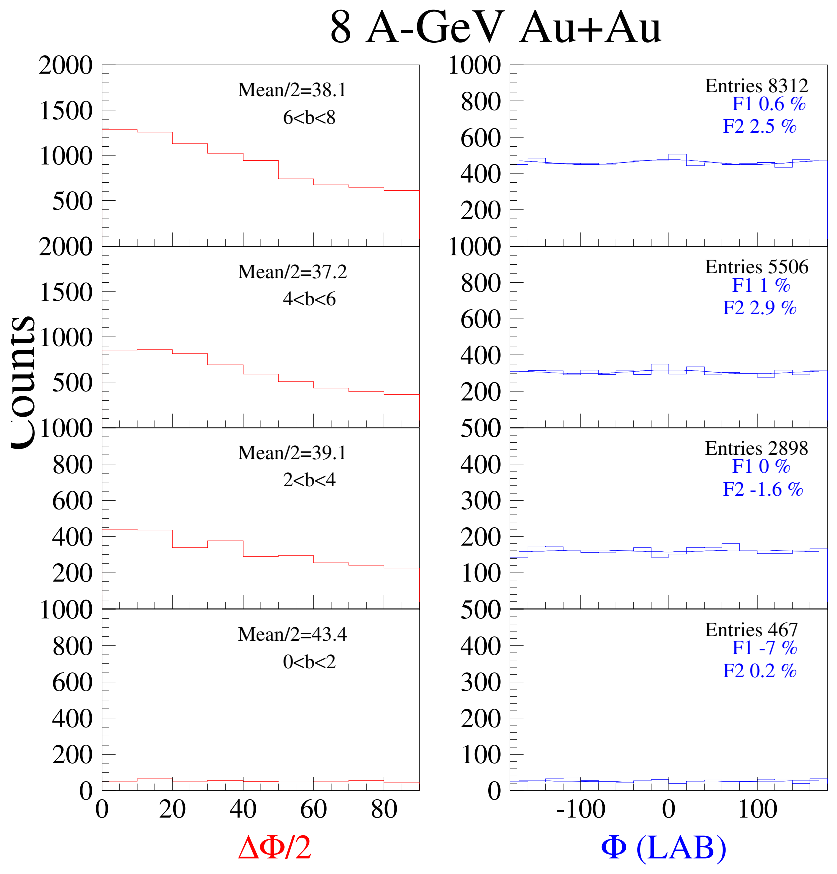

Figure A.8: Reaction Plane Resolution Test for $8\,A-GeV$ On the left is the subevent comparison (Φ_1 - Φ_2)/2 on the right is the reaction plane determined in the lab frame with the weighting for acceptance correction applied and the fit measure of its effect (Eq. (4.1)). Down the page are different centrality selections. Table 3.3 catalogs the reaction plane dispersion correction factors associated with the 4 panels on the left.

0 20 40 60 80 -100 0 100

0 20 40 60 80 -100 0 100

0 20 40 60 80 -100 0 100

Appendix B

Proton $P_{\perp}$ Acceptance

This appendix contains the $P_{\perp}$ weighting functions described in Chapter 4 for Protons. Displayed are each of the incident beam energies and impact parameter selections.

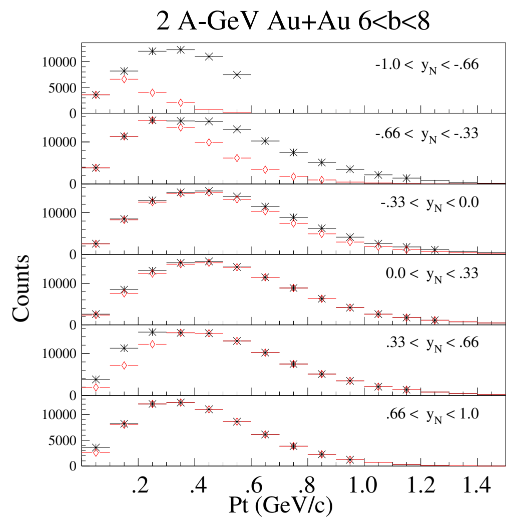

Figure B.1: $P_{\perp}$ acceptance shown for 2 $A - GeV$ proton, in the $6 - 8$ fm bin. Down the page are the 6 rapidity binnings used in the S-curves. *'s represent corrected data, diamonds uncorrected or raw data. Note that the plot is integrated over the Φ_{flow} dependence of the weighting function.

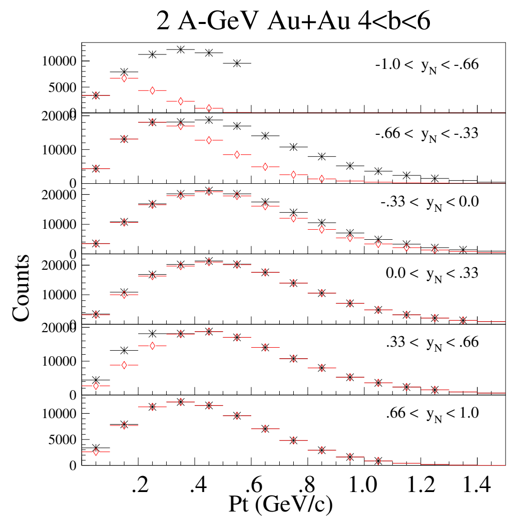

Figure B.2: $P_{\perp}$ acceptance shown for 2 $A - GeV$ proton, in the $4 - 6$ fm bin. Down the page are the 6 rapidity binnings used in the S-curves. *'s represent corrected data, diamonds uncorrected or raw data. Note that the plot is integrated over the Φ_{flow} dependence of the weighting function.

0 2 4 6 8 10 12 14
0 2 4 6 8 10 12 14
0 2 4 6 8 10 12 14
0 2 4 6 8 10 12 14
0 2 4 6 8 10 12 14
0 2 4 6 8 10 12 14

0 2 4 6 8 10 12 14
0 2 4 6 8 10 12 14
0 2 4 6 8 10 12 14
0 2 4 6 8 10 12 14
0 2 4 6 8 10 12 14
0 2 4 6 8 10 12 14

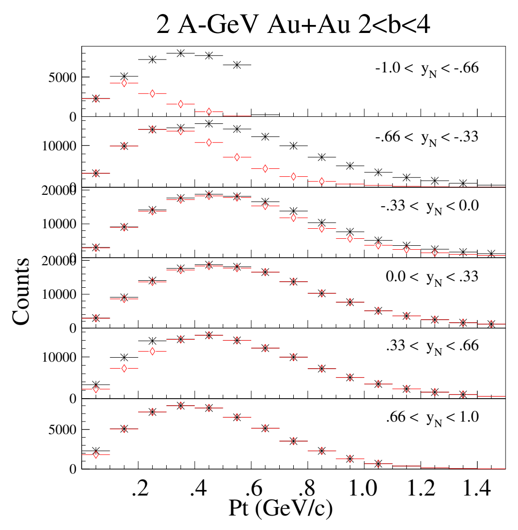

Figure B.3: $P_\perp$ acceptance shown for 2 $A-GeV$ proton, in the $2-4$ fm bin. Down the page are the 6 rapidity binnings used in the S-curves. *'s represent corrected data, diamonds uncorrected or raw data. Note that the plot is integrated over the Φ_{flow} dependence of the weighting function.

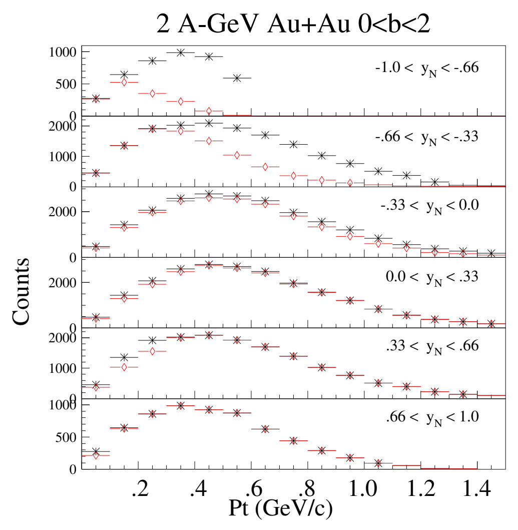

Figure B.4: $P_\perp$ acceptance shown for 2 $A-GeV$ proton, in the $0-2$ fm bin. Down the page are the 6 rapidity binnings used in the S-curves. *'s represent corrected data, diamonds uncorrected or raw data. Note that the plot is integrated over the Φ_{flow} dependence of the weighting function.

0 2 4 6 8 10 12 14

0 2 4 6 8 10 12 14

0 2 4 6 8 10 12 14

0 2 4 6 8 10 12 14

0 2 4 6 8 10 12 14

0 2 4 6 8 10 12 14

0 2 4 6 8 10 12 14

0 2 4 6 8 10 12 14

0 2 4 6 8 10 12 14

0 2 4 6 8 10 12 14

0 2 4 6 8 10 12 14

0 2 4 6 8 10 12 14

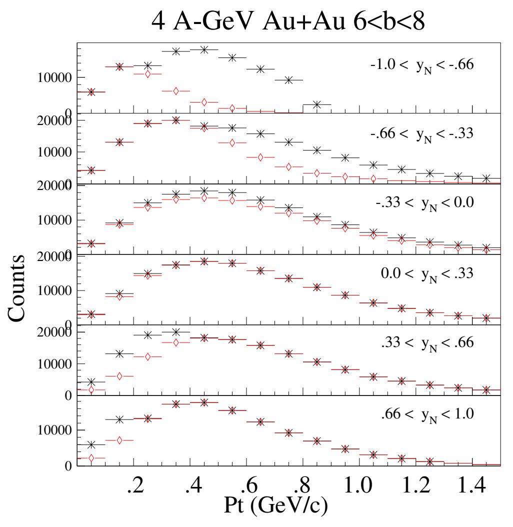

Figure B.5: $P_{\perp}$ acceptance shown for $4\ A-GeV$ proton, in the $6-8\ fm$ bin. Down the page are the 6 rapidity binnings used in the S-curves. *'s represent corrected data, diamonds uncorrected or raw data. Note that the plot is integrated over the Φ_{flow} dependence of the weighting function.

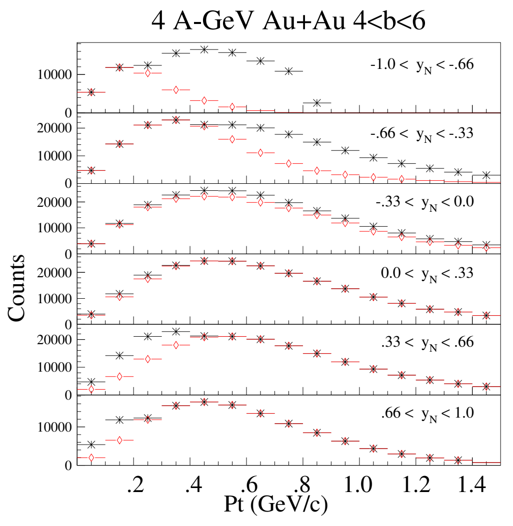

Figure B.6: $P_{\perp}$ acceptance shown for $4\ A-GeV$ proton, in the $4-6\ fm$ bin. Down the page are the 6 rapidity binnings used in the S-curves. *'s represent corrected data, diamonds uncorrected or raw data. Note that the plot is integrated over the Φ_{flow} dependence of the weighting function.

0 2 4 6 8 10 12 14
0 2 4 6 8 10 12 14
0 2 4 6 8 10 12 14
0 2 4 6 8 10 12 14
0 2 4 6 8 10 12 14
0 2 4 6 8 10 12 14

0 2 4 6 8 10 12 14
0 2 4 6 8 10 12 14
0 2 4 6 8 10 12 14
0 2 4 6 8 10 12 14
0 2 4 6 8 10 12 14
0 2 4 6 8 10 12 14

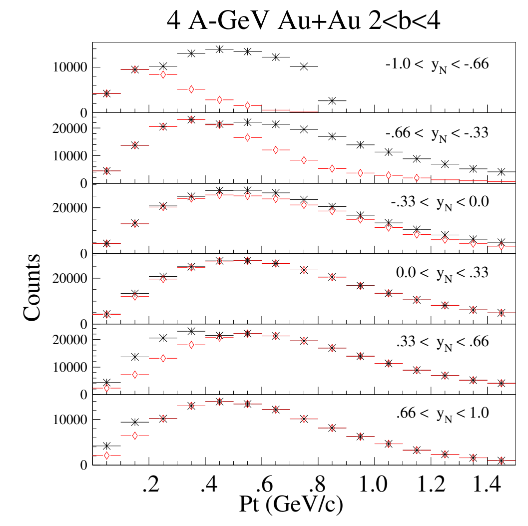

Figure B.7: $P_{\perp}$ acceptance shown for $4\ A-GeV$ proton, in the $2-4\ fm$ bin. Down the page are the 6 rapidity binnings used in the S-curves. *'s represent corrected data, diamonds uncorrected or raw data. Note that the plot is integrated over the Φ_{flow} dependence of the weighting function.

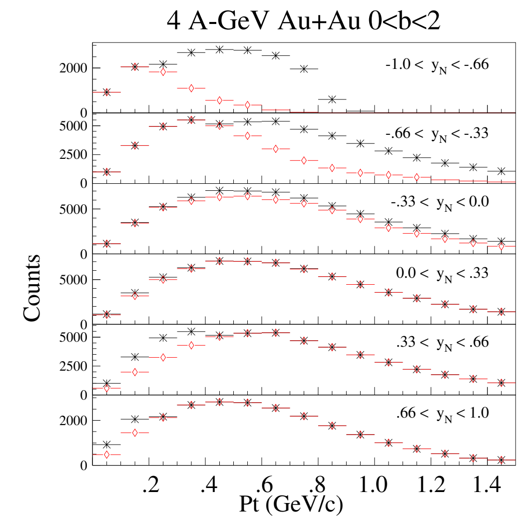

Figure B.8: $P_{\perp}$ acceptance shown for $4\ A-GeV$ proton, in the $0-2\ fm$ bin. Down the page are the 6 rapidity binnings used in the S-curves. *'s represent corrected data, diamonds uncorrected or raw data. Note that the plot is integrated over the Φ_{flow} dependence of the weighting function.

0 2 4 6 8 10 12 14

0 2 4 6 8 10 12 14

0 2 4 6 8 10 12 14

0 2 4 6 8 10 12 14

0 2 4 6 8 10 12 14

0 2 4 6 8 10 12 14

0 2 4 6 8 10 12 14

0 2 4 6 8 10 12 14

0 2 4 6 8 10 12 14

0 2 4 6 8 10 12 14

0 2 4 6 8 10 12 14

0 2 4 6 8 10 12 14

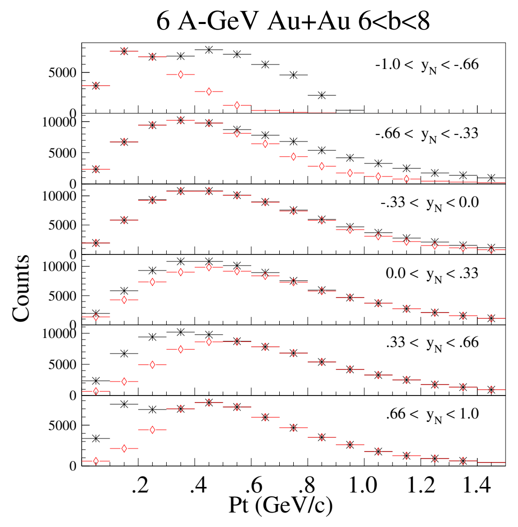

Figure B.9: $P_\perp$ acceptance shown for 6 $A-GeV$ proton, in the $6-8\ fm$ bin. Down the page are the 6 rapidity binnings used in the S-curves. *'s represent corrected data, diamonds uncorrected or raw data. Note that the plot is integrated over the Φ_{flow} dependence of the weighting function.

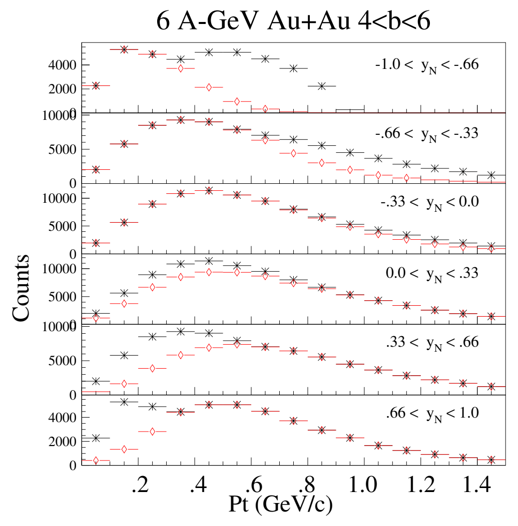

Figure B.10: $P_\perp$ acceptance shown for 6 $A-GeV$ proton, in the $4-6\ fm$ bin. Down the page are the 6 rapidity binnings used in the S-curves. *'s represent corrected data, diamonds uncorrected or raw data. Note that the plot is integrated over the Φ_{flow} dependence of the weighting function.

0 2 4 6 8 10 12 14

0 2 4 6 8 10 12 14

0 2 4 6 8 10 12 14

0 2 4 6 8 10 12 14

0 2 4 6 8 10 12 14

0 2 4 6 8 10 12 14

0 2 4 6 8 10 12 14

0 2 4 6 8 10 12 14

0 2 4 6 8 10 12 14

0 2 4 6 8 10 12 14

0 2 4 6 8 10 12 14

0 2 4 6 8 10 12 14

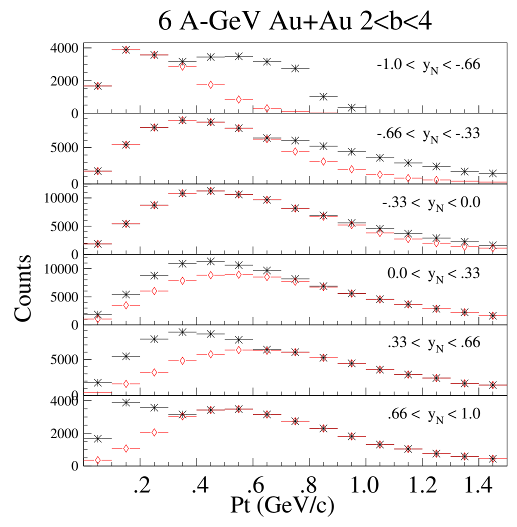

Figure B.11: $P_\perp$ acceptance shown for $6\,A-GeV$ proton, in the $2-4\,fm$ bin. Down the page are the 6 rapidity binnings used in the S-curves. *'s represent corrected data, diamonds uncorrected or raw data. Note that the plot is integrated over the Φ_{flow} dependence of the weighting function.

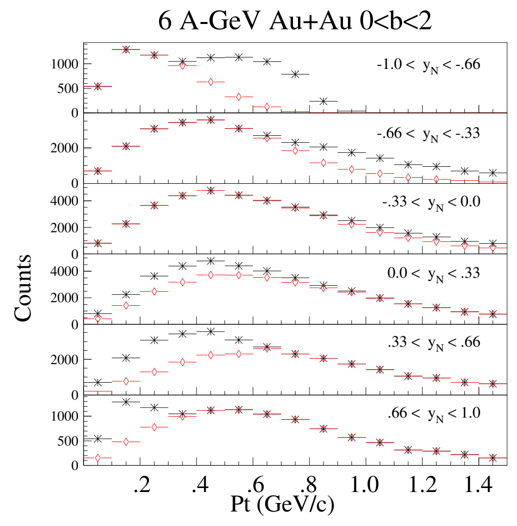

Figure B.12: $P_\perp$ acceptance shown for $6\,A-GeV$ proton, in the $0-2\,fm$ bin. Down the page are the 6 rapidity binnings used in the S-curves. *'s represent corrected data, diamonds uncorrected or raw data. Note that the plot is integrated over the Φ_{flow} dependence of the weighting function.

0 2 4 6 8 10 12 14
0 2 4 6 8 10 12 14
0 2 4 6 8 10 12 14
0 2 4 6 8 10 12 14
0 2 4 6 8 10 12 14
0 2 4 6 8 10 12 14

0 2 4 6 8 10 12 14
0 2 4 6 8 10 12 14
0 2 4 6 8 10 12 14
0 2 4 6 8 10 12 14
0 2 4 6 8 10 12 14
0 2 4 6 8 10 12 14

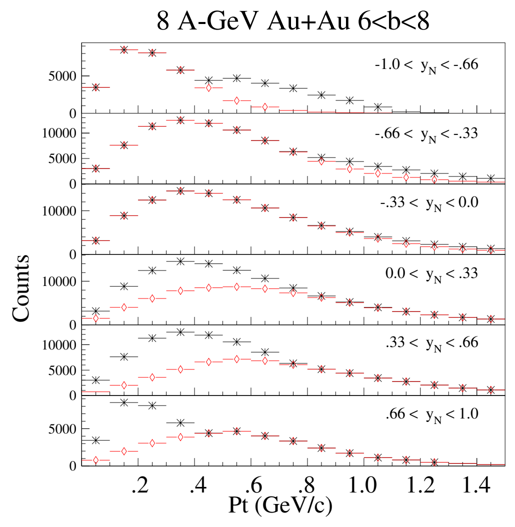

Figure B.13: $P_\perp$ acceptance shown for $8\,A-GeV$ proton, in the $6-8\,fm$ bin. Down the page are the 6 rapidity binnings used in the S-curves. *'s represent corrected data, diamonds uncorrected or raw data. Note that the plot is integrated over the Φ_{flow} dependence of the weighting function.

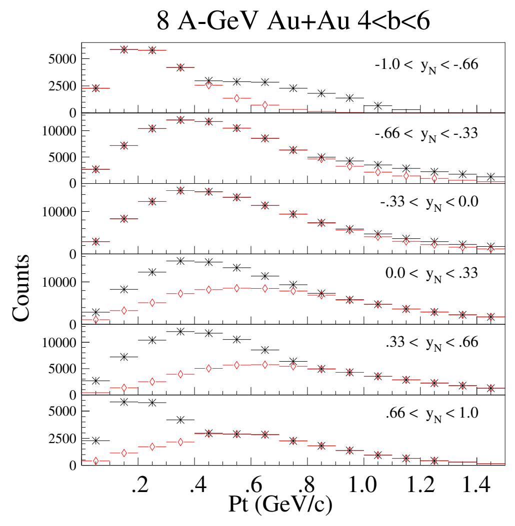

Figure B.14: $P_\perp$ acceptance shown for $8\,A-GeV$ proton, in the $4-6\,fm$ bin. Down the page are the 6 rapidity binnings used in the S-curves. *'s represent corrected data, diamonds uncorrected or raw data. Note that the plot is integrated over the Φ_{flow} dependence of the weighting function.

0 2 4 6 8 10 12 14

0 2 4 6 8 10 12 14

0 2 4 6 8 10 12 14

0 2 4 6 8 10 12 14

0 2 4 6 8 10 12 14

0 2 4 6 8 10 12 14

0 2 4 6 8 10 12 14

0 2 4 6 8 10 12 14

0 2 4 6 8 10 12 14

0 2 4 6 8 10 12 14

0 2 4 6 8 10 12 14

0 2 4 6 8 10 12 14

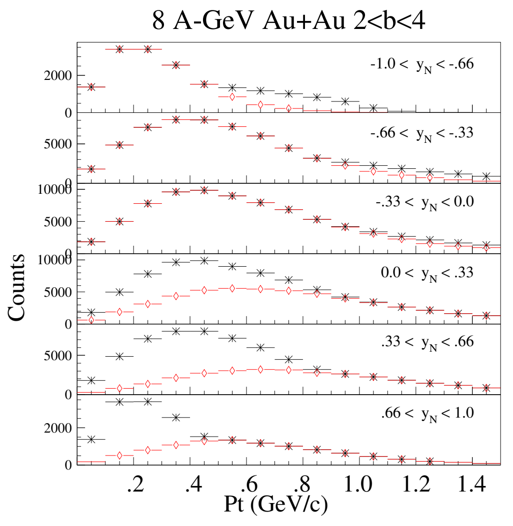

Figure B.15: $P_{\perp}$ acceptance shown for $8\,A-GeV$ proton, in the $2-4\,fm$ bin. Down the page are the 6 rapidity binnings used in the S-curves. *'s represent corrected data, diamonds uncorrected or raw data. Note that the plot is integrated over the Φ_{flow} dependence of the weighting function.

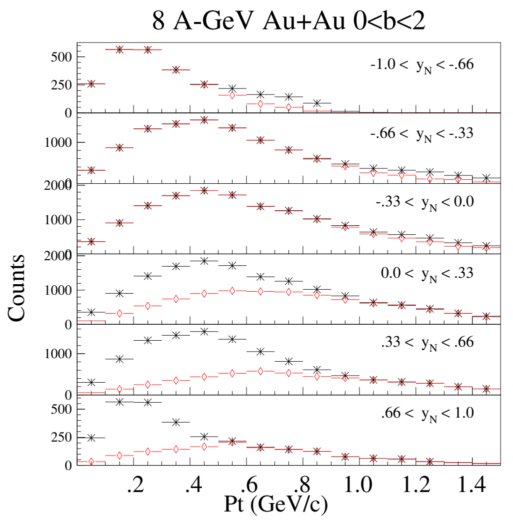

Figure B.16: $P_{\perp}$ acceptance shown for $8\,A-GeV$ proton, in the $0-2\,fm$ bin. Down the page are the 6 rapidity binnings used in the S-curves. *'s represent corrected data, diamonds uncorrected or raw data. Note that the plot is integrated over the Φ_{flow} dependence of the weighting function.

0 2 4 6 8 10 12 14

0 2 4 6 8 10 12 14

0 2 4 6 8 10 12 14

0 2 4 6 8 10 12 14

0 2 4 6 8 10 12 14

0 2 4 6 8 10 12 14

0 2 4 6 8 10 12 14

0 2 4 6 8 10 12 14

0 2 4 6 8 10 12 14

0 2 4 6 8 10 12 14

0 2 4 6 8 10 12 14

0 2 4 6 8 10 12 14

Appendix C

π^+ $P_\perp$ Acceptance

This appendix contains the $P_{\perp}$ weighting functions described in Chapter 4 for π^{+}. Displayed are each of the incident beam energies and impact parameter selections.

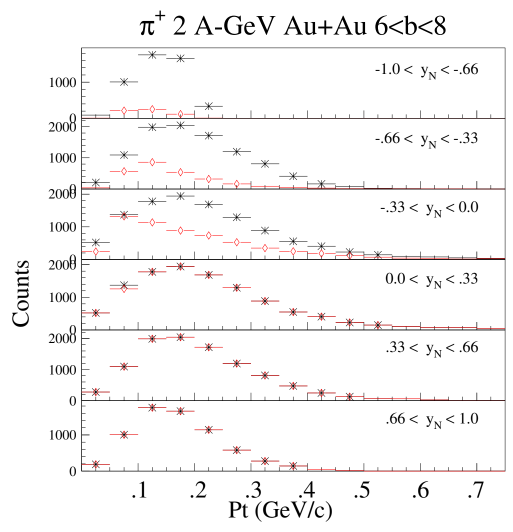

Figure C.1: $P_\perp$ acceptance shown for 2 $A-GeV$ π^+, in the $6-8$ fm bin. Down the page are the 6 rapidity binnings used in the S-curves. *'s represent corrected data, diamonds uncorrected or raw data. Note that the plot is integrated over the Φ_{flow} dependence of the weighting function.

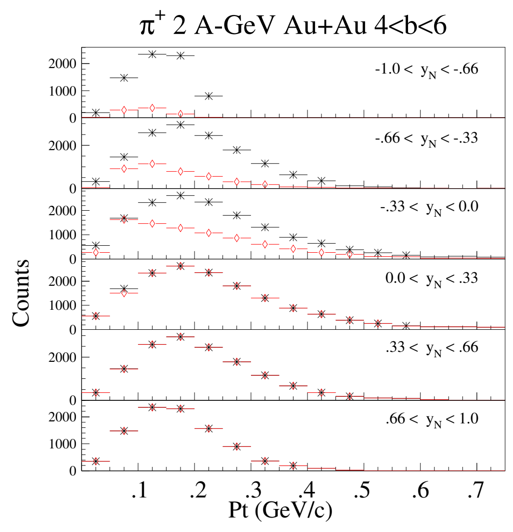

Figure C.2: $P_\perp$ acceptance shown for 2 $A-GeV$ π^+, in the $4-6$ fm bin. Down the page are the 6 rapidity binnings used in the S-curves. *'s represent corrected data, diamonds uncorrected or raw data. Note that the plot is integrated over the Φ_{flow} dependence of the weighting function.

0 2 4 6 8 10 12 14

0 2 4 6 8 10 12 14

0 2 4 6 8 10 12 14

0 2 4 6 8 10 12 14

0 2 4 6 8 10 12 14

0 2 4 6 8 10 12 14

0 2 4 6 8 10 12 14

0 2 4 6 8 10 12 14

0 2 4 6 8 10 12 14

0 2 4 6 8 10 12 14

0 2 4 6 8 10 12 14

0 2 4 6 8 10 12 14

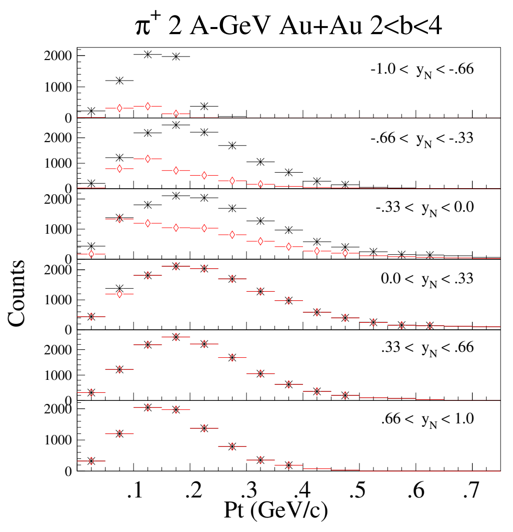

Figure C.3: $P_\perp$ acceptance shown for 2 $A - GeV$ π^+, in the $2 - 4\ fm$ bin. Down the page are the 6 rapidity binnings used in the S-curves. *'s represent corrected data, diamonds uncorrected or raw data. Note that the plot is integrated over the Φ_{flow} dependence of the weighting function.

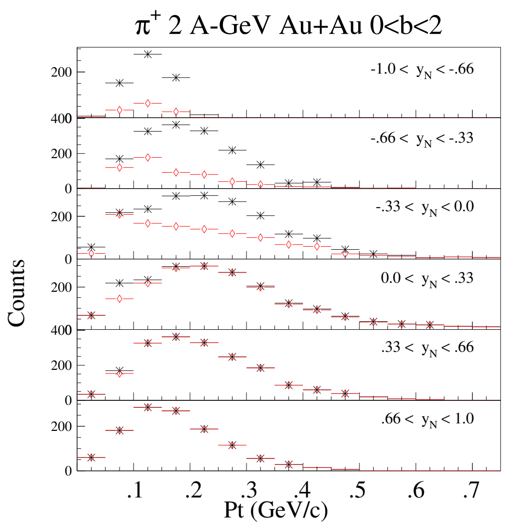

Figure C.4: $P_\perp$ acceptance shown for 2 $A - GeV$ π^+, in the $0 - 2\ fm$ bin. Down the page are the 6 rapidity binnings used in the S-curves. *'s represent corrected data, diamonds uncorrected or raw data. Note that the plot is integrated over the Φ_{flow} dependence of the weighting function.

0 2 4 6 8 10 12 14
0 2 4 6 8 10 12 14
0 2 4 6 8 10 12 14
0 2 4 6 8 10 12 14
0 2 4 6 8 10 12 14
0 2 4 6 8 10 12 14

0 2 4 6 8 10 12 14
0 2 4 6 8 10 12 14
0 2 4 6 8 10 12 14
0 2 4 6 8 10 12 14
0 2 4 6 8 10 12 14
0 2 4 6 8 10 12 14

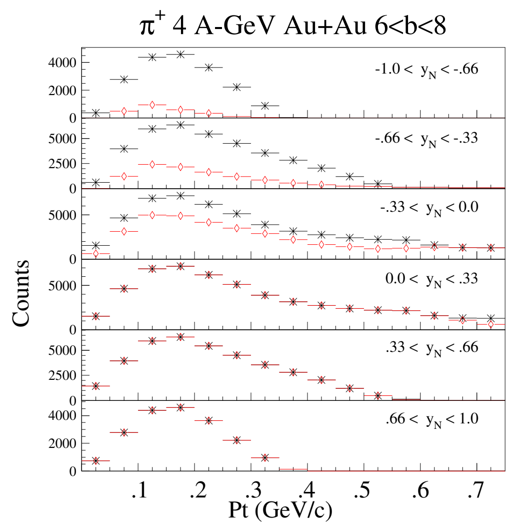

Figure C.5: $P_{\perp}$ acceptance shown for $4\ A - GeV\ \pi^+$, in the $6 - 8\ fm$ bin. Down the page are the 6 rapidity binnings used in the S-curves. *'s represent corrected data, diamonds uncorrected or raw data. Note that the plot is integrated over the Φ_{flow} dependence of the weighting function.

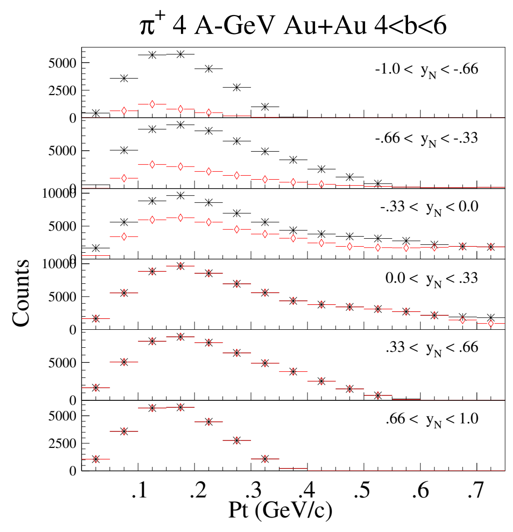

Figure C.6: $P_{\perp}$ acceptance shown for $4\ A - GeV\ \pi^+$, in the $4 - 6\ fm$ bin. Down the page are the 6 rapidity binnings used in the S-curves. *'s represent corrected data, diamonds uncorrected or raw data. Note that the plot is integrated over the Φ_{flow} dependence of the weighting function.

0 2 4 6 8 10 12 14

0 2 4 6 8 10 12 14

0 2 4 6 8 10 12 14

0 2 4 6 8 10 12 14

0 2 4 6 8 10 12 14

0 2 4 6 8 10 12 14

0 2 4 6 8 10 12 14

0 2 4 6 8 10 12 14

0 2 4 6 8 10 12 14

0 2 4 6 8 10 12 14

0 2 4 6 8 10 12 14

0 2 4 6 8 10 12 14

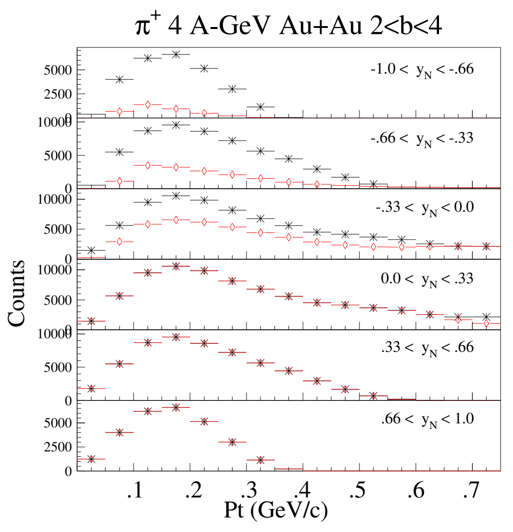

Figure C.7: $P_\perp$ acceptance shown for $4\ A-GeV\ \pi^+$, in the $2-4\ fm$ bin. Down the page are the 6 rapidity binnings used in the S-curves. *'s represent corrected data, diamonds uncorrected or raw data. Note that the plot is integrated over the Φ_{flow} dependence of the weighting function.

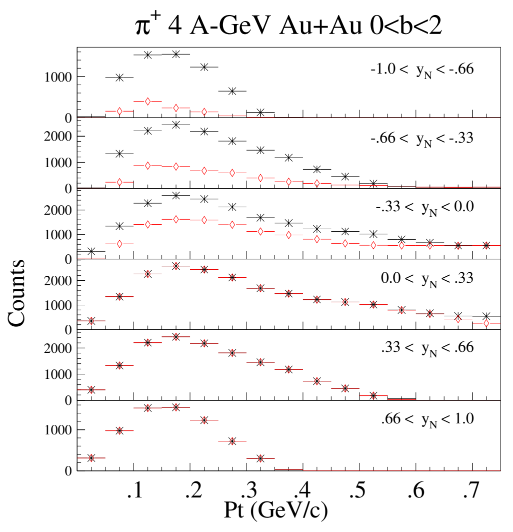

Figure C.8: $P_\perp$ acceptance shown for $4\ A-GeV\ \pi^+$, in the $0-2\ fm$ bin. Down the page are the 6 rapidity binnings used in the S-curves. *'s represent corrected data, diamonds uncorrected or raw data. Note that the plot is integrated over the Φ_{flow} dependence of the weighting function.

0 2 4 6 8 10 12 14
0 2 4 6 8 10 12 14
0 2 4 6 8 10 12 14
0 2 4 6 8 10 12 14
0 2 4 6 8 10 12 14
0 2 4 6 8 10 12 14

0 2 4 6 8 10 12 14
0 2 4 6 8 10 12 14
0 2 4 6 8 10 12 14
0 2 4 6 8 10 12 14
0 2 4 6 8 10 12 14
0 2 4 6 8 10 12 14

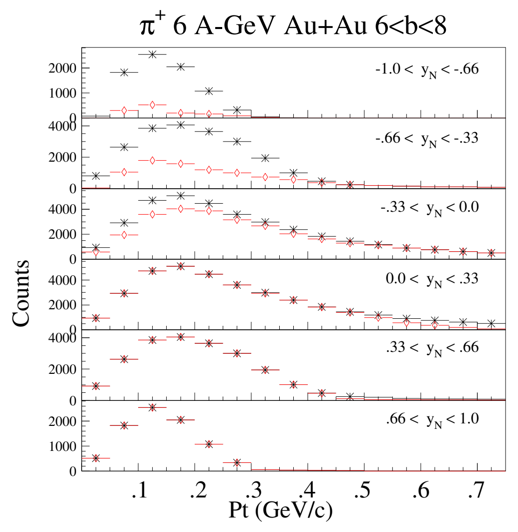

Figure C.9: $P_{\perp}$ acceptance shown for 6 $A-GeV$ π^{+}, in the $6-8\,fm$ bin. Down the page are the 6 rapidity binnings used in the S-curves. *'s represent corrected data, diamonds uncorrected or raw data. Note that the plot is integrated over the Φ_{flow} dependence of the weighting function.

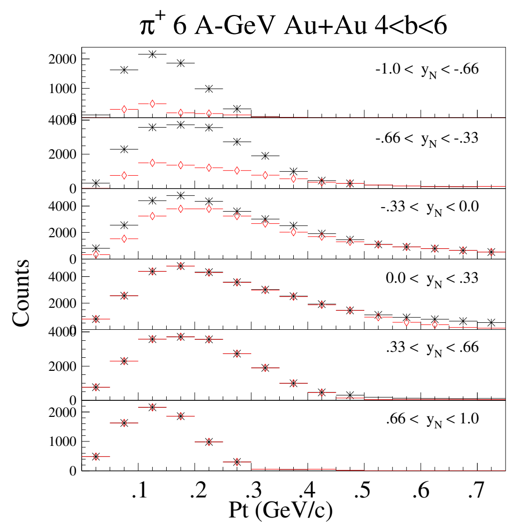

Figure C.10: $P_{\perp}$ acceptance shown for 6 $A-GeV$ π^{+}, in the $4-6\,fm$ bin. Down the page are the 6 rapidity binnings used in the S-curves. *'s represent corrected data, diamonds uncorrected or raw data. Note that the plot is integrated over the Φ_{flow} dependence of the weighting function.

0 2 4 6 8 10 12 14

0 2 4 6 8 10 12 14

0 2 4 6 8 10 12 14

0 2 4 6 8 10 12 14

0 2 4 6 8 10 12 14

0 2 4 6 8 10 12 14

0 2 4 6 8 10 12 14

0 2 4 6 8 10 12 14

0 2 4 6 8 10 12 14

0 2 4 6 8 10 12 14

0 2 4 6 8 10 12 14

0 2 4 6 8 10 12 14

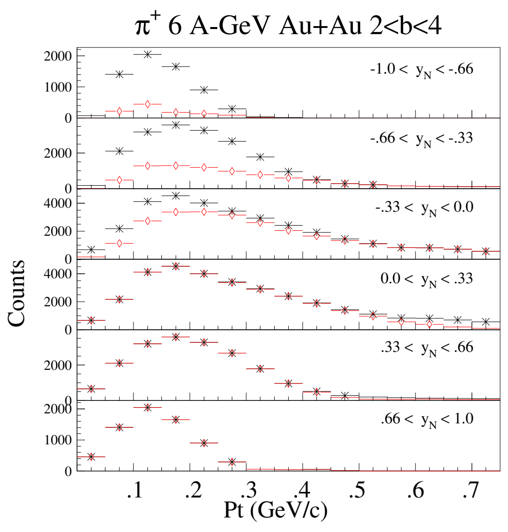

Figure C.11: $P_\perp$ acceptance shown for $6\,A-GeV\ \pi^+$, in the $2-4\,fm$ bin. Down the page are the 6 rapidity binnings used in the S-curves. *'s represent corrected data, diamonds uncorrected or raw data. Note that the plot is integrated over the Φ_{flow} dependence of the weighting function.

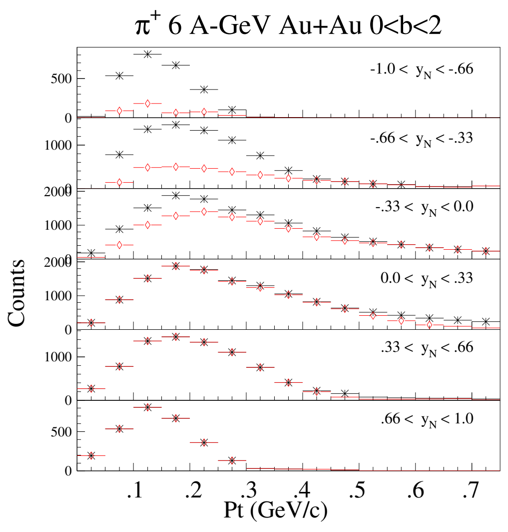

Figure C.12: $P_\perp$ acceptance shown for $6\,A-GeV\ \pi^+$, in the $0-2\,fm$ bin. Down the page are the 6 rapidity binnings used in the S-curves. *'s represent corrected data, diamonds uncorrected or raw data. Note that the plot is integrated over the Φ_{flow} dependence of the weighting function.

0 2 4 6 8 10 12 14
0 2 4 6 8 10 12 14
0 2 4 6 8 10 12 14
0 2 4 6 8 10 12 14
0 2 4 6 8 10 12 14
0 2 4 6 8 10 12 14

0 2 4 6 8 10 12 14
0 2 4 6 8 10 12 14
0 2 4 6 8 10 12 14
0 2 4 6 8 10 12 14
0 2 4 6 8 10 12 14
0 2 4 6 8 10 12 14

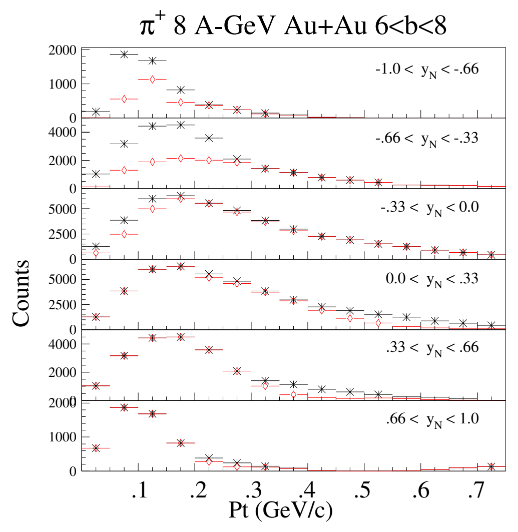

Figure C.13: $P_{\perp}$ acceptance shown for $8\,A-GeV$ π^+, in the $6-8\,fm$ bin. Down the page are the 6 rapidity binnings used in the S-curves. *'s represent corrected data, diamonds uncorrected or raw data. Note that the plot is integrated over the Φ_{flow} dependence of the weighting function.

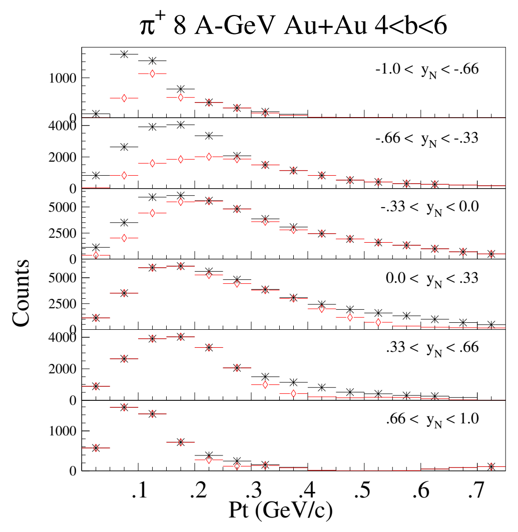

Figure C.14: $P_{\perp}$ acceptance shown for $8\,A-GeV$ π^+, in the $4-6\,fm$ bin. Down the page are the 6 rapidity binnings used in the S-curves. *'s represent corrected data, diamonds uncorrected or raw data. Note that the plot is integrated over the Φ_{flow} dependence of the weighting function.

0 2 4 6 8 10 12 14

0 2 4 6 8 10 12 14

0 2 4 6 8 10 12 14

0 2 4 6 8 10 12 14

0 2 4 6 8 10 12 14

0 2 4 6 8 10 12 14

0 2 4 6 8 10 12 14

0 2 4 6 8 10 12 14

0 2 4 6 8 10 12 14

0 2 4 6 8 10 12 14

0 2 4 6 8 10 12 14

0 2 4 6 8 10 12 14

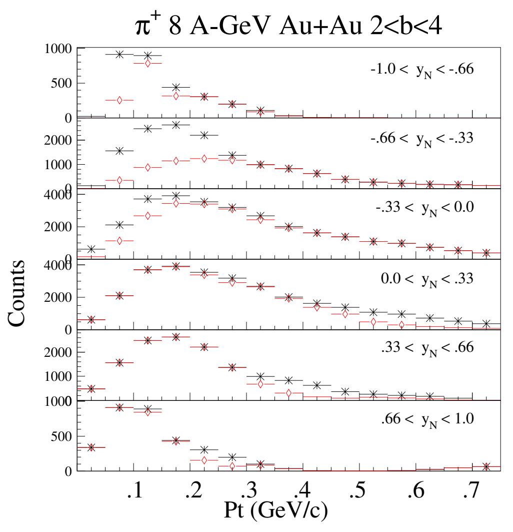

Figure C.15: $P_\perp$ acceptance shown for $8\,A-GeV\ \pi^+$, in the $2-4\,fm$ bin. Down the page are the 6 rapidity binnings used in the S-curves. *'s represent corrected data, diamonds uncorrected or raw data. Note that the plot is integrated over the Φ_{flow} dependence of the weighting function.

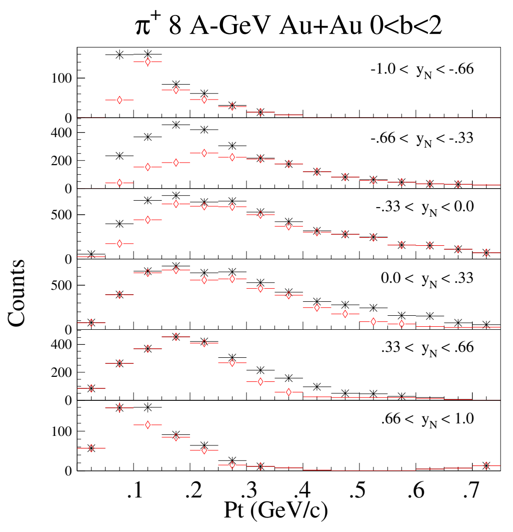

Figure C.16: $P_\perp$ acceptance shown for $8\,A-GeV\ \pi^+$, in the $0-2\,fm$ bin. Down the page are the 6 rapidity binnings used in the S-curves. *'s represent corrected data, diamonds uncorrected or raw data. Note that the plot is integrated over the Φ_{flow} dependence of the weighting function.

0 2 4 6 8 10 12 14

0 2 4 6 8 10 12 14

0 2 4 6 8 10 12 14

0 2 4 6 8 10 12 14

0 2 4 6 8 10 12 14

0 2 4 6 8 10 12 14

0 2 4 6 8 10 12 14

0 2 4 6 8 10 12 14

0 2 4 6 8 10 12 14

0 2 4 6 8 10 12 14

0 2 4 6 8 10 12 14

0 2 4 6 8 10 12 14

Appendix D

π^- $P_\perp$ Acceptance

This appendix contains the $P_\perp$ weighting functions described in Chapter 4 for π^-. Displayed are each of the incident beam energies and impact parameter selections.

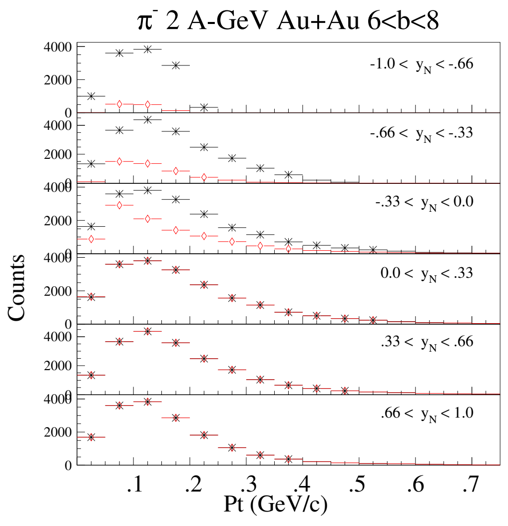

Figure D.1: $P_\perp$ acceptance shown for 2 $A - GeV$ π^-, in the $6 - 8$ fm bin. Down the page are the 6 rapidity binnings used in the S-curves. *'s represent corrected data, diamonds uncorrected or raw data. Note that the plot is integrated over the Φ_{flow} dependence of the weighting function.

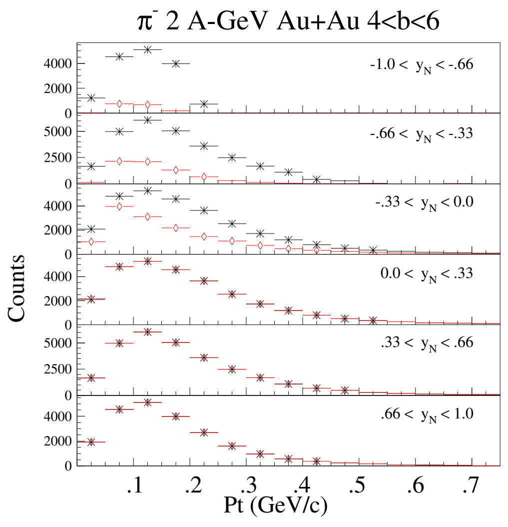

Figure D.2: $P_\perp$ acceptance shown for 2 $A - GeV$ π^-, in the $4 - 6$ fm bin. Down the page are the 6 rapidity binnings used in the S-curves. *'s represent corrected data, diamonds uncorrected or raw data. Note that the plot is integrated over the Φ_{flow} dependence of the weighting function.

0 2 4 6 8 10 12 14

0 2 4 6 8 10 12 14

0 2 4 6 8 10 12 14

0 2 4 6 8 10 12 14

0 2 4 6 8 10 12 14

0 2 4 6 8 10 12 14

0 2 4 6 8 10 12 14

0 2 4 6 8 10 12 14

0 2 4 6 8 10 12 14

0 2 4 6 8 10 12 14

0 2 4 6 8 10 12 14

0 2 4 6 8 10 12 14

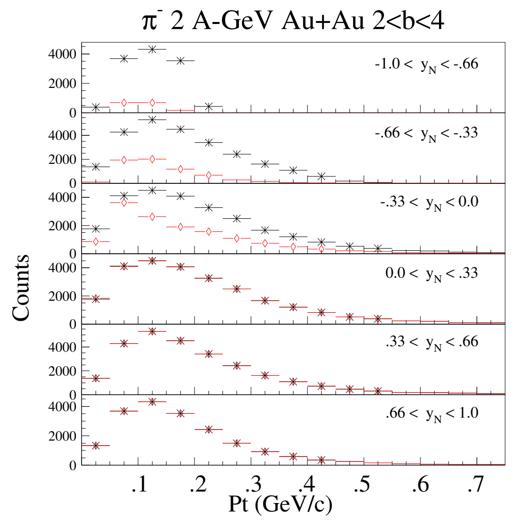

Figure D.3: $P_{\perp}$ acceptance shown for 2 $A - GeV$ π^-, in the $2 - 4$ fm bin. Down the page are the 6 rapidity binnings used in the S-curves. *'s represent corrected data, diamonds uncorrected or raw data. Note that the plot is integrated over the Φ_{flow} dependence of the weighting function.

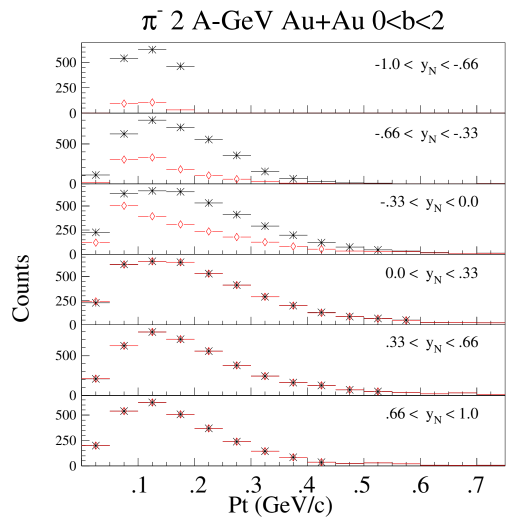

Figure D.4: $P_{\perp}$ acceptance shown for 2 $A - GeV$ π^-, in the $0 - 2$ fm bin. Down the page are the 6 rapidity binnings used in the S-curves. *'s represent corrected data, diamonds uncorrected or raw data. Note that the plot is integrated over the Φ_{flow} dependence of the weighting function.

0 2 4 6 8 10 12 14
0 2 4 6 8 10 12 14
0 2 4 6 8 10 12 14
0 2 4 6 8 10 12 14
0 2 4 6 8 10 12 14
0 2 4 6 8 10 12 14

0 2 4 6 8 10 12 14
0 2 4 6 8 10 12 14
0 2 4 6 8 10 12 14
0 2 4 6 8 10 12 14
0 2 4 6 8 10 12 14
0 2 4 6 8 10 12 14

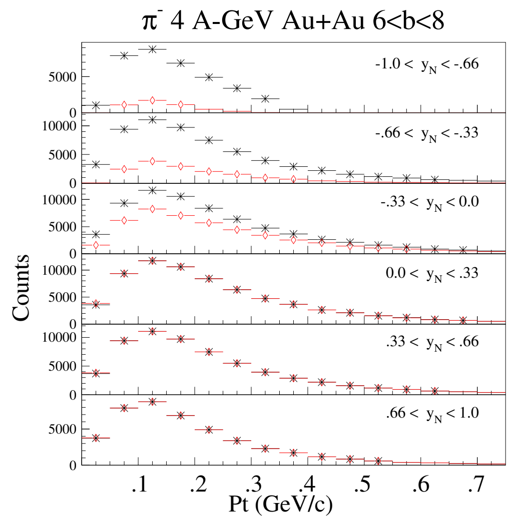

Figure D.5: $P_{\perp}$ acceptance shown for $4\ A-GeV\ \pi^-$, in the $6-8\ fm$ bin. Down the page are the 6 rapidity binnings used in the S-curves. *'s represent corrected data, diamonds uncorrected or raw data. Note that the plot is integrated over the Φ_{flow} dependence of the weighting function.

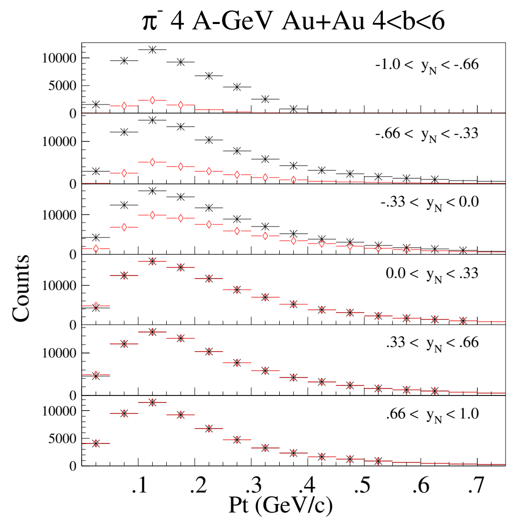

Figure D.6: $P_{\perp}$ acceptance shown for $4\ A-GeV\ \pi^-$, in the $4-6\ fm$ bin. Down the page are the 6 rapidity binnings used in the S-curves. *'s represent corrected data, diamonds uncorrected or raw data. Note that the plot is integrated over the Φ_{flow} dependence of the weighting function.

0 2 4 6 8 10 12 14
0 2 4 6 8 10 12 14
0 2 4 6 8 10 12 14
0 2 4 6 8 10 12 14
0 2 4 6 8 10 12 14
0 2 4 6 8 10 12 14

0 2 4 6 8 10 12 14
0 2 4 6 8 10 12 14
0 2 4 6 8 10 12 14
0 2 4 6 8 10 12 14
0 2 4 6 8 10 12 14
0 2 4 6 8 10 12 14

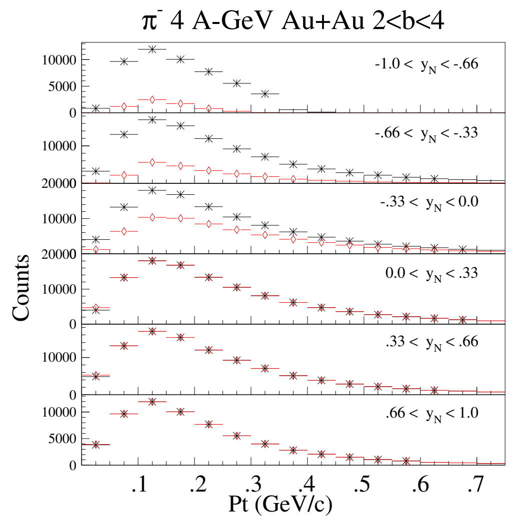

Figure D.7: $P_\perp$ acceptance shown for $4\,A-GeV\ \pi^-$, in the $2-4\ fm$ bin. Down the page are the 6 rapidity binnings used in the S-curves. *'s represent corrected data, diamonds uncorrected or raw data. Note that the plot is integrated over the Φ_{flow} dependence of the weighting function.

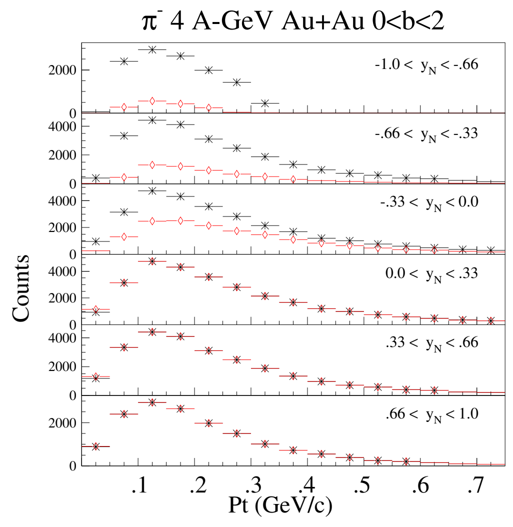

Figure D.8: $P_\perp$ acceptance shown for $4\,A-GeV\ \pi^-$, in the $0-2\ fm$ bin. Down the page are the 6 rapidity binnings used in the S-curves. *'s represent corrected data, diamonds uncorrected or raw data. Note that the plot is integrated over the Φ_{flow} dependence of the weighting function.

0 2 4 6 8 10 12 14

0 2 4 6 8 10 12 14

0 2 4 6 8 10 12 14

0 2 4 6 8 10 12 14

0 2 4 6 8 10 12 14

0 2 4 6 8 10 12 14

0 2 4 6 8 10 12 14

0 2 4 6 8 10 12 14

0 2 4 6 8 10 12 14

0 2 4 6 8 10 12 14

0 2 4 6 8 10 12 14

0 2 4 6 8 10 12 14

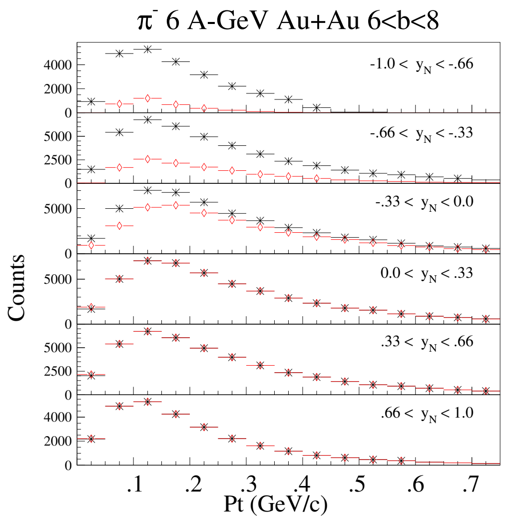

Figure D.9: $P_\perp$ acceptance shown for $6\,A-GeV\ \pi^-$, in the $6-8\,fm$ bin. Down the page are the 6 rapidity binnings used in the S-curves. *'s represent corrected data, diamonds uncorrected or raw data. Note that the plot is integrated over the Φ_{flow} dependence of the weighting function.

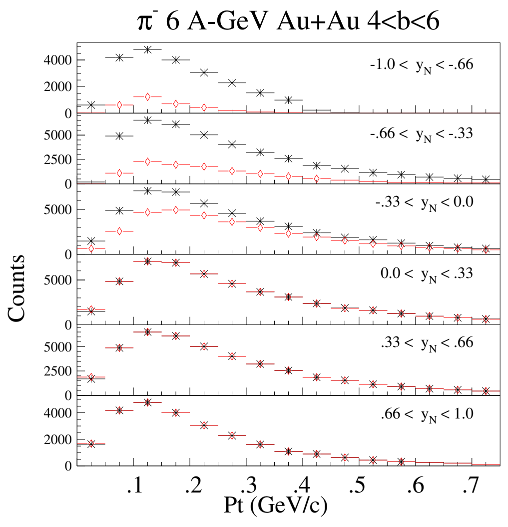

Figure D.10: $P_\perp$ acceptance shown for $6\,A-GeV\ \pi^-$, in the $4-6\,fm$ bin. Down the page are the 6 rapidity binnings used in the S-curves. *'s represent corrected data, diamonds uncorrected or raw data. Note that the plot is integrated over the Φ_{flow} dependence of the weighting function.

0 2 4 6 8 10 12 14

0 2 4 6 8 10 12 14

0 2 4 6 8 10 12 14

0 2 4 6 8 10 12 14

0 2 4 6 8 10 12 14

0 2 4 6 8 10 12 14

0 2 4 6 8 10 12 14

0 2 4 6 8 10 12 14

0 2 4 6 8 10 12 14

0 2 4 6 8 10 12 14

0 2 4 6 8 10 12 14

0 2 4 6 8 10 12 14

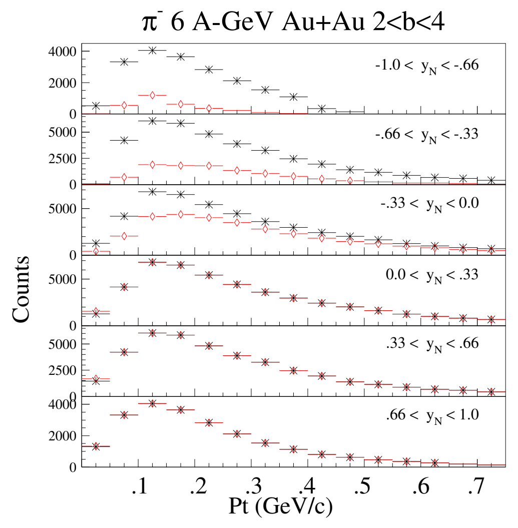

Figure D.11: $P_\perp$ acceptance shown for $6\,A-GeV\ \pi^-$, in the $2-4\,fm$ bin. Down the page are the 6 rapidity binnings used in the S-curves. *'s represent corrected data, diamonds uncorrected or raw data. Note that the plot is integrated over the Φ_{flow} dependence of the weighting function.

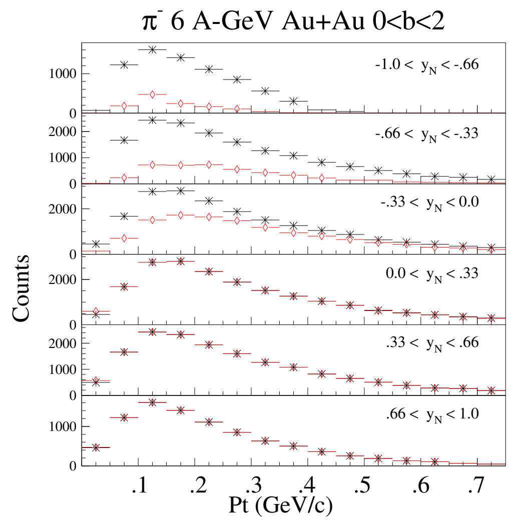

Figure D.12: $P_\perp$ acceptance shown for $6\,A-GeV\ \pi^-$, in the $0-2\,fm$ bin. Down the page are the 6 rapidity binnings used in the S-curves. *'s represent corrected data, diamonds uncorrected or raw data. Note that the plot is integrated over the Φ_{flow} dependence of the weighting function.

0 2 4 6 8 10 12 14

0 2 4 6 8 10 12 14

0 2 4 6 8 10 12 14

0 2 4 6 8 10 12 14

0 2 4 6 8 10 12 14

0 2 4 6 8 10 12 14

0 2 4 6 8 10 12 14

0 2 4 6 8 10 12 14

0 2 4 6 8 10 12 14

0 2 4 6 8 10 12 14

0 2 4 6 8 10 12 14

0 2 4 6 8 10 12 14

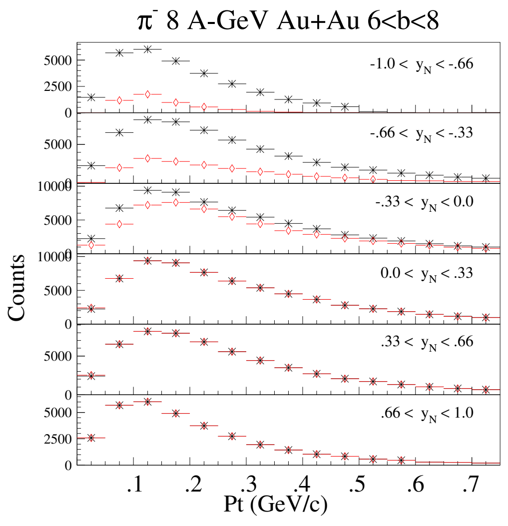

Figure D.13: $P_{\perp}$ acceptance shown for $8\,A-GeV\ \pi^-$, in the $6-8\,fm$ bin. Down the page are the 6 rapidity binnings used in the S-curves. *'s represent corrected data, diamonds uncorrected or raw data. Note that the plot is integrated over the Φ_{flow} dependence of the weighting function.

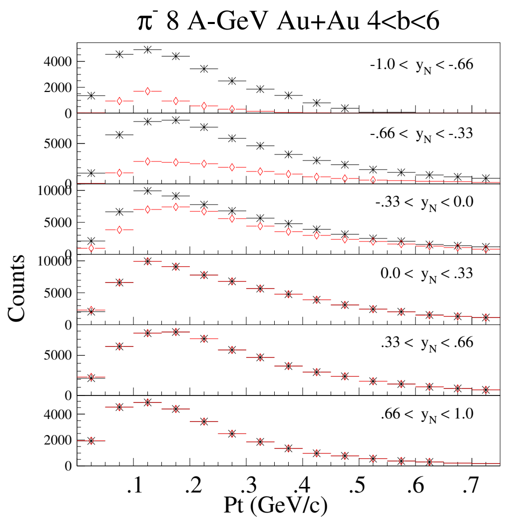

Figure D.14: $P_{\perp}$ acceptance shown for $8\,A-GeV\ \pi^-$, in the $4-6\,fm$ bin. Down the page are the 6 rapidity binnings used in the S-curves. *'s represent corrected data, diamonds uncorrected or raw data. Note that the plot is integrated over the Φ_{flow} dependence of the weighting function.

0 2 4 6 8 10 12 14
0 2 4 6 8 10 12 14
0 2 4 6 8 10 12 14
0 2 4 6 8 10 12 14
0 2 4 6 8 10 12 14
0 2 4 6 8 10 12 14

0 2 4 6 8 10 12 14
0 2 4 6 8 10 12 14
0 2 4 6 8 10 12 14
0 2 4 6 8 10 12 14
0 2 4 6 8 10 12 14
0 2 4 6 8 10 12 14

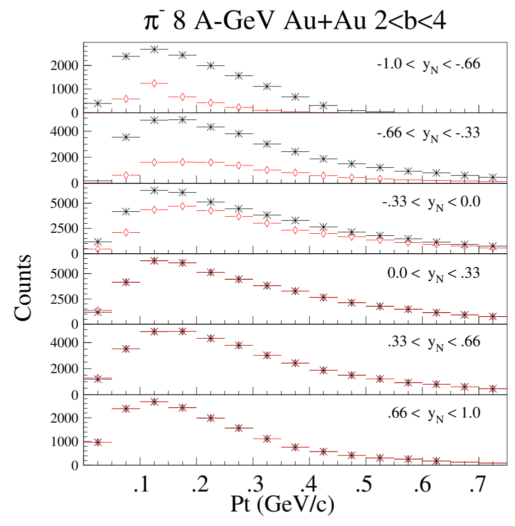

Figure D.15: $P_{\perp}$ acceptance shown for $8\,A-GeV$ π^{-}, in the $2-4\,fm$ bin. Down the page are the 6 rapidity binnings used in the S-curves. *'s represent corrected data, diamonds uncorrected or raw data. Note that the plot is integrated over the Φ_{flow} dependence of the weighting function.

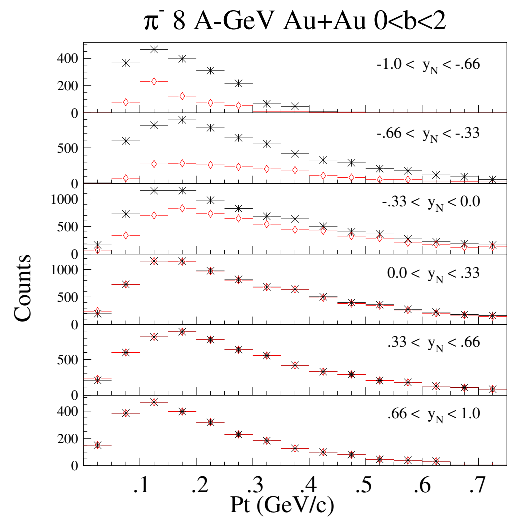

Figure D.16: $P_{\perp}$ acceptance shown for $8\,A-GeV$ π^{-}, in the $0-2\,fm$ bin. Down the page are the 6 rapidity binnings used in the S-curves. *'s represent corrected data, diamonds uncorrected or raw data. Note that the plot is integrated over the Φ_{flow} dependence of the weighting function.

0 2 4 6 8 10 12 14
0 2 4 6 8 10 12 14
0 2 4 6 8 10 12 14
0 2 4 6 8 10 12 14
0 2 4 6 8 10 12 14
0 2 4 6 8 10 12 14

0 2 4 6 8 10 12 14
0 2 4 6 8 10 12 14
0 2 4 6 8 10 12 14
0 2 4 6 8 10 12 14
0 2 4 6 8 10 12 14
0 2 4 6 8 10 12 14

Appendix E

Impact Parameter

We can not directly measure the impact parameter in heavy ion collisions. In order to determine the magnitude of this vector we have to make some assumptions. First we assume that the event anisotropy is aligned with the impact parameter. This allows us to use the Q-vector discussed in Chapter 3 to find the impact parameters direction. In order to recover the magnitude of the impact parameter we assume that the event multiplicities are dependent on it. With a very simple geometric model for the nucleus cross section, the multiplicity distribution, and the assumption that the multiplicity is a monotonic function of the impact parameter, b, the impact parameter can be calculated. A refinement not used here, would be to convolute the multiplicity distribution for a given impact parameter. This would be model dependent.

First we start with the general cross section and derive the relations between the impact parameter and the integrated multiplicity distribution. The general cross section is

$$\begin{aligned} \sigma &= \frac{N}{I \times S} \qquad \text{(E.1)} \\ I &= incident\,flux \\ S &= number\,of\,scattering\,centers\,(/barn) \\ N &= scattering\,rate \end{aligned}$$

The scattering rate N integrated over the impact parameter range can then be written as

$$\int_0^B \frac{dN}{db} db \;=\; I\,S\sigma \tag{E.2}$$

where B is the maximum impact parameter considered. This becomes

$$\int_0^B \frac{dN}{dm}\frac{dm}{db} db \;=\; I\,S\sigma \tag{E.3}$$

where multiplicity,

$$m \;=\; m(b)$$

The maximum multiplicity (MAX) goes with zero impact parameter. This results in Eq. (E.4), where M_c is the multiplicity cut that goes with the maximum impact parameter B and with σ.

$$\int_{M_c}^{MAX} \frac{dN}{dm} dm \;=\; I\,S\sigma \tag{E.4}$$

Then using the geometric cross section the impact parameter can be determined.

$$\int_{M_c(b)}^{MAX} \frac{dN}{dm} dm \;=\; I\,S\,\pi b^2 \tag{E.5}$$

We now only need the multiplicity distributions and the constants I and S, to complete the calculation. The TPC will be used to determine the multiplicity distribution. We can calculate a cross section σ_{M_c} that goes with any multiplicity cut M_c by

$$\frac{\sigma_{M_c}}{\pi B^2} = \frac{\int_{Mc}^{MAX} \frac{dN}{dm} dm}{\int_0^{MAX} \frac{dN}{dm} dm} \tag{E.6}$$

where B is the sum of the radii of the colliding nuclei. The left hand side of Eq. (E.6) is called the percentage centrality. This approach does not require the scalers. However, this approach works only if we have a complete multiplicity spectrum down to $M_c = 0$, obtainable only with a beam trigger. We do not have such data available so we take the alternate approach of using the scalers.

$$\frac{\sigma_{trig}}{\pi B^2} = \frac{\int_{Mctrig}^{MAX} \frac{dN}{dm} dm}{\int_0^{MAX} \frac{dN}{dm} dm} \tag{E.7}$$

First we calculate S and I to find σ_{trig}. S the number of scattering centers for the ^{197}Au targets, can be found by

$$\begin{aligned} S &= \frac{\rho N_a}{A_w}\, target\, thickness \qquad \text{(E.8)} \\ \rho &= 19.299\, (g/cm^3) \\ N_a &= 6.022x10^{23}\, (part/mole) \\ A_w &= 197\, (g/mole)\, atomic\, weight \end{aligned}$$

We had three gold targets of varying thickness.

Target	Thickness (cm)	S (particles/barn)
10 mil	.0254	1.498×10^{-3}
20	.0508	2.997×10^{-3}
30	.0762	4.495×10^{-3}

In order to get the incident flux we need to use the scalers generated from the upstream scintillators. There are a few complications in using these that will be discussed as they arise. One of the problems was that the list of scalers that were recorded differed from one year to the next.

For the 2 and 4 A-GeV

On page 202 of the E895 logbook # 1 (1995) is a listing of the scalers recorded during the 2 and 4 $A-GeV$ runs. This is Table E.1. I used the scalers accumulated in run number 1205 for the 2 $A-GeV$ and, a series of runs 1140-1145 for the 4 $A-GeV$ run.

6 and 8 A-GeV

For the 6 and 8$A-GeV$ the same prescription was followed except the scalers were changed. The relevant list is on page 19 of the E895 logbook #2 from (1996) and is reproduced here in Table E.2. Runs 260 and 1060 were used for 6 $A-GeV$ and 8 $A-GeV$ cross sections, respectively.

Note that scaler 8 in Table E.1 and scaler 4 in Table E.2 are all beam particles. Similarly, scaler 6 in Table E.1 and scaler 9 in Table E.2 are all interactions.

Now there is another complication. The scalers were ungated through the entire spill. The AGS is not a continuous beam accelerator, it 'spills' its accelerated contents for ~ 1 *sec*. Normally, one might expect to have two sets of scalers, one cleared at

Scaler #	Logic Value
0	1khz Clock
1	10khz
2	100khz
3	1Mhz
4	-
5	spill #
6	$\overline{V2} \cdot B1 \cdot \overline{ST}$
7	ST_{upper}
8	$B1 \cdot \overline{V2}$
9	$\overline{V2} \cdot B1 \cdot \overline{ST} \cdot \overline{BUSY}$
10	$\overline{V2} \cdot B1 \cdot \overline{ST}$
11	-

Table E.1: List of Scalers for the 2 and 4 $A - GeV$. NOTE: In the 4 $A - GeV$ run scaler 6 was moved to scaler 11. In the table S1,S2,V1,V2 and ST stand for the logic signals from these scintillators respectively. These scintillators are shown in Fig. 2.7. B1 refers to logic signals as $B1 = S1 \cdot \overline{V1}$. The $\overline{ST}$ counts pulses above the lower noise and below the upper (gold nuclei) thresholds discussed in Chapter 2, so $\overline{ST}$ from an incident beam particle means an interaction.

Scaler #	Logic Value
0	1Mhz Clock
1	$clock \cdot spill$
2	$clock \cdot spill \cdot \overline{BUSY} = LIVETIME$
3	spill number
4	B2
5	$B2 \cdot LIVETIME$
6	pretriggers
7	master triggers
8	laser firing
9	interaction
10	canary gated clock
11	canary gates

Table E.2: List of Scalers for the 6 and 8 $A - GeV$. $B2 = B1 \cdot \overline{V2} \cdot ST =$ all beam particles.

the end of each spill, and one cleared only at the end of each run. The end-of-run scalers are usually used for calculations of cross sections. However, in our case we had to integrate the end-of-spill scalers. This would have been straightforward had we only had a single tape stream, but with three tape streams, care had to be taken to insure that the scaler values were integrated properly. We had to deal with the master triggers here. Master trigger means the number of events during the spill. A master trigger of 2 meant that two events had been taken when the scalers were saved. Note that the master triggers were structured such that master trigger 1's went to que0, 2's to que2 and 3's to que4, before repeating in the tape que.

The trigger cross section can then be calculated from the scalers by

$$\sigma_{trig} = \frac{\int Scaler\ 6}{\int Scaler\ 8 \cdot S} \tag{E.9}$$

for the 2 and 4 $A - GeV$ and

$$\sigma_{trig} = \frac{\int Scaler\ 9}{\int Scaler\ 4 \cdot S} \tag{E.10}$$

for the 6 and 8 $A - GeV$.

However, for historical reasons a slightly different but equivalent method was applied. The equations are as follows.

For the 2 and 4 A-GeV runs

Energy	Trigger Imact Parameter (Minimum Bias Data)
2	$10.3 \pm 0.5\, fm$
4	$9.3 \pm 0.5\, fm$
6	$15.6 \pm 0.5\, fm$
8	$12.9 \pm 0.5\, fm$

Table E.3: List of maximum impact parameters achieved by the various trigger settings.

$$LIVETIME \;=\; \frac{\int Scaler\,9}{\int Scaler\,6} \tag{E.11}$$

of Table E.1.

For 2 and 4 A-GeV

$$\sigma_{trig} \;=\; \frac{\int Scaler\,9}{\int Scaler\,8 \cdot\; LIVETIME \cdot S} \tag{E.12}$$

which reduces to Eq. (E.9). For 6 and 8 $A - GeV$,

$$\sigma_{trig} \;=\; \frac{\int Scaler\,9}{\int Scaler\,4 \cdot\; S} \tag{E.13}$$

which is Eq. (E.10).

Impact parameter

Once σ_{trig} has been obtained from Eq. (E.9 or E.10), we can calculate the associated largest impact parameter as long as the minimum multiplicity associated with the trigger is considerably less than the multiplicity associated with this impact parameter. For example, for a desired selection of $b = 2 - 4\, fm$, Eq. (E.6) is used with $B = 2$ and then repeated for $B = 4$. The two resulting values of M_c are the multiplicity boundaries of the $2 - 4\,fm$ band. An iterative process is used by varying M_c until Eq. (E.7) is satisfied for any required B. A list of the cuts obtained for this dissertation are in Table 3.3. A graphical representation of the results is Fig. E.1.

It should be noted that there are no software event selections made on the data when determining the trigger cross section by the scalers. In data analysis the multiplicity distributions often have some quality cuts made on the tracks that make up the distribution, and this changes the multiplicity. As a result, the criteria for 'good' tracks must not change from the point of determining the multiplicity cuts to their use on the data to determine the impact parameter. Once the boundaries for the impact parameter band for a given set of events is determined, one is free to apply additional quality cuts to those events. For the purposes of all the impact parameter determinations here, a track quality cut of DCA $< 2.5\,cm$ (from the vertex) was used.

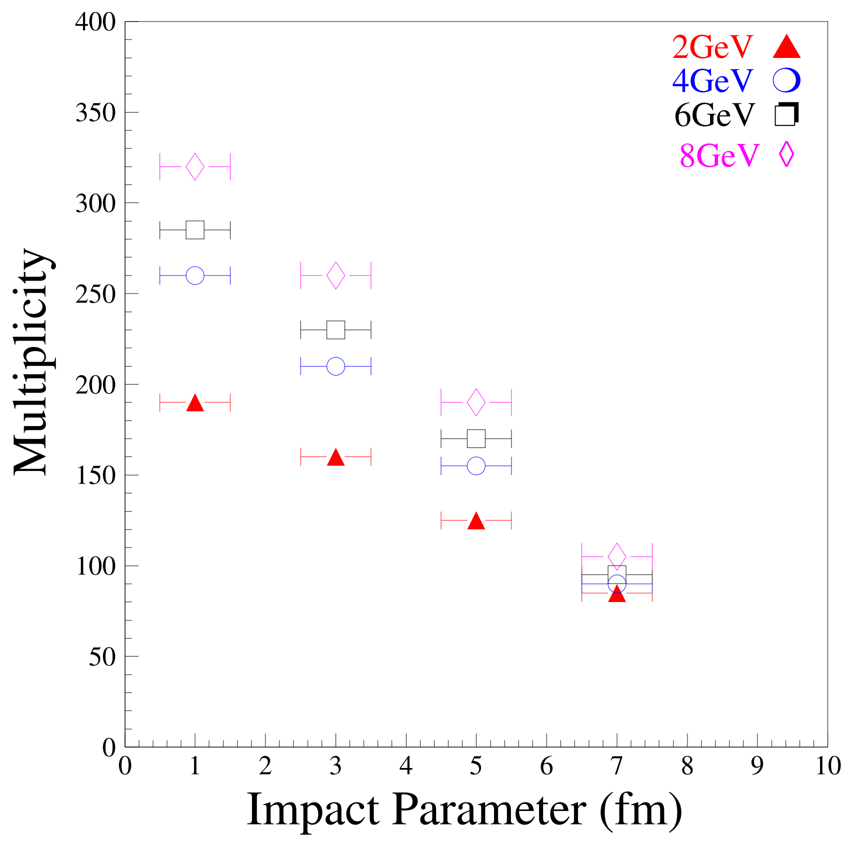

Figure E.1: Multiplicity versus cross section determined impact parameter.

Bibliography

[Ahle77] S.P. Ahlen *et al.* Nuc. Inst. and Meth. **147** 321 (1977)

[Ahle80] S.P. Ahlen *et al.* Rev. of Modern Phys. **v52 no. 1** (1980)

[Aich86] J. Aichelin and H. Stöcker, Phys. Lett. **B176**, 14 (1986).

[Alli80] W.W.M.Allison, J.H.Cobb, Ann. Rev. Nucl. Part. Sci. **30**, 253 (1980).

[Appl98] H. Appelhauser *et al.*, Phys. Rev. Lett. **80** 4136-4140, (1998)

[Bade82] A.Baden *et al.*, Nucl. Instr. Meth. **203**, 189 (1982).

[Barn98] R.M. Barnett *et al.* Phys. Rev. **D54(1-I)** (1998).

[Barr96] J. Barrette *et al.*, Nucl. Phys. **A610**, 63c (1996).

[Barr97] J. Barrette *et al.*, Phys. Rev. **C55**, 1420 (1997).

[Barr97] J. Barrette *et al.* Phys. Rev. **C58** 3254 (1997)

[Bass93] S.A.Bass *et al.*, Phys. Rev. Lett. **71**, 1144 (1993).

[Bass96] S.A.Bass *et al.*, Phys. Rev. **C51**, 3343 (1996).

[Bass98] S.A. Bass *et al.*, Prog. Part. Nucl Phys. **41** 225 (1998)

[Bert84] G.F Bertsch, H. Kruse, and S. Das Gupta, Phys. Rev. **C**, 29, 673 (1984).

[Birk64] J.B. Birks **The theory and Practice of scintillation conters** Pergamon Press, New York 1964.

[Cebr98] D.A.Cebra **Division of Nuc. Phys. American Physical Society Meeting** Whistler, Canada, 1998.

[Chan97] J. Chance *et al.*, Phys. Rev. Lett **78**, 2535 (1997).

[Dani85] P. Danielewicz and G. Odyniec, Phys. Lett. **B 157**, 146 (1985).

[Drap97] J.E. Draper **E895 Collaboration Meeting; Columbus, Ohio** 1997.

[Fern92] R.Fernow, **Introduction to Experimental Particle Phyisics** Cambridge University Press (1992)

[Gust84] H.A.Gustafsson *et al.*, Phys. Rev. Lett. **52**, 1590 (1984).

[Grif87] D. Griffiths **Introduction to Elementary Particles** John Wiley and Sons (1987)

[Herm96] N. Herrmann *et al.*, Nucl. Phys. **A610**, 49c (1996).

[Kint97] J.C.Kintner *et al.* Phys. Rev. Lett. **78**, 4165 (1997).

[Klay98] J.Klay **E895 Collaboration Meeting, St. Mary's College** December, 1998.

[Krus85] H. Kruse, B.V. Jacak, and H. Stöcker, Phys. Rev. Lett. **54**, 289 (1985).

[Kaha96] S. Kahana *et al.*, proceeding of the 1st Catania Relativistic Ion Study, Acicastello, Italy (1996).

[LiKo95] B.A. Li and C.M. Ko, Phys. Rev. **C52**, 2037 (1995)

[LiKo96] B.A. Li and C.M. Ko, Phys. Rev. **C53**, R22 (1996)

[LiKo96b] B.A. Li and C.M. Ko, Phys. Rev. **C54**, 3283 (1996)

[LiKo96c] B.A. Li and C.M. Ko, Phys. Rev. **C54**, 844 (1996)

[LiKo96d] B.A. Li and C.M. Ko, Nucl. Phys. **A601**, 457 (1996)

[LiKo98] B.A. Li and C.M. Ko, Phys. Rev. **C58**, 1382 (1998)

[LiKo99] B. A. Li, C.M. Ko, A.T. Sustich, B. Zhang preprint nucl-th/9904013

[Liu97] H.Liu *et. al.* Collective flow in Au+Au collisions between 2-8A GeV at AGS. **Quark Matter** (1997)

[Lohs] T. Lohse and W. Witzeling **The Time Projection Chamber** European Organiztion for Nuclear Research, C.E.R.N, 1211 Geneva 23, Switzerland.

[Mage99] D. Magestro **Winter Workshop on Nuclear Dynamics** Park City, Utah: January (1999).

[Olli95] Ollitrault, J.Y. Nuclear Physics **A590** (no.1-2):561c-4c (1995)

[Part94] M.D. Partlan et al., Fragment Flow in Au+Au Collisions; UC Davis PhD Disseration

[Part97] M. Partlan *et al.*, Phys. Rev. Lett **75**, 2100 (1997).

[Pink96] C.H.Pinkenberg, K. Hildenbrand, Phys. Plonica **27**, 243 (1996).

[Pink99] C. Pinkenberg *et al.* (E895 Collaboration) preprint nucl-ex/9903010

[Posk98] A.M. Poskanzer and S.A. Voloshin, Phys. Rev. C **v58** 1671-1678, (1998)

[Rai90] G.Rai, EOS Collaboration IEEE Transactions on Nuclear Science, **Vol 37**, No.2 April (1990)

[Renf84] R.E.Renfordt *et al.*, Phys. Rev. Lett. **53**, 763 (1984).

[Risc96] D. Riscke, Nucl. Phys. **A610**, 88c (1996).

[Sche74] W.Scheid, H. Müller and W. Greiner, Phys. Rev. Lett. **32**, 741 (1974).

[Scott97] A. Scott Dissertation Kent State University (1997).

[Soff99] S. Soff, S.A. Bass, M. Bleicher, H. Stöcker W. Griener 'Directed and Elliptic Flow' **nucl-th/9903061** (to be published)

[Song99] G. Song, B.A. Li and C.M. Ko, Nucl. Phys. **A646**, 481 (1999)

[STAR92] STAR (Solenoidal Tracker At RHIC) Conceptual Design Report **PUB-5347** 1992.

[Stro83] H.Ströbele,*et al.*, Phys. Rev. **C27**, 1349 (1983).

[Stoc80] H. Stöcker, J. Maruhn, and W. Greiner, Phys. Rev. Lett. **44**, 725 (1980).

[VerW82] B.J. VerWest and R.A. Arndt. Phys. Rev. **C25**, 1979 (1982).